


5-2018

# Self-Assembled Barium Titanate Nanoscale Films by Molecular Beam Epitaxy

Timothy Allen Morgan  
*University of Arkansas, Fayetteville*

Follow this and additional works at: <http://scholarworks.uark.edu/etd>

 Part of the [Metallurgy Commons](#), [Nanoscience and Nanotechnology Commons](#), and the [Polymer and Organic Materials Commons](#)

---

## Recommended Citation

Morgan, Timothy Allen, "Self-Assembled Barium Titanate Nanoscale Films by Molecular Beam Epitaxy" (2018). *Theses and Dissertations*. 2817.  
<http://scholarworks.uark.edu/etd/2817>

This Dissertation is brought to you for free and open access by ScholarWorks@UARK. It has been accepted for inclusion in Theses and Dissertations by an authorized administrator of ScholarWorks@UARK. For more information, please contact [scholar@uark.edu](mailto:scholar@uark.edu), [ccmiddle@uark.edu](mailto:ccmiddle@uark.edu).

Self-Assembled Barium Titanate Nanoscale Films by Molecular Beam Epitaxy

A dissertation submitted in partial fulfillment  
of the requirements for the degree of  
Doctor of Philosophy in Microelectronics-Photonics

by

Timothy Allen Morgan  
Western Kentucky University  
Bachelor of Science in Physics & Mathematics, 2006  
University of Arkansas  
Master of Science in Microelectronics-Photonics, 2008

May 2018  
University of Arkansas

This dissertation is approved for recommendation to the Graduate Council.

---

Gregory J Salamo, Ph.D.  
Dissertation Director

---

Laurent Bellaiche, Ph.D.  
Committee Member

---

Morgan Ware, Ph.D.  
Committee Member

---

Hugh Churchill, Ph.D.  
Committee Member

---

Rick Wise, Ph.D.  
Ex-Officio Member

The following signatories attest that all software used in this dissertation was legally licensed for use by Timothy Allen Morgan for research purposes and publication.

---

Mr. Timothy Allen Morgan, Student

---

Dr. Gregory Salamo, Dissertation Director

This dissertation was submitted to <http://www.turnitin.com> for plagiarism review by the TurnItIn company's software. The signatories have examined the report on this dissertation that was returned by TurnItIn and attest that, in their opinion, the items highlighted by the software are incidental to common usage and are not plagiarized material.

---

Dr. Rick Wise, Program Director

---

Dr. Gregory Salamo, Dissertation Director

## Abstract

One challenge of investigating ferroelectrics at the nanoscale has been controlling the stoichiometry during growth. Historically, the growth of barium titanate ( $\text{BaTiO}_3$ ) by molecular beam epitaxy has relied on a growth technique called shuttered RHEED. Shuttered RHEED controls the stoichiometry of barium titanate through the precise deposition of alternating layers of  $\text{BaO}$  and  $\text{TiO}_2$ . While this approach has achieved 1% control of stoichiometry, finding self-limiting mechanisms to lock-in stoichiometry has been the focus of the growth community. The Goldschmidt tolerance factor predicts an unstable perovskite when barium sits in the titanium lattice site. The  $\text{BaO-TiO}_2$  phase diagram predicts a low-solubility ( $<100$  ppm) of excess barium oxide at molecular beam epitaxy (MBE) growth temperatures of  $600-800$  °C. We show that excess barium provided during MBE growth is a self-limiting mechanism to grow stoichiometric barium titanate thin films.

Features in RHEED oscillations were identified for both shuttered RHEED and co-deposition that confirm barium rich growth condition. Barium-rich growth condition was confirmed to lead to bulk BTO values for out-of-plane lattice constant, Ti/Ba ratio, and piezoelectric coefficient for 40 nm thick BTO thin films. Angle-resolved x-ray photoelectron spectroscopy studies show that excess barium accumulates at the surface in the form of a barium-rich surface layer referred to here as  $\text{BaO}$ . For titanium-rich growth condition, the layer assumed stoichiometric bulk BTO values. The excess barium accumulated at the surface was removed with methanol sonication.

Barium titanate thin films were shown to self-assemble when excess barium was provided during co-deposition. A systematic comparison of 5 nm thick BTO films grown comparing the shuttered RHEED and co-deposition growth approaches was performed to prove

that excess barium doesn't incorporate into the film but only as BaO at the surface. Both growth approaches produce identical out-of-plane lattice parameter, Ti/Ba ratio, and piezoelectric coefficients. An enhancement in the  $d_{33}$  for the 5 nm thin films compared to the 40 nm thin films was also observed. The compressive strain on 5 nm thin films enhanced the polarization over fully relaxed 40 nm thin films.

## **Acknowledgements**

I appreciate the opportunity that God has given me to observe a piece of his wonderful creation. Every step of the way I've been able to observe His intelligence and beauty of a carefully created universe. He has also used this process to change me through the interaction of many people.

My wife, Tiffany, has been an unyielding force of encouragement during this process. Without her, I would not have had the courage to face many fears and become a better scientist. Her creativity and diligence inspire me.

To my daughters, Lilia & Elise, thanks for being a breath of joy when I was home. You helped remind me of the joy of discovery. I loved helping you all explore new sights, sounds and sensations. I look forward to accompanying your journey of learning.

Dr. Greg Salamo, I cannot express enough thanks for many lessons. While no one has challenged me more, I am better for it. Your intense focus on the present has always been an inspiration for me and a critical skill I am to keep refining. My passion and curiosity has never been higher because of how you see the beauty in every piece of data. I have been grateful for the ten years I've spent working with you.

The joy of working on my PhD for ten years has been the number of people that have taught and inspired me along the way. Mohammad Zammani, my fellow grad student who is a fierce friend and sees the science of every situation. Robert Sleezer, an enthusiastic teacher who has never ceased to provide motivating perspective. Zhaoquan Zeng, the postdoc who taught me how to grow oxides and started this journey. Vasyl Kunets, who got me my start in research and was always willing to talk. Morgan Ware, who helped me find that leak among many other important aspects of science. Yuriy Mazur, who always cared enough to tell me how to improve

my scientific approach. Mourad Benamara, who has helped me not get too stressed out along the way. Renee Hearon, who was a light in some of my darkest times. Ken Vickers, who always saw more in me than I did and taught me how to value people. Rick Wise, who taught me how to focus and finish.

I gratefully acknowledge the funding agencies that have supported me in finishing the work in this dissertation. I would like to thank the National Science Foundation, Department of Defense: Army Research Laboratory, Arkansas Space Consortium and the Walton Foundation for the funding they have provided. The work in this dissertation has been supported by the National Science Foundation under Grant Numbers EEC-1138248, IIA-1457888, EEC-0438704, ECS-0337484, SA 200618, ECCS-0702187, EEC-1138248, 16-EPS3-0011, DMR1309989, and ECCS1128462 and the Department of Defense: Army Research Laboratory W911ND-08-2-0006, W911NF-05-1-0353, DAAD19-03-2-0017, and W911NF-08-2-0006. Additionally, the Arkansas Grant Space Consortium and Walton Foundation provided funding through the awards of an Arkansas Space Grant Consortium Fellowship and a Walton Distinguished Associate Fellowship. Without the support from these funding agencies, I would not have had the opportunity to discover this new growth approach.

## **Dedication**

I dedicate this dissertation to my wife, Tiffany, the most creative, logical problem solver I know.



## Table of Contents

Chapter 1: Barium Titanate.....	1
1.1 Barium Titanate Properties .....	3
1.2 Stoichiometric Growth of Barium Titanate .....	8
1.2.1 Off-stoichiometric Growth of Barium Titanate .....	11
1.2.2 MBE Growth of Barium Titanate .....	12
1.3 Impact of BTO Stoichiometry on Ferroelectricity.....	18
Chapter 2: Oxide Molecular Beam Epitaxy.....	19
2.1 Molecular Beam Epitaxy .....	20
2.1.1 Oxygen in Ultrahigh Vacuum .....	23
2.1.2 Heating and Oxygen .....	28
2.1.2.1 Silicon Carbide Heater Upgrade .....	29
2.1.2.2 Substrate Temperature Monitoring.....	31
2.1.3 Flux Monitoring .....	34
2.1.3.1 Flux Monitoring .....	35
2.1.3.2 Shuttered RHEED.....	37
2.2 Calibration .....	38
2.3 Barium Titanate .....	39
Chapter 3: Materials Characterization of Barium Titanate Thin Films .....	46
3.1 Thin Film Structure.....	47
3.1.1 X-ray diffraction .....	47
3.1.2 XRD Results .....	50
3.2 Thin Film Surface Composition .....	55
3.2.1 X-ray Photoelectron Spectroscopy .....	55
3.2.2 XPS Results .....	62
3.2.3 Barium-Rich Surface Layer .....	64

3.3 Thin Film Morphology .....	65
Chapter 4: Ferroelectric Properties of Barium Titanate Thin Films .....	68
4.1 Piezoresponse Force Microscopy .....	68
4.2 Quantitative PFM.....	72
4.2.1 Background Measurement .....	74
4.2.2 Measuring the Piezoelectric Coefficient .....	77
4.3 Impact of Surface Chemistry on Piezoresponse .....	79
4.3.1 Carbon Surface Layer .....	80
4.3.1.1 Solvent Cleaning Optimization.....	81
4.3.1.2 Oxygen Plasma Cleaning Optimization.....	83
4.3.2 Surface Charge.....	85
4.4 Tip Force.....	85
4.5 Probe Effects.....	88
4.6 Comparing Growths using Quantitative Piezoforce Microscopy .....	91
Chapter 5: Results & Discussion .....	93
5.1 Characterizing BTO Films under Off-stoichiometric Growth Conditions .....	93
5.1.1 Off-stoichiometric RHEED Oscillations .....	93
5.1.2 Structure and Stoichiometry of BTO Films .....	98
5.1.3 Ferroelectric properties of BTO films.....	101
5.2 Self-Assembly of BTO films .....	103
5.2.1 Barium-Rich Co-Deposition RHEED Oscillations.....	106
5.2.2 Stoichiometry of Barium-Rich Co-Deposited BTO Films .....	107
5.2.3 Ferroelectric Properties of Self-Assembled BTO films.....	111
Chapter 6: Conclusions & Future Work .....	113
6.1 Further Evaluation of Self-Assembled Barium Titanate Thin Films.....	113
6.2 Barium Titanate Quantum Dots.....	114

6.3 Flexoelectricity and Friction .....	116
6.4 Ferroelectric Properties as a Function of BTO Thickness .....	118
References .....	120
Appendix A: Description of Research for Popular Publication .....	135
Appendix B: Executive Summary of Newly Created Intellectual Property .....	137
Appendix C: Potential Patent and Commercialization Aspects of listed Intellectual Property Items .....	138
C.1 Patentability of Intellectual Property (Could Each Item be Patented) .....	138
C.2 Commercialization Prospects (Should Each Item Be Patented) .....	138
C.3 Possible Prior Disclosure of IP .....	139
Appendix D: Broader Impact of Research .....	140
D.1 Applicability of Research Methods to Other Problems .....	140
D.2 Impact of Research Results on U.S. and Global Society .....	140
D.3 Impact of Research Results on the Environment .....	141
Appendix E: Microsoft Project for PhD MicroEP Degree Plan .....	142
Appendix F: Identification of All Software Used in Research and Dissertation Generation .....	144
Appendix G: All Publications Published, Submitted and Planned .....	146

## List of Figures

Figure 1. The breadth of properties in oxide materials originates in its crystal structures. ....	1
Figure 2. Perovskites have a wide variety of atoms combinations for $ABX_3$ perovskites. ....	2
Figure 3. Spatial filling of BTO unit cell and the relative sizes of barium, titanium and oxygen atoms. ....	4
Figure 4. Bonding strength between Ti-O and Ba-O in BTO unit cell. ....	5
Figure 5. Relationship of atomic displacements to polarization on a hysteresis loop. ....	6
Figure 6. Polarization is stabilized by surface charge and arranged into domains to minimize energy. ....	7
Figure 7. Full BaO-TiO <sub>2</sub> phase diagram. ....	8
Figure 8. The stable phases formed with excess barium ( $Ba_2TiO_4$ ), stoichiometry ( $BaTiO_3$ ) and excess titanium ( $BaTi_2O_5$ ) stable crystal structures. ....	9
Figure 9. Modified BaO-TiO <sub>2</sub> Phase Diagram near 50%. ....	10
Figure 10. GaAs adsorption-controlled growth window. ....	13
Figure 11. Superlattice of BaO and TiO <sub>2</sub> layers. ....	15
Figure 12. BaTiO <sub>3</sub> adsorption-controlled growth window. ....	16
Figure 13. MBEs connected via transfer line. ....	19
Figure 14. Oxide MBE concept. ....	21
Figure 15. Oxide MBE chamber with hot titanium cell. ....	22
Figure 16. Mean free path of cations in oxygen. ....	23
Figure 17. Mean free path concept. ....	24
Figure 18. Oxygen pressure required to oxidize cations. ....	25
Figure 19. Comparison of oxygen source potency. ....	26
Figure 20. Oxygen plasma intensity map. Low plasma intensity (light blue) created oxygen vacancies in BTO. While increasing plasma intensity (red), generated stoichiometric BTO. ....	27
Figure 21. Tantalum heater (left) oxidizes while SiC (right) can operate in high heat and oxygen. ....	29

Figure 22. XPS results comparing backside of STO sample after operating SiC at 14.5 Amps (Red) and 18 Amps (Blue).....	30
Figure 23. STO substrate preparation for growth and optical monitoring.....	32
Figure 24. Temperature comparisons of blackbody, thermocouple, and bandedge. ....	33
Figure 25. Barium flux changes from sequential growths.....	36
Figure 26. (A) Shuttered RHEED oscillations with (B) high intensity of BaO layer and (C) low intensity of TiO <sub>2</sub> layer, results in (D) smooth surface.....	37
Figure 27. Temperature oscillations correlated to RHEED oscillations.....	39
Figure 28. Barium rich oscillations for (top) OG029 (middle) OG033 and (bottom) OG034. ....	40
Figure 29. Titanium-rich oscillations (TL) OG031 (TR) OG032 (ML) OG035 (MR) OG036 (BL) OG037.....	43
Figure 30. Comparing RHEED envelopes of (left) barium rich to (right) titanium rich.....	45
Figure 31. X-ray diffraction excites spherical waves (left) and constructive interference between planes occurs at certain angles.....	47
Figure 32. XRD simulations comparing the FWHM of 5 and 50 nm thick films. The 5 nm film has a FWHM that is six times larger than the 50 nm FWHM.....	48
Figure 33. Gaussian fits of the simulated 5 nm and 50 nm films to determine the FWHM at each thickness. ....	49
Figure 34. 2θ-ω scans of strontium titanate thin films grown with various Ti/Sr shutter time ratios.....	50
Figure 35. SrTiO <sub>3</sub> out-of-plane lattice parameter change with shutter time ratio. ....	51
Figure 36. XRD 2θ-ω curves for all BTO films. ....	53
Figure 37. Out-of-plane lattice parameter of BTO films as function of shutter time ratio.....	54
Figure 38. Primary concepts of x-ray photoelectron spectrometer.....	56
Figure 39. Binding energy (BE) of an electron is defined as the energy difference from the core level to the fermi level. The BE uniquely identifies an atom chemically.....	57
Figure 40. Partial XPS survey spectrum of a BTO film. ....	58
Figure 41. Oxygen curve fit showing surface oxygen and BTO oxygen.....	59

Figure 42. Barium 3d <sub>5/2</sub> curve fit showing two chemical environments: BaO and BTO. ....	60
Figure 43. Barium rich (blue) vs barium poor (red) comparison of Ba 3d <sub>5/2</sub> peak. ....	62
Figure 44. Cation ratio change before and after methanol cleaning. ....	64
Figure 45. Comparison of Ba3d <sub>5/2</sub> Curve fitting showing increase in surface BaO peak when changing to more surface sensitive angle (15°). ....	64
Figure 46. Basic components of a Bruker Dimension 3100 AFM head. ....	65
Figure 47. Comparison of morphology based on barium-rich vs. titanium-rich. ....	66
Figure 48. A PFM experiment consists of poling with DC voltage (left) and sensing the poled regions with AC voltage and a lock-in detector. ....	69
Figure 49. Piezoresponse hysteresis loops (top) phase and (bottom) amplitude. ....	70
Figure 50. Piezoresponse data from a BTO film poled with -3 VDC (dark area on left) and +7 VDC (bright area on right). ....	71
Figure 51. Many factors contribute background noise; vector analysis of PFM response helps to identify those sources. ....	72
Figure 52. Piezoresponse of glass as function of V <sub>ac</sub> frequency. ....	74
Figure 53. Time and distance in PFM measurement showing background noise. ....	75
Figure 54. Slope of repulsive region in deflection sensitivity curve to extract piezoelectric coefficient. ....	76
Figure 55. Measuring d <sub>33</sub> from difference in c+ and c- domains. ....	78
Figure 56. (a) Piezoresponse of OG029 immediately after growth and (b) height. Three months later, (c) No piezoresponse existed and (d) large height features observed in the poled area. ....	79
Figure 57. Time dependence of carbon accumulating on BTO surface. ....	81
Figure 58. Bulk BTO height (left) and piezoresponse (right). ....	82
Figure 59. Oxygen plasma intensity map (top). Surface morphology at low intensity (bottom left) and high intensity (bottom right). ....	83
Figure 60. Piezoresponse of solvent cleaned (TL) vs plasma cleaned (BL). The d <sub>33</sub> (TR) changes primarily because of surface charge background (BR). ....	84
Figure 61. Effect of set point (tip force) on piezoelectric coefficient. ....	86

Figure 62. Changes in set point (top left) result in changes in piezoresponse (top right). $d_{33}$ relationship with tip force (bottom). .....	87
Figure 63. Less than 20% variation in piezoelectric coefficient when tip force was held constant. ....	88
Figure 64. Change in piezoelectric coefficient with change in probe.....	89
Figure 65. Probe engagement changed the $d_{33}$ value.....	90
Figure 66. SEM images show difference in shape between two probes.....	91
Figure 67. Comparing barium-rich (A) and barium-poor RHEED oscillations (B). ....	96
Figure 68. Surface roughness as function of stoichiometry.....	97
Figure 69. Out-of-plane lattice parameter based on surface stoichiometry. ....	98
Figure 70. Stoichiometry change after surface cleaning.....	99
Figure 71. Lattice parameter and stoichiometry (Ti/Ba) have bulk BTO values when grown in barium-rich condition.....	100
Figure 72. Piezoelectric coefficient as function of $c$ (above) and Ti/Ba (below). ....	102
Figure 73. Self-assembly of barium titanate. ....	103
Figure 74. Barium-rich oscillations co-deposition (top) shuttered RHEED (bottom).....	106
Figure 75. (A) Ba $3d_{5/2}$ peak, (B) TOA, (C) cleaning, (D) XRD. ....	108
Figure 76. Piezoelectric Stoichiometry before (A) and after methanol sonication (B). ....	110
Figure 77. Piezoelectric coefficient comparison between growth approaches and thickness. ...	112
Figure 78. Spotty RHEED pattern of BTO grown on MgO (A) and with excess Ba on STO:Nb (B). AFM confirmed dots formed (C) that showed unique piezoresponse on dots (D). ....	115
Figure 79. Gradient force (left) applied to poled region. Polarization switch due to mechanically bending the film (middle). Graphic showing how bending induces polarization in BTO (right). ....	116
Figure 80. Three different regions of BTO were poled both electrically and mechanically (top). The friction plot indicated the mechanically poled region shows lowest friction (bottom).....	117

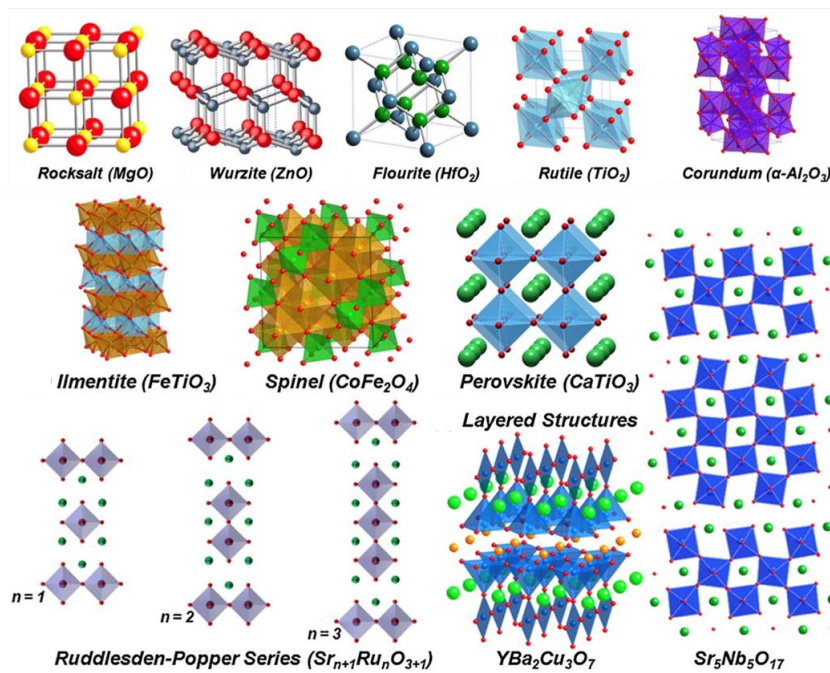
## List of Tables

Table 1. Comparison of the properties of BaTiO <sub>3</sub> constituents and related phases.....	11
Table 2. SrTiO <sub>3</sub> calibration sample growth parameters from left to right are strontium cell temperature, strontium shutter time open, titanium cell temperature, titanium shutter time open and ratio of titanium to strontium shutter times. ....	38
Table 3. BaTiO <sub>3</sub> samples grown to identify barium-rich and titanium-rich growth conditions. ..	42
Table 4. SrTiO <sub>3</sub> XRD analysis as function of growth conditions.....	52
Table 5. BaTiO <sub>3</sub> XRD analysis as a function of growth conditions. ....	54
Table 6. Summary of XPS analysis of a BaTiO <sub>3</sub> thin film. ....	61
Table 7. BaTiO <sub>3</sub> XPS analysis (BC – Before Cleaning, PC – Post Cleaning). ....	63
Table 8. BaTiO <sub>3</sub> material analysis of barium rich and titanium rich thin films.....	94
Table 9. Substrates for BTO dot growth.....	114



## Chapter 1: Barium Titanate

Oxide materials are the most abundant on earth [1], [2]. They also contain a wide range of properties including ferroelectricity [3]-[7], superconductivity [8]-[14], and ferromagnetism [15]-[20], as well as being multiferroic [21]-[29] and more. This variety of properties oxide materials exhibit is related to their structural diversity [30] (Figure 1). Understanding how oxides form is the key to discovering the origin of their properties.



**Figure 1.** The breadth of properties in oxide materials originates in its crystal structures [30].

Of the oxides, the perovskite is the most common crystal structure found in the earth's crust [1]. Specifically, bridgmanite, a perovskite mineral, makes up 92% of the earth's crust [1]. The first perovskite to be discovered was  $CaTiO_3$  in 1839 [31], [32]. One of the most beautiful aspects of the crystal structure is the large number of chemicals that can occupy different sites [33], [34]. Perovskites have three unique sites (A, B & X), that allow over 10,000 different combinations [33] of unique materials (Figure 2). For this reason, the perovskites have been one



$$t = \frac{r_{A+rO}}{\sqrt{2}(r_B+rO)} \quad (\text{Equation 2})$$

The tolerance factor predicts which combination of cations and anions form a stable perovskite structure, purely on size. While ideal cubic perovskites like SrTiO<sub>3</sub> have  $t \sim 1$ , deviations lead to different crystal structures. For example, CaTiO<sub>3</sub> has a tolerance factor in the range of  $0.71 < t < 0.8$  and has an orthorhombic crystal structure. Perovskite structure stability is governed by this simple size relationship. Another requirement for stable perovskites is charge neutrality. For example, in bismuth ferrite [50]-[52], Bi has a valence state of 3+ and Fe has a valence state of 3+ which balances with the three O that have valence state of 2-, thus resulting in a neutral unit cell.

Another reason for perovskite diversity is that it's a crystal structure formed from two different crystal structures of AX and BX<sub>2</sub>. In Figure 1 [30], AX could be a rock salt [53]-[55] and the BX<sub>2</sub> could be a rutile crystal structure [56]-[58]. The fundamental building block of the rutile crystal structure is the octahedral [59], [60]. For example, titanium dioxide has a titanium at the center bonded to six different oxygen atoms. It is this octahedral that meshes into the rock salt crystal structure to form a perovskite. Most rock salt crystals are ionically bonded to each other, while the octahedral are covalently bonded to each other. The merger of two differently bonded lattices into the perovskite is the reason for rich diversity in its properties. The perovskite that was the focus of this research was barium titanate. Furthermore, the principles about perovskite formation can be used to guide new MBE growth approaches for BTO.

### 1.1 Barium Titanate Properties

Barium titanate is a A<sub>2</sub>B<sub>4</sub>O<sub>3</sub> perovskite. Barium is the A-site cation with a valence state of 2+ and an ionic radius of 2.24 Å [61]. Titanium is the B-site cation valence state 4+ and an ionic radius of 1.45 Å. Oxygen has a valence state of 2- and ionic radius of 0.74 Å. From these

numbers, the tolerance factor for BTO is 0.96 which is close to one, indicating a very stable perovskite. Figure 3 represents the relative size of these atoms and how they would fill a tetragonal unit cell. There is no room for interstitial cations.

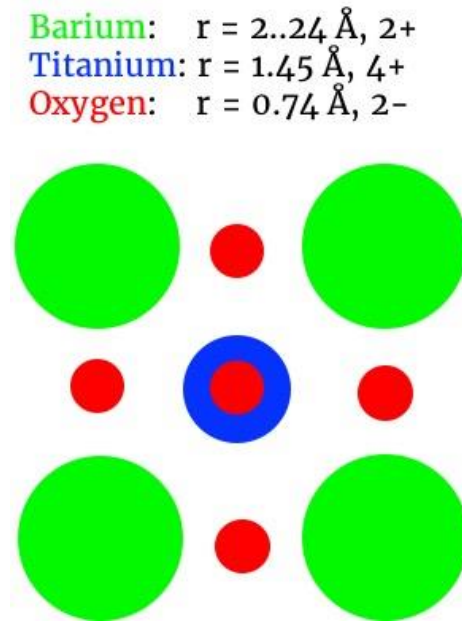


**Figure 3.** Spatial filling of BTO unit cell and the relative sizes of barium, titanium and oxygen atoms.

At room temperature, BTO has a non-centrosymmetric, tetragonal structure that is the foundation of its ferroelectricity. In Figure 4, the solid lines represent the stronger covalent bonds between the titanium and oxygen atoms. The dashed lines represent the weaker ionic bonds between the barium and oxygen atoms.

Barium titanate is a high-k dielectric ( $\epsilon_{\text{BTO}} = 3000$ ) and ferroelectric material [31]. A ferroelectric material is characterized by a reversible remnant polarization. The polarization is due to the off-centering of the titanium atom in the B-site of barium titanate. When an electric field opposite in sign to the current polarization state and larger in magnitude than the coercive field is applied, the off-centering of the titanium is reversed and thus the polarization is reversed.

Figure 5 shows a signature hysteresis curve for a ferroelectric. Six remnant polarizations are possible along the axes. The Ti atomic placement shift is about 10 pm [62], [63] and is able to create a polarization of  $\sim 25 \mu\text{C}/\text{cm}^2$ . The other signature of a hysteresis loop is the electric field or voltage required to switch the polarization also known as the coercive field.

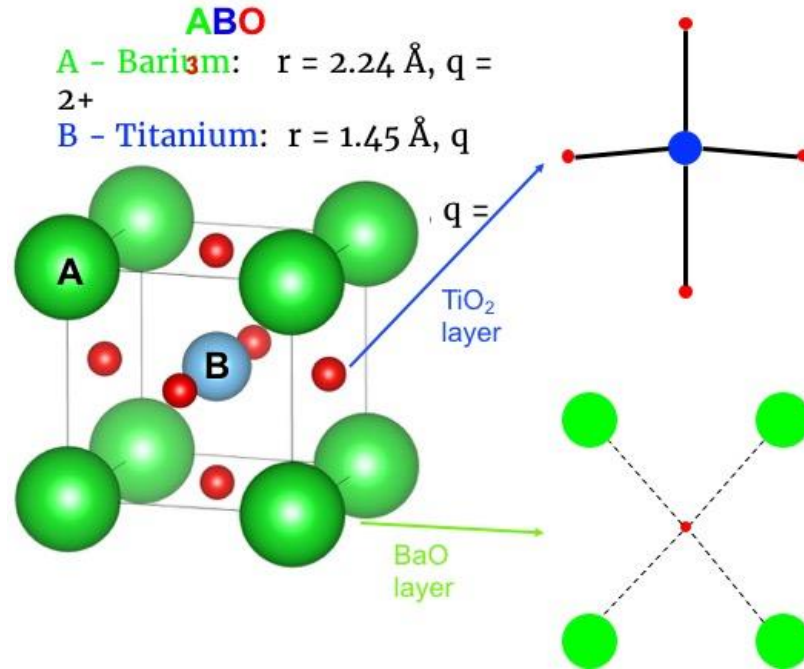


**Figure 4.** Bonding strength between Ti-O and Ba-O in BTO unit cell.

At the nanoscale, the coercive field is obtained with low voltage ( $<5 \text{ V}$ ) at room temperature. The low voltage makes thin films attractive for low power, non-volatile memory devices [5], [64], [65]. Yet, controlling the stoichiometry of BTO for the growth of thin films is the challenge. Improving stoichiometry control will lead to lower defect densities and, thus, higher performing materials (lower losses and less fatigue) [5], [64]-[66].

Ferroelectric domains are regions within a material with the same polarization. As an example, there might exist a domain with polarization pointing in the  $+z$ -direction ( $c+$ ) and a domain with polarization pointing in  $-z$ -direction ( $c-$ ). When these two domains are neighboring

each other, they are separated by 180° domain walls. Domains form naturally in ferroelectrics to reduce the depolarizing field and minimize the energy of the material. The domain size is proportional to the square root of thickness [32].

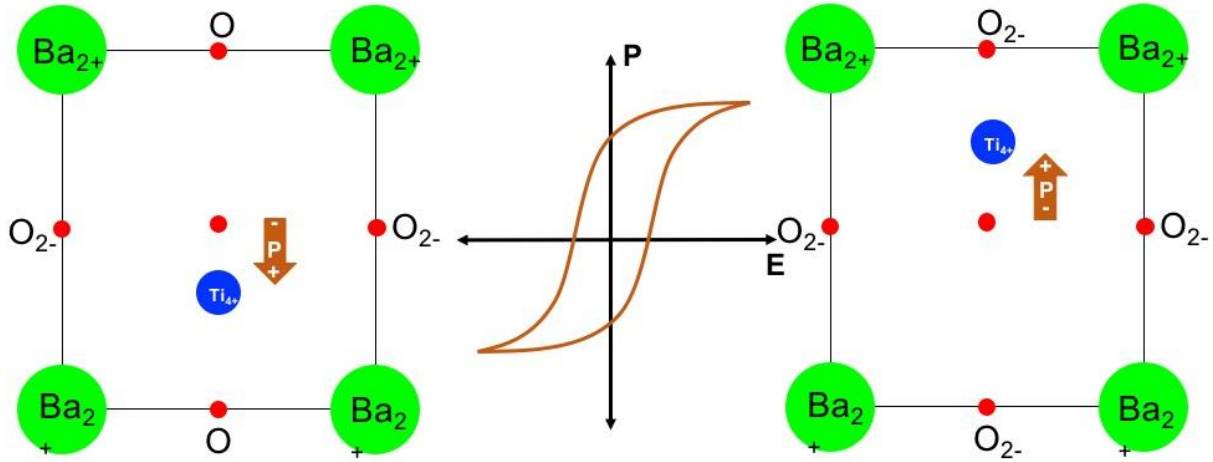


**Figure 5.** Relationship of atomic displacements to polarization on a hysteresis loop.

Surface charge plays an important role in stabilizing the polarization (Figure 6) and formation of domains (area of same polarization). When a domain is created, surface charges (free electrons, ions) rearrange on the surface to screen and stabilize the domains [32], [48], [67]. When a domain is switched, the surface charge rearranges to match the new polarization. Domain switching is sensitive to defects [68]-[70].

The bonding within BTO determines defect formation energies. Understanding the bonding helps determine which kind of defect is more likely to form. The BaO and TiO<sub>2</sub> planes show the distances between atoms. The titanium atom has six oxygen atoms as nearest neighbors; at room temperature, four are a distance  $a/2$  away and those two in the polarization direction are at  $c/2$ . In addition to the distance away, the charge state of titanium and oxygen, 4+ and 2- makes this a strong covalent bond. However, the TiO<sub>6</sub> octahedra is not completely charge

balanced; the net charge is -2. The barium atoms are  $a/\sqrt{2}$  away from the oxygen that would still like to donate two electrons to become stable. The nearest barium atoms can share a quarter of an electron each and charge compensate the  $\text{TiO}_6$ . Since barium has a charge state of  $2+$ , it would rather give up its electrons. Thus, the barium is weakly ionically bonded to the rest of the structure. The difference in bonding between the cations results in different defect formation energies [71]. For instance, in order to form a barium vacancy  $\sim 20$  eV is required while  $\sim 80$  eV is required to form a titanium vacancy.

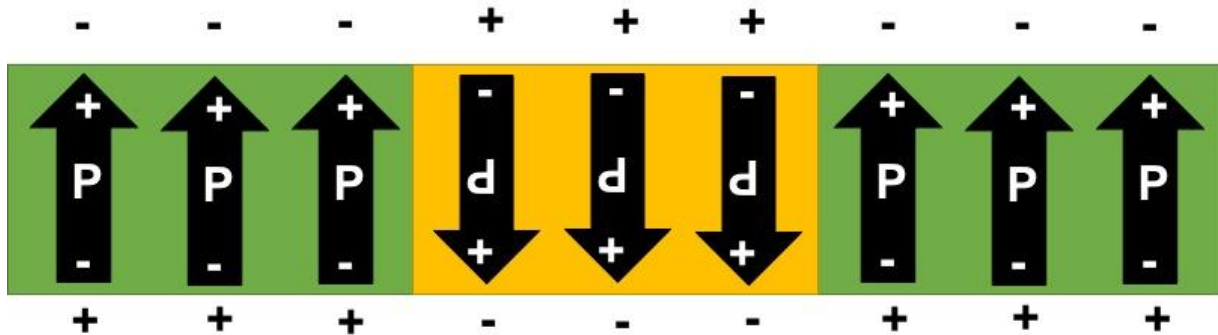


**Figure 6.** Polarization is stabilized by surface charge and arranged into domains to minimize energy.

Changes in stoichiometry of barium titanate change its ferroelectric properties [72], [73]. For example, replace barium with strontium in BTO and the remnant polarization and losses decrease [74]-[77]. On the other hand, create a cation vacancy in strontium titanate and ferroelectricity is created [78], [79]. Researchers have modified barium titanate to enhance its polarization through strain [80]-[83]. Oxygen vacancies lead to conductive BTO with no ferroelectricity [84]-[86]. Understanding the impact of cation defects on the ferroelectric properties is relatively unexplored [87]-[89].

Understanding how a material is bonded is the key to understanding how to grow the material [90], [91]. Both the Goldschmidt tolerance factor (Eqn. 2) along with  $\text{BaO-TiO}_2$  phase

diagrams provide insight into a new way to control the stoichiometry of barium titanate. Those principles are discussed in this dissertation and new ways to use them in molecular beam epitaxy growth are proposed.

## 1.2 Stoichiometric Growth of Barium Titanate

Bulk barium titanate has been made since the 1940s and the improvements in bulk growth techniques has greatly reduced point defects [92]. Understanding the BaO-TiO<sub>2</sub> phase diagram [71], [93], [94] in Figure 7 gives insight into controlling the stoichiometry of BTO. Pure BaTiO<sub>3</sub> forms precisely when 50% of TiO<sub>2</sub> is mixed with 50% BaO. Deviation from 50% results in different phases or mixed solid solutions. In contrast to the InAs-GaAs phase diagram [95] where varying the %InAs simply alloys into the same crystal structure for the whole range. The major difference is the mixing of two different phases entirely: BaO (rock salt) and TiO<sub>2</sub> (rutile). Understanding what phases form for both the excess BaO and excess TiO<sub>2</sub> provided insights for developing a new growth approach.

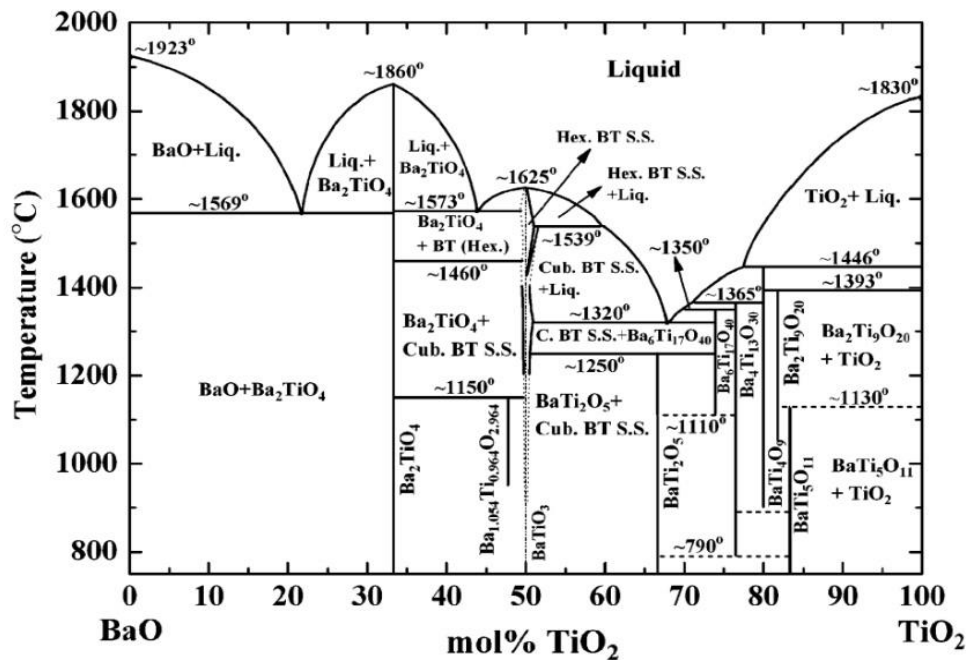
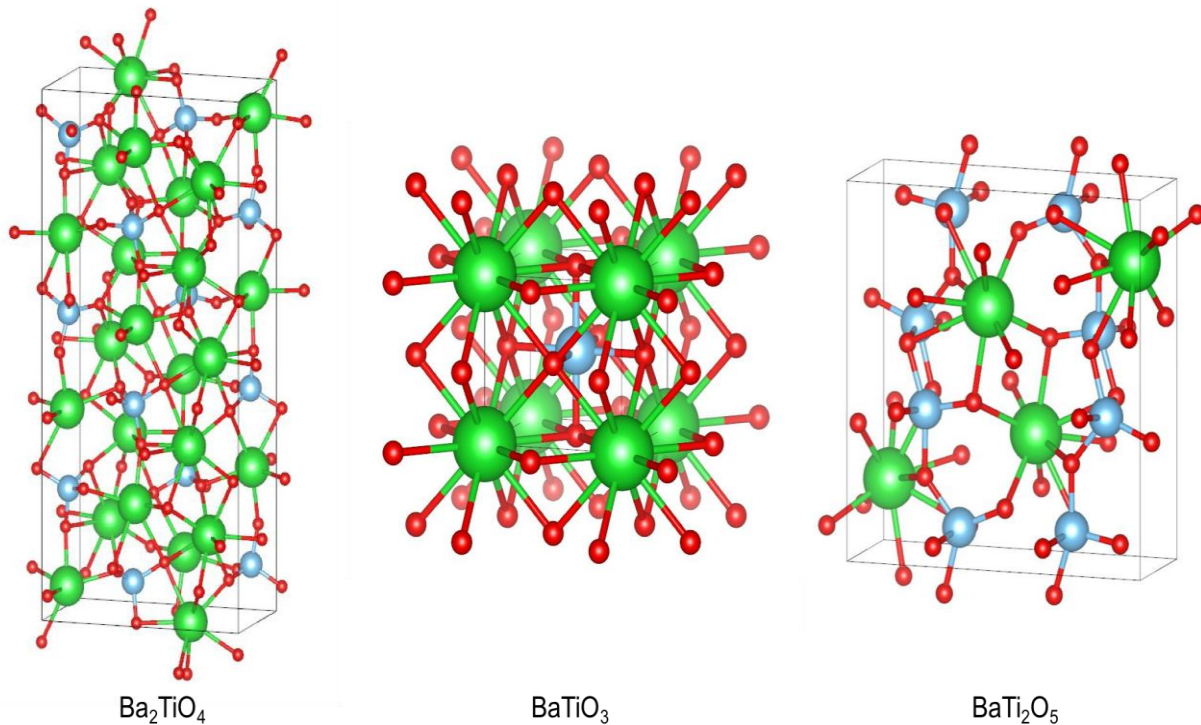


Figure 7. Full BaO-TiO<sub>2</sub> phase diagram [71].



Other phases and solid solutions form near  $\text{BaTiO}_3$  on both the barium rich and titanium rich side. On the barium rich side bordering 50%  $\text{TiO}_2$ ,  $\text{Ba}_2\text{TiO}_4$  begins to form around 1570 °C and is stable through room temperature. On the titanium side,  $\text{BaTi}_2\text{O}_5$  is the stable compound that forms below 1250 °C; however, it's not phase pure and a BTO solid solution can coexist in a stable structure. These crystal structures are illustrated in Figure 8.



**Figure 8.** The stable phases formed with excess barium ( $\text{Ba}_2\text{TiO}_4$ ), stoichiometry ( $\text{BaTiO}_3$ ) and excess titanium ( $\text{BaTi}_2\text{O}_5$ ) stable crystal structures.

While the chemical formula simply incorporates an extra  $\text{BaO}$  or  $\text{TiO}_2$  layer, the crystal structure changes are not as simple as shown in Figure 8. In  $\text{SrTiO}_3$ , the extra  $\text{SrO}$  layer simply stacks on top, forming a Ruddelston-Popper phase [53], [59], [96], [97]. Below 1200 °C, both sides on the BTO line form stable phases. However, there is asymmetry in the barium rich and titanium rich sides. On the titanium rich side, a BTO solid solution forms with  $\text{BaTi}_2\text{O}_5$ . On the barium rich side, a single phase of  $\text{BaTiO}_4$  phase forms and has been shown to segregate from

BaTiO<sub>3</sub> [71]. Below 1400 °C there is not a new phase on either the barium rich or barium poor side.

Furthermore, there is additional asymmetry to either side, highlighted by the dashed line near 50%TiO<sub>2</sub> (Figure 9). The titanium rich side is wider since barium vacancies required to accommodate the excess titanium are easier to remove with an energy of ~20 eV [71]. On the other hand, the energy required to form a titanium vacancy to accommodate a barium atom is nearly four times higher at ~80 eV [71].

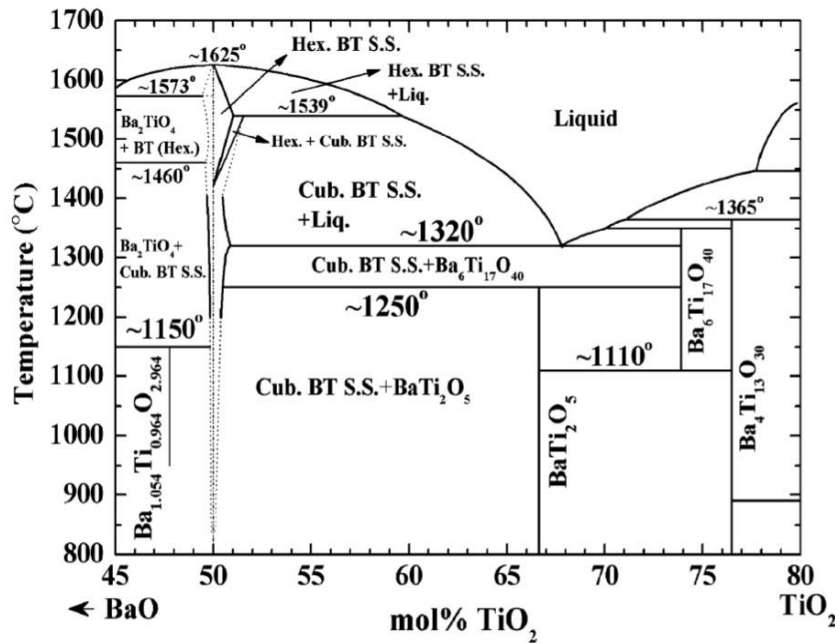


**Figure 9.** Modified BaO-TiO<sub>2</sub> Phase Diagram near 50% [71].

The dashed lines in the BaO-TiO<sub>2</sub> phase diagram (Figure 9) represent the solubility of excess barium oxide and titanium dioxide as a function of temperature. Kui et al. experimentally measured the solubility to be around 1% [71] in the 1200-1400 °C range. The solubility of BaO and TiO<sub>2</sub> can be estimated from the work of Kui et al. as a function of temperature. At MBE growth temperatures, 600-800 °C, the solubility is estimated to be less than 100 ppm, which is better stoichiometry control than the shuttered RHEED growth approach [98]. The low solubility

on the excess barium side with a single phase could provide a mechanism for controlling stoichiometry during growth.

Determining the likelihood of a barium atom substituting for a titanium atom must be considered if excess barium will be provided during growth. From a size perspective, the Goldschmidt tolerance factor predicts an unstable perovskite structure if barium sits in the A site. Using Equation 2 for barium and substituting  $r_A = r_B$ ,  $t = 0.774$  which is no longer predicted to be a stable tetragonal or cubic perovskite. Also, the unit cell with the barium substitution would not be charge neutral. A prerequisite for barium substitution is the creation of a titanium vacancy, which is four times higher in energy cost than a barium or oxygen vacancy. All of this information coupled with the BaO-TiO<sub>2</sub> phase diagram suggests excess barium does not incorporate into the lattice as a defect.

**Table 1.** Comparison of the properties of BaTiO<sub>3</sub> constituents and related phases.

	<b>Crystal</b>	<b>Lattice Constants</b>	<b><math>\epsilon</math></b>	<b><math>P_r</math> (<math>\mu\text{C}/\text{cm}^2</math>)</b>	<b><math>E_c</math> (kV/cm)</b>
<b>BaO</b>	Rock salt	$a = b = c = 3.97$	34	N/A	N/A
<b>TiO<sub>2</sub></b>	Rutile	$a = 2.97$ $b = c = 4.652$	170	N/A	N/A
<b>BaTiO<sub>3</sub></b>	Perovskite	$a = b = 3.99$ $c = 4.04$	3000	40	~1
<b>Ba<sub>2</sub>TiO<sub>4</sub></b>	Monoclinic	$a = 6.24$ $b = 7.78$ $c = 10.68$	40	N/A	N/A
<b>BaTi<sub>2</sub>O<sub>5</sub></b>	Orthorhombic	$a = 3.94$ $b = 10.52$ $c = 11.01$	65	7	8

### 1.2.1 Off-stoichiometric Growth of Barium Titanate

Both the BaO-TiO<sub>2</sub> phase diagram and the Goldschmidt tolerance factor suggest that off-stoichiometric growth conditions could be used to control stoichiometry. Understanding how off-

stoichiometric growth conditions impact the stoichiometry and material properties of the resulting material is important in assessing how the excess cations incorporate into the film. A study of off-stoichiometric ratio of BTO reactants formed lower tetragonality and dielectric constant as the ratio of Ti/Ba varied from unity [99] because the excess phase segregated. BaO, TiO<sub>2</sub>, Ba<sub>2</sub>TiO<sub>4</sub> and BaTi<sub>2</sub>O<sub>5</sub> all have lower dielectric constants and remnant polarizations than BTO (Table 1). The BaTiO<sub>3</sub> and Ba<sub>2</sub>TiO<sub>4</sub> were physically separated into different regions [100], [101] as opposed to intermixing.

Moving on to thin film deposition, pulsed laser deposition (PLD) has been used to investigate off-stoichiometric growth conditions of barium titanate [102], [103]. In PLD, grown BTO films phase segregation was observed in the barium rich condition. However, the phases were mixed throughout the film which would have significant impact on the performance of a capacitor since there would be multiple phases.

A large part of research on MBE growth of BTO has simply focused on controlling the stoichiometry through precise cation deposition. Only a few reports on off-stoichiometric growth of barium titanate using MBE have been published [88], [104]. One study found that over a large range of Ti/Ba growth ratios for BTO films grown on Ge, tetragonal structure is preferred over other phases [105].

### 1.2.2 MBE Growth of Barium Titanate

Controlling the stoichiometry is the key to unlocking the best properties of a material. The better the control, the better the properties [106], [107]. One of the key advantages of molecular beam epitaxy is the sub-monolayer control of atomic deposition and the precise doping profiles. However, while MBE uses these advantages to produce sharp interfaces for heterostructures, the stoichiometry of individual layers does not rely on the precise deposition of

atoms to achieve the most stoichiometric material. Rather, these features are used to discover the growth conditions that automatically lock-in stoichiometry. For example, gallium arsenide based heterostructure has produced the world's highest recorded mobility [107] because the layers can be grown in an adsorption-controlled window. An adsorption-controlled window is a range of substrate temperatures and atomic pressures where the atoms form stoichiometric solids and the excess cations desorb off the surface (Figure 10). Individual layers of the heterostructure grown within this window rely on nature to control the stoichiometry in order to automatically achieve the lowest defect concentrations in that material.

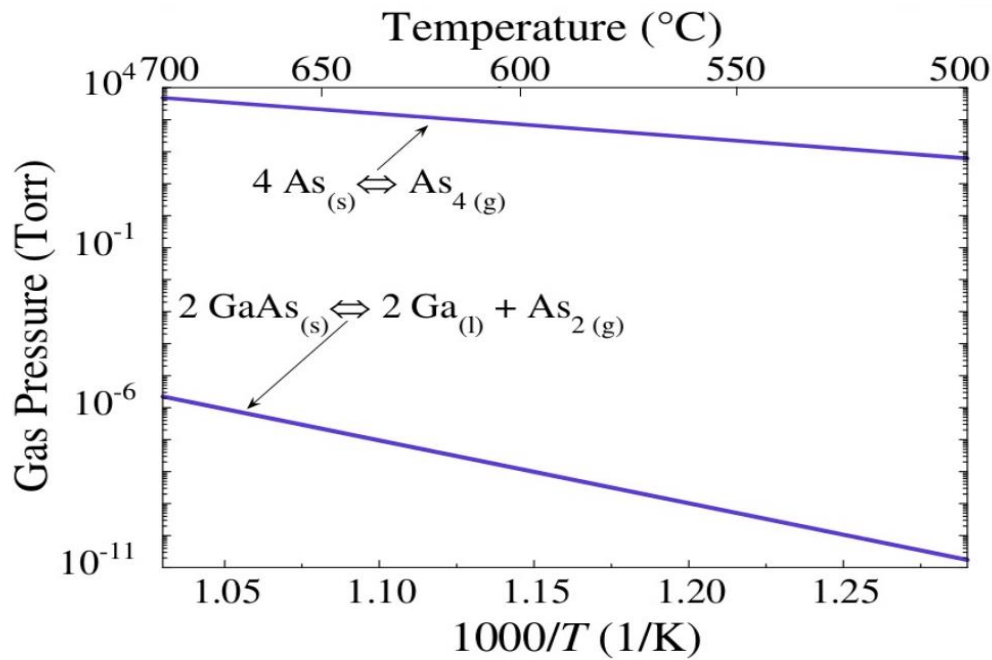


**Figure 10.** GaAs adsorption-controlled growth window [108].

Alloying in MBE combines both adsorption-controlled growth (Figure 10) and precise control over the growth rates. In ternary semiconductors, such as  $\text{In}_x\text{Ga}_{1-x}\text{As}$ , the ratio is linked because indium and gallium atoms can only sit in the gallium site of the zinc blende crystal structures when grown under arsenic-rich conditions. The stoichiometry of the film is then tuned by adjusting the growth rates of indium and gallium. The ratio of growth rates dictates the ratio

of cations incorporated into the film. Considering the case of  $x = 0.35$  for  $\text{In}_x\text{Ga}_{1-x}\text{As}$ , the indium growth rate would be 0.35 ML/s while the gallium would be set to 0.65 ML/s and, under an arsenic rich condition, the cations will take the correct amount of arsenic and the excess will desorb off the surface.

Molecular beam epitaxy is the technique of choice for discovering how a material grows. When the growth conditions of any material are found that naturally allow the material to crystallize, the highest quality and performance of that material follows. For example, MBE has been used to discover a large adsorption-controlled growth window (Figure 10) to lock-in the stoichiometry of GaAs [34], [98] obtaining the highest recorded mobility for arsenide-based heterostructures. While oxide MBE has been able to control stoichiometry of  $\text{PbTiO}_3$  and  $\text{BiFeO}_3$ [109], [110], the same growth approach for many of the titanates cannot be used since they do not have an adsorption-controlled growth.

MBE has many advantages in the growth of oxides. The success of producing sharp interfaces with sub-monolayer control lends itself to a layer-by-layer growth approach. BTO can be considered a superlattice of BaO and  $\text{TiO}_2$  (Figure 11). The sub-monolayer control gives MBE superior stoichiometry control over any other technique. Another advantage MBE has in controlling stoichiometry is the ultra-high vacuum (UHV) environment which greatly reduces defects caused by impurities such as carbon. High purity, independently dosed source material allows for layering of unique oxide structures. The chemical reaction occurs only at the surface and with the atomic species. Also, compared to bulk methods for single crystals (1000-1500 °C), MBE operates at a lower growth temperature (500-900 °C).

From the BaO- $\text{TiO}_2$  phase diagram at these growth temperatures the solubility of BaO in  $\text{BaTiO}_3$  is estimated to be less than 0.1%. Lower solubility means the excess does not incorporate into the lattice. Also, the low volatility of the constituents (BaO and  $\text{TiO}_2$ ) means

that any excess will remain on the surface. With low solubility and volatility, off-stoichiometry growth conditions should lead to other phase formations. However, the substrate provides a template that would encourage BaTiO<sub>3</sub> phase to form. Would the excess then simply stack? Can the excess diffuse through the layers and phase segregate as the phase diagram predicts? Or what kinds of defects will form given the low solubility? With the asymmetry of the titanium and barium vacancy formation, understanding how both barium and titanium excess incorporates will be explored.



**Figure 11.** Superlattice of BaO and TiO<sub>2</sub> layers.

Volatility of atomic or molecular species is required for an adsorption-controlled growth window. The lack of a native growth window (Figure 12) is one reason BaTiO<sub>3</sub> remains one of the most challenging perovskites to grow by MBE. The constituents of barium titanate, namely BaO and TiO<sub>2</sub>, are volatile only under high growth temperatures and extremely low pressures that are not easily accessible [34], [98], [111]-[113] for MBE. Furthermore, oxidation of cation sources cause flux changes, making shutter times difficult to use to consistently and accurately put down single monolayers.

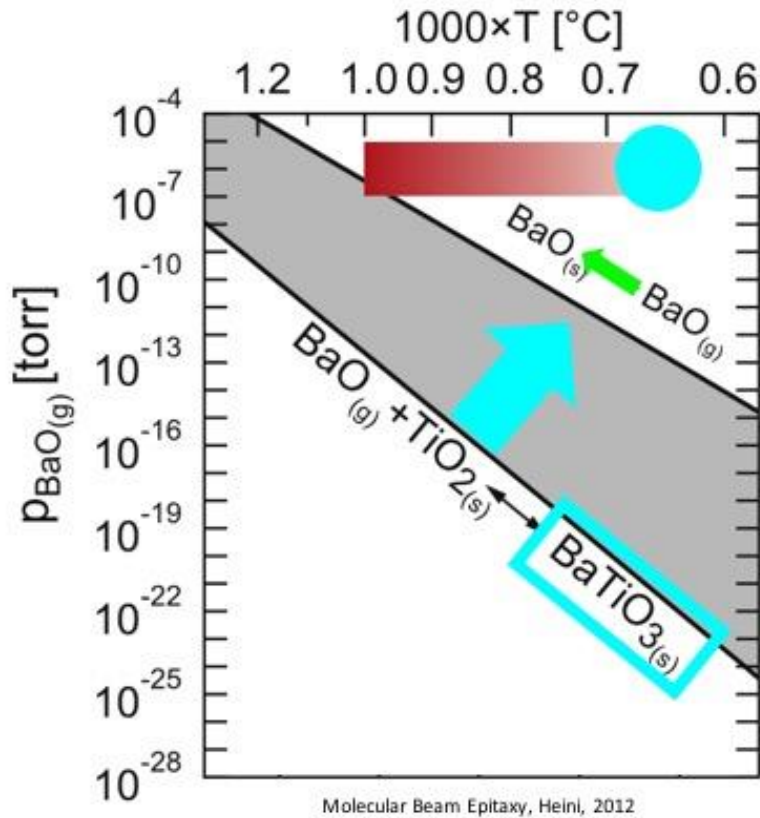


**Figure 12.** BaTiO<sub>3</sub> adsorption-controlled growth window [34].

With both of these challenges, early growth efforts of barium titanate focused on depositing exact amounts of cations using layer-by-layer growth [114]-[116]. Many real time flux monitoring techniques such as atomic absorption spectroscopy (AAS), quartz crystal microbalances (QCM), and reflection high energy electron diffraction (RHEED) were used to measure fluxes in real time [33], [117], [118]. One reason in-situ flux monitoring techniques are necessary is the rapid oxidation of cation sources. Furthermore, the constant opening and closing of shutters creates non-uniform fluxes over the duration of the shutter opening due to flux build-up while the shutter is closed. While AAS & QCM are advantageous in that they detect fluxes before atoms striking the substrate, RHEED is a post-deposition technique. The additional complexity to monitoring RHEED in a superlattice approach like this is, in addition to looking at



surface roughness [119], [120], chemical composition also changes. There is uncertainty in controlling the composition through the use of RHEED oscillations. The uncertainty comes from observing the intensity change near an end of a layer. For example, the intensity increases when depositing BaO, but the maximum intensity is actually more than one barium layer. Observing many oscillations can reduce this uncertainty since complete BaO and TiO<sub>2</sub> layers leads to the peaks and valleys being constant over a long time. Implementing these techniques to control cation deposition exactly is demanding in terms of chamber design especially to accommodate all of the equipment required to monitor the fluxes in real time with a background oxygen pressure on the order of 10<sup>-6</sup> Torr. Furthermore, optimizing the RHEED oscillations requires time-intensive calibrations [121]. The heavy use of shutters for both calibration and growth leads to more equipment failure and increased cost and down time. Even with all of the challenges, high quality BaTiO<sub>3</sub> has been grown by artificially controlling stoichiometry to ~1%. Yet, a self-limiting mechanism that locks-in stoichiometry is still desirable to achieving better accuracy as 1% stoichiometry deviation can still cause dramatic effects [98], [122].

In order to achieve an adsorption-controlled growth window for titanates including BaTiO<sub>3</sub>, a metal-organic titanium source, titanium tetra-isopropoxide (TTIP), was used to develop hybrid molecular beam epitaxy (HMBE). With HMBE, the stoichiometry variation is reduced to 0.1% and has nearly eliminated interfacial defects of BTO films grown on GdScO<sub>3</sub> [123]. HMBE has also been used to grow (Ba,Sr)TiO<sub>3</sub> with higher figures of merit highlighting the value of finding an adsorption-controlled growth window [124]. HMBE supplies excess TTIP that reacts only with another metal, in this instance barium, and at higher growth temperatures (~900 °C) any excess TTIP as well as the byproducts desorb off the surface, thus achieving desorption-limited stoichiometry. The high growth temperature and organic byproducts of TTIP are not desirable for the integration of oxides into semiconductors such as

GaAs that decomposes at  $\sim 600$  °C. A growth approach based upon perovskite formation that limits stoichiometry at lower growth temperatures without byproducts was investigated in this work.

It is proposed that lower growth temperatures under excess cations could be a self-limiting growth condition to control stoichiometry. Barium-rich and titanium-rich growth conditions were investigated. An understanding of RHEED oscillations that indicate barium-rich or titanium-rich growth condition was developed. The stoichiometry and structure of the BTO films were measured.

### 1.3 Impact of BTO Stoichiometry on Ferroelectricity

The ferroelectric properties of BTO can be modified through strain [80], [82], [83] and changes in stoichiometry. Epitaxial growth of BTO on substrates with smaller in-plane lattice constants increases the out-of-plane lattice constant via compressive strain. Oxygen vacancies lead to conductive BTO with no measurable polarization [73], [86], [125]. On the interesting side, it is theoretically predicted that these cation defects can actually induce magnetic responses and may create BTO to become a multiferroic [87], [126], [127].

Ferroelectric properties were measured to assess how off-stoichiometric growth conditions impacted these properties. If extra phases are included, the polarization should decrease since BaO, TiO<sub>2</sub>, Ba<sub>2</sub>TiO<sub>4</sub> and BaTi<sub>2</sub>O<sub>5</sub> all have lower remnant polarization values than BTO. The impact on ferroelectricity is less clear if defects form. For STO, off-stoichiometric growth increased the out-of-plane lattice parameter. Increasing the out-of-plane lattice constant through strain leads to larger remnant polarization. However, the stoichiometry is being changed, which would decrease the polarization. Measuring the ferroelectric properties gave information about how the excess cations during growth impacted the BTO films.

## Chapter 2: Oxide Molecular Beam Epitaxy

A Riber MBE32 (Riber, Bezons, France) for oxide growth was added to the transfer line at the University of Arkansas for the growth of dissimilar materials. The transfer line (Figure 13) already contained two other Riber MBE32s that were used for the growth of semiconductors. MBE1 was focused on the growth of high mobility III-V heterostructures and MBE2 grew many different materials, including GaAsBi, phosphides, manganese, and tellurides. The connection of an oxide MBE to a transfer line opened up the possibility of growing ferroelectrics on semiconductors.



**Figure 13.** MBEs connected via transfer line.

MBE was originally designed to grow semiconductor materials such as gallium arsenide. As such, commercially produced MBEs were constructed out of materials that were compatible with materials such as gallium, aluminum, indium, and arsenic, but did not take into account how oxygen would impact the material of components. Furthermore, design of the chambers included cells and instruments necessary to grow these materials, but did not consider how to measure

fluxes of elements such as titanium. While the ultra-high vacuum and extreme differences in temperatures between components within a chamber are challenging enough, oxygen brings additional requirements to material construction and chamber design.

MBE consists of an ultra-high vacuum (UHV) chamber with Knudsen cells for independent dosing of atomic species. The base pressure of the machine was  $<10^{-9}$  Torr, which was the foundation of growing high purity material. UHV was achieved through the use of several different types of pumps with the workhorse being an ion pump. Liquid nitrogen was flowed through a cryopanel to trap atoms acting as another pump during growth. The cryopanel also surrounded the cells and ensured temperature isolation between cells. The growth was controlled through computer controlled shutters and temperature controllers. The atoms were deposited onto a heated crystalline substrate. Growth was monitored through the use of Reflection High Energy Electron Diffraction (RHEED). The construction and design of MBE components will be discussed in relation to the ability to grow oxides, especially titanates.

## 2.1 Molecular Beam Epitaxy

A Riber MBE32 was heavily modified for the growth of barium titanate. The Riber MBE32 was originally designed for the growth of III-V semiconductors such as gallium arsenide; however, many of the design elements such as material choice for filaments and ports for monitoring fluxes in real time were not provided. Providing elemental sources of barium, titanium, and oxygen was the primary objective (Figure 14) and each material provided its own unique challenges. Maintaining the advantages of MBE in allowing the chemistry to happen at the surface necessitates maintaining a mean free path large enough for cations to reach the surface. The mean free path is one requirement, while the other is maintaining a high enough oxygen pressure, so that the cations oxidize at the surface. Introducing oxygen also adds an

additional challenge in maintaining stable fluxes since the source materials can oxidize. Accuracy of the cation deposition is important since barium titanate does not grow in an adsorption-controlled growth regime. Developing a MBE and growth approach to produce high quality ferroelectrics was the first objective of this research. In this chapter, the development of oxide MBE in a Riber MBE32 is discussed.

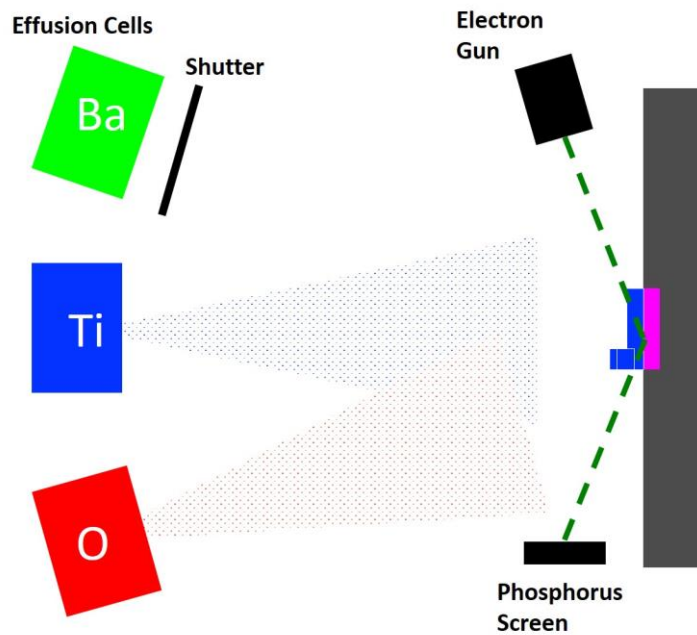


**Figure 14.** Oxide MBE concept.

Additional concerns in terms of material choice for many components inside the MBE are affected by oxygen. Two common materials used in MBE components are tantalum and molybdenum. While under UHV conditions, they can withstand the high temperatures required in many filaments, heat reflectors, or manipulator components, but vaporize when oxygen is introduced [117]. Vaporization of tantalum and molybdenum creates impurities and degrades components more rapidly. The block (Figure 15) used to hold substrates for growth is typically made of molybdenum but, for oxide growth, a nickel-chromium alloy known as Inconel was

used to withstand high temperature and oxygen. Other components affected by oxygen will be discussed later.

Elemental sourcing of barium and titanium was achieved through the use of Knudsen cells. Barium fluxes for growth rates on the order of 1 ML/s can be produced around 600 °C. Barium is not liquid at this temperature and can be held in a traditional pyrolytic boron nitride (PBN) crucible. Titanium requires cell temperatures ranging from 1580-1850 °C (the glowing cell in Figure 15), so a high temperature cell with a crucible made from an alloy capable of handling liquid titanium must be used.

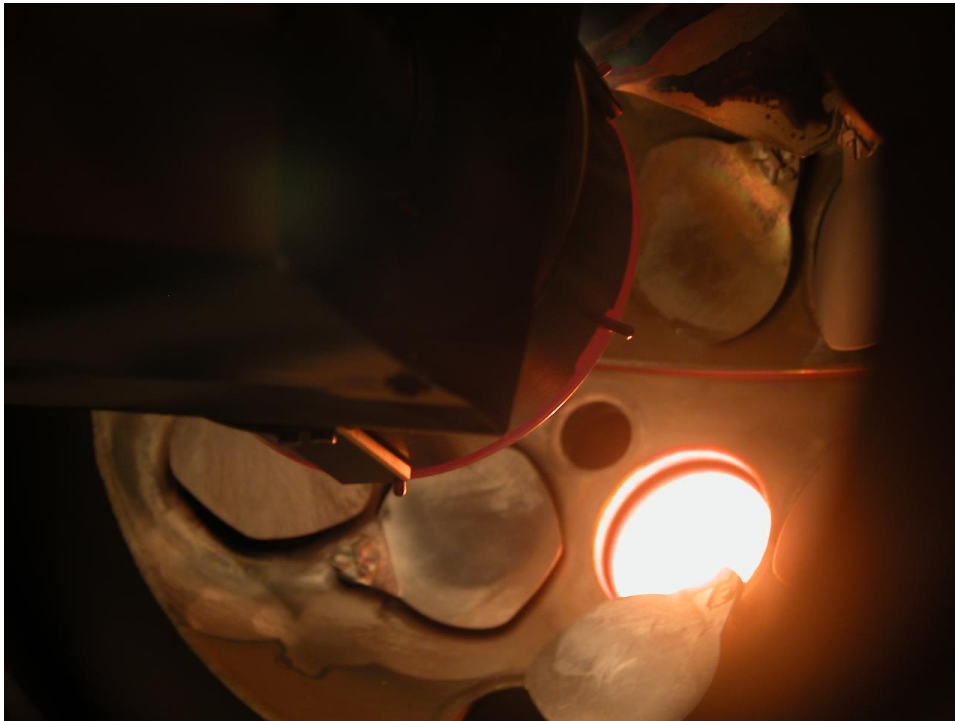


**Figure 15.** Oxide MBE chamber with hot titanium cell.

The focus of the rest of the chapter is discussing how to achieve oxide growth. How to preserve the fundamental advantage of MBE using oxygen is of primary importance. Understanding the impact oxygen has on fluxes and flux monitoring will be discussed. Finally, growing a calibration sample to tune the growth parameters will be highlighted.

### 2.1.1 Oxygen in Ultrahigh Vacuum

The fundamental requirement for molecular beam epitaxy is to have a mean free path that is longer than the distance from cell to manipulator. The mean free path defines the distance an atom can travel before interacting with another atom. The mean free path requirement for MBE ensures that reactions between deposited atoms will happen at the surface and not before. Figure 16 displays the mean free path of metals as a function of oxygen pressure [108]. Twenty centimeters was the distance from the cells to the manipulator. In order for the mean free path to be longer than 20 centimeters, the chamber pressure had to be lower than  $10^{-4}$  Torr.

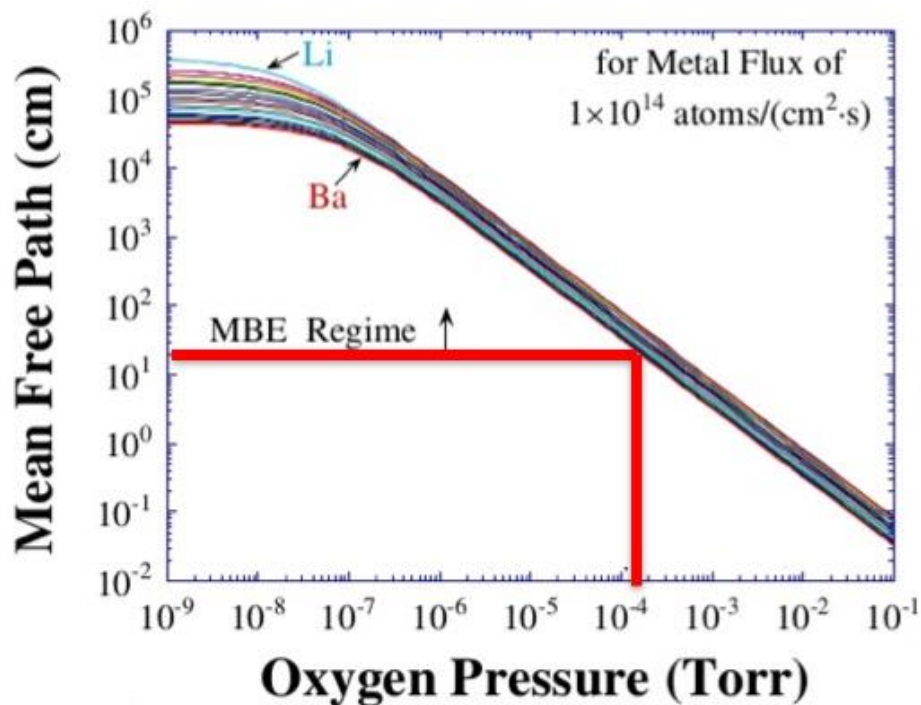


**Figure 16.** Mean free path of cations in oxygen [127].

Since the oxygen is on all of the time during growth, the oxygen pressure defines the mean free path in the MBE chamber. More than just the density of oxygen, the strong electronegativity of atomic oxygen creates an environment where the chemical bonding of cations and oxygen is very likely to happen before the surface. Figure 17 is a schematic representation of the cations (e.g.



Sr or Ti) that are leaving a cell and the number of atoms they have to avoid before reaching the surface. In order to preserve the surface reactions, the mass flow controller was adjusted to flow  $O_2$  at 3.5 sccm to ensure the pressure never rose higher than  $5E-5$  Torr in the chamber.

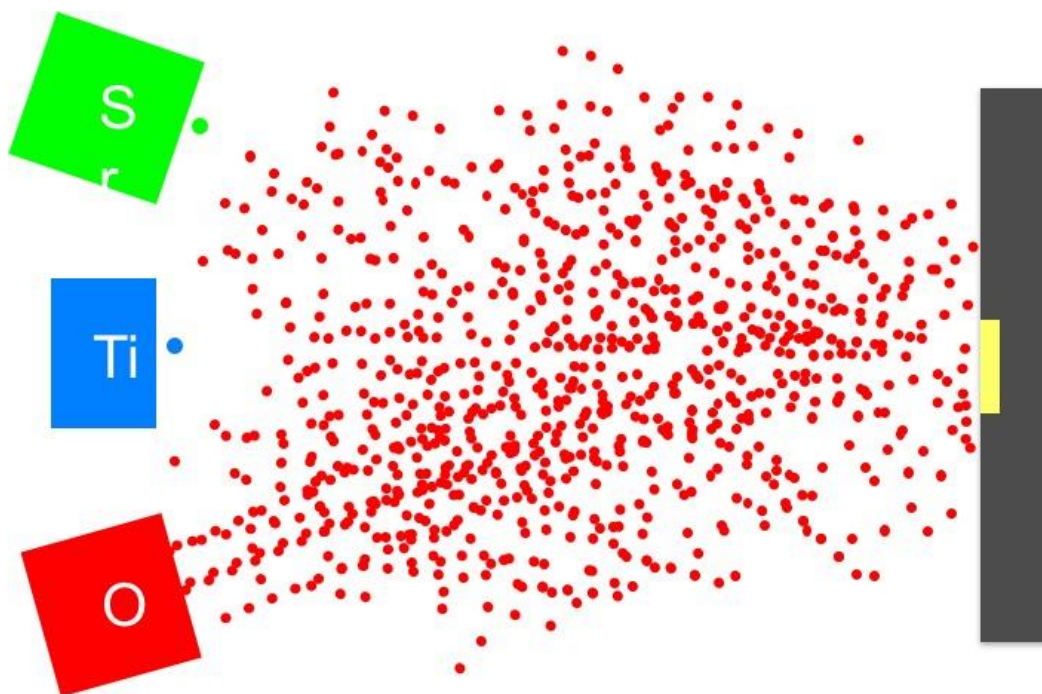


**Figure 17.** Mean free path concept.

An additional requirement for oxide MBE is the ability of oxygen to react with cations and form a metal-oxide. There are two factors for oxidation of cations: pressure and strength of oxidant. Figure 18 shows the pressures for  $O_2$  to oxidize various metals and form a solid. The colored lines are equilibrium lines where all of the reactants form solid. Below this line, solids will not form. At  $600\text{ }^\circ\text{C}$ , barium and strontium requires at least  $5 \times 10^{-6}$  Torr of  $O_2$  in order to form solid BaO and SrO, respectively. However, the mean free path (horizontal red line) represents an upper bound for the oxygen pressure that can be used to ensure the oxidation takes place on the surface of the substrate. Both the mean free path and cation oxidation form a pressure range in which oxide MBE can produce strontium titanate and barium titanate. A 1.5



order of magnitude oxygen pressure window is rather small, making it difficult to ensure both requirements are met.

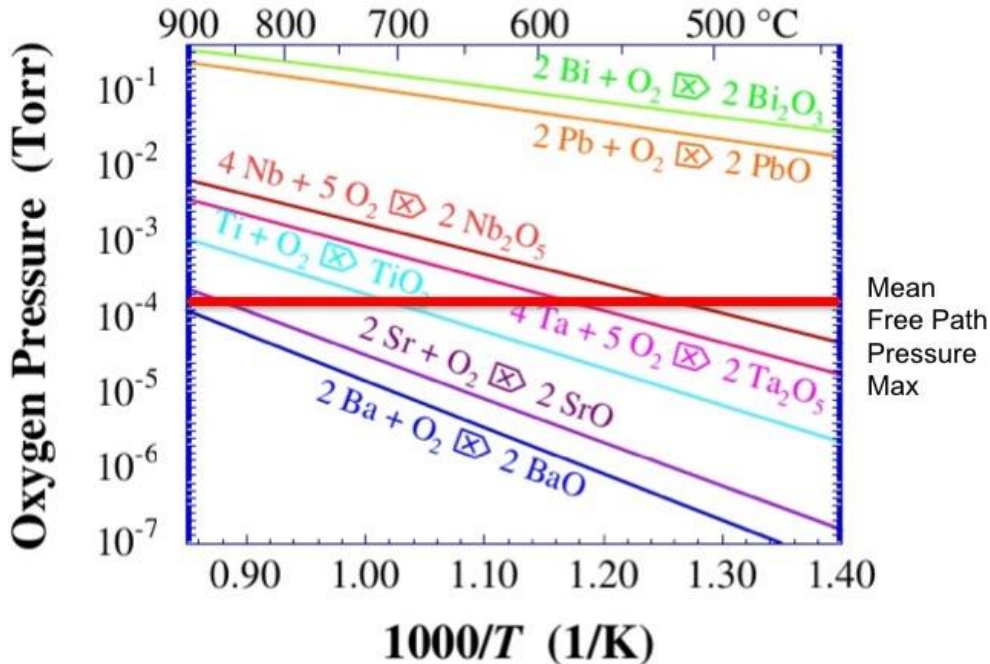


**Figure 18.** Oxygen pressure required to oxidize cations [113].

In order to broaden the pressure range for growth, the second factor affecting oxidation is the potency of the oxidant. In Figure 19, three different oxidants are compared:  $O_2$ ,  $O$  (generated from oxygen plasma) and  $O_3$  (ozone) [114]. The pressure required for each oxidant to oxidize copper is compared in Figure 19. At 600 °C,  $O_2$  requires more than  $10^{-3}$  Torr pressure, while plasma oxygen is one order of magnitude less at  $10^{-4}$  Torr and ozone four orders of magnitude lower at  $10^{-7}$  Torr. Thus, it was attempted to oxidize barium and strontium and discovered both cations oxidized at a pressure of  $5 \times 10^{-7}$  Torr at 600 °C.

While ozone is by far the most reactive oxygen source, there are safety risks involved in using it over the other two oxidants. Ozone will condensate on the cryopanel when LN2 flows through it during growth and will violently desorb upon warming, causing an explosion inside

the chamber [114], [117], [128], [129]. Ozone generation also has risk. However, temperature isolation was a strong requirement for the Ribier MBE32 since the high temperature titanium cell had no water cooling jackets to reduce its operating temperature in the range of 1550-1850 °C. To avoid the extra hazards of using ozone and the strong need for temperature isolation of the titanium cell, oxygen plasma was chosen to be the oxidant.

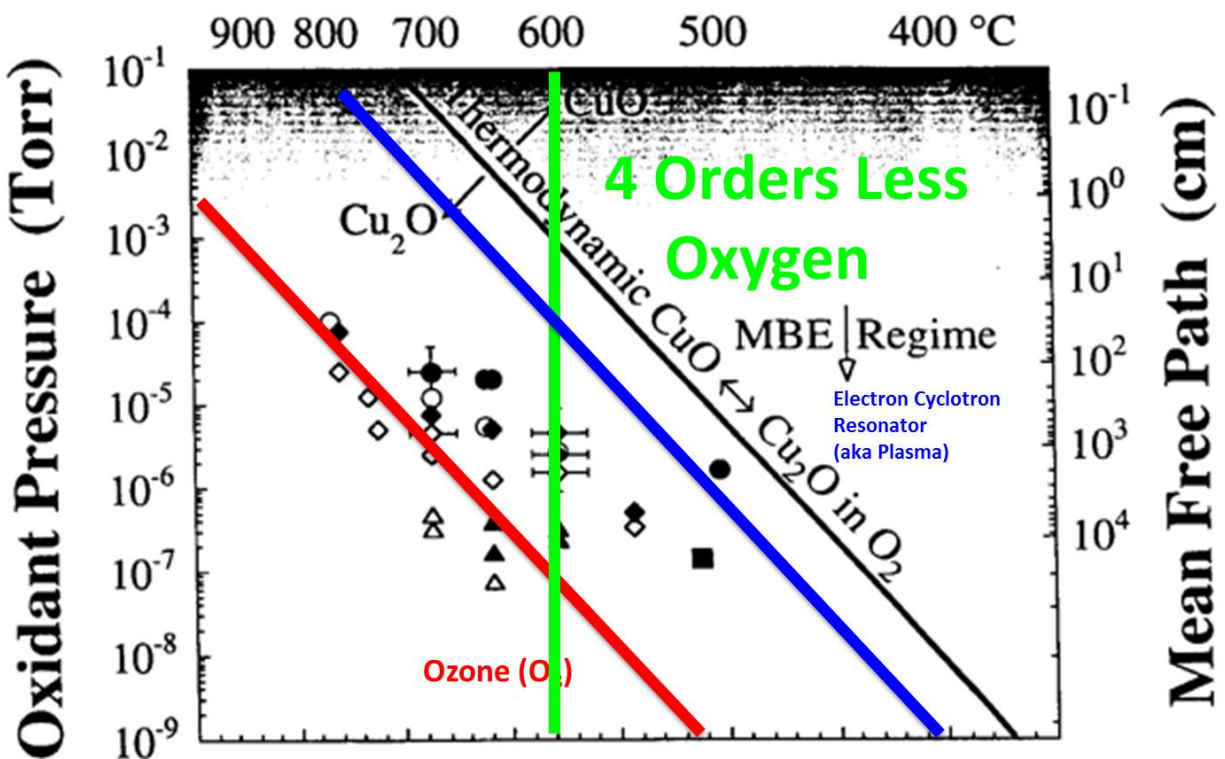


**Figure 19.** Comparison of oxygen source potency [113].

Optimizing the oxygen pressure in the chamber while using a plasma is important to optimize growth. Plasma generates atomic oxygen, which is more potent than O<sub>2</sub>. For MBE, the lower the pressure the better to ensure that the chemistry happens at the surface. In a plasma, the oxygen pressure in the chamber is controlled by a flow controller and 10 psi was used as a constant pressure. However, the amount of oxygen generated in a plasma depends upon flow and power. In order to understand where the maximum atomic oxygen generation occurred for the

Addon oxygen plasma system (Riber, Bezon, France), an optical detector was used to monitor the intensity of light generated (Figure 20) which was proportional to the atomic oxygen generated for various oxygen flow and RF power applied to the coil surrounding the plasma tube. In order to achieve maximum atomic oxygen generation, 3.5 sccm and 400 W was the optimum conditions for stability. At 3.5 sccm and 10 psi, the chamber pressure in the Riber MBE32 was  $2 \times 10^{-5}$  Torr, which was about an order of magnitude lower in pressure than the mean free path requirement of  $10^{-4}$  Torr.

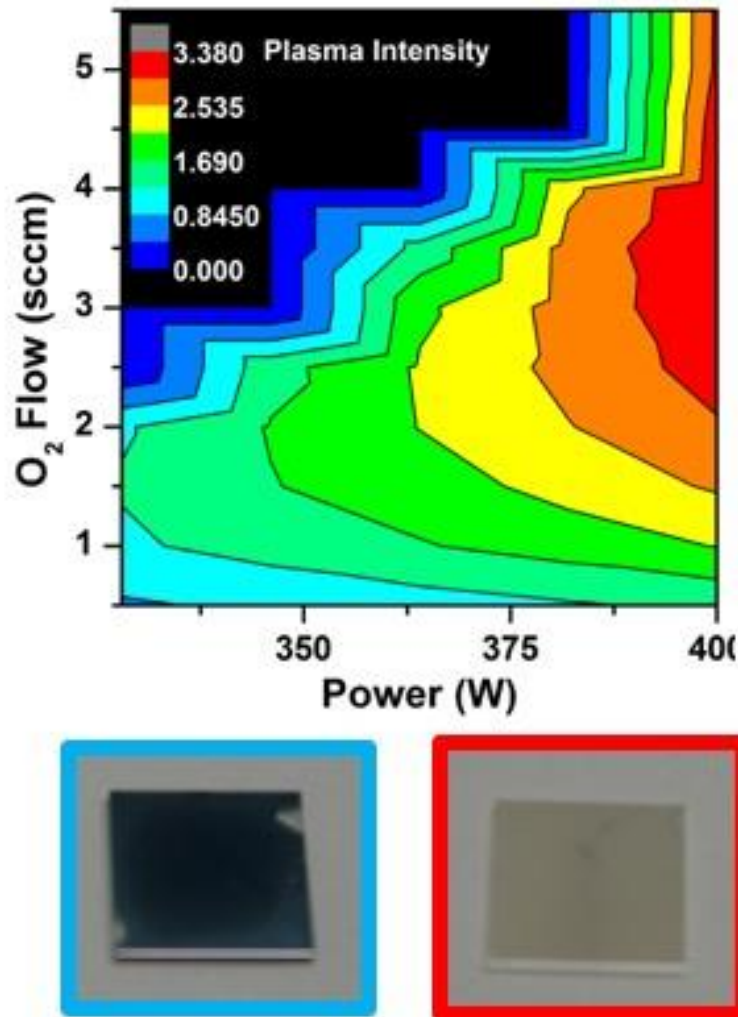


**Figure 20.** Oxygen plasma intensity map. Low plasma intensity (light blue) created oxygen vacancies in BTO. While increasing plasma intensity (red), generated stoichiometric BTO.

The other factor to consider when choosing oxygen flow is oxygen vacancy formation in films. The higher the oxygen pressure, the lower the oxygen vacancy concentration [130], [131]. For comparison, samples were grown using low flow (0.8 sccm and 350 W) and high flow (3.5 sccm and 400 W). The vacancies were so high in the low flow region that the sample was blue in color (Figure 20 – bottom left). The sample also had a low resistance based on a two-point probe measurement with multimeter compared to the transparent, insulating STO at the high flow setting (Figure 20 – bottom right). With the oxygen optimized for growth, attention was turned to how oxygen affects other components, particularly the components that reach high temperatures during growth.

### 2.1.2 Heating and Oxygen

Filaments are the primary components of concern when introducing oxygen to a UHV system. Oxidation of filaments occurs during exposure to oxygen, especially atomic oxygen that is created during oxygen plasma, creating high resistance regions in the filament that over time evaporate and lead to failure. The filaments involved in the Riber MBE32, included substrate heater, cell filaments, RHEED gun, ion gauge, plasma coil, ion pump, and RGA. The hotter the filament and more exposure to oxygen, the more quickly it will to break. Of these filaments, the substrate heater was the most exposed to oxygen, the second hottest filament in the chamber, and the most expensive filament to replace.

In addition to filaments, any components near filaments that are made of tantalum or molybdenum can vaporize. All of the shutters were made of tantalum. The primary shutter of concern was the one in front of the titanium cells that was exposed to greater than 1600 – 1900 °C and could vaporize, if the oxygen pressure was sufficiently high, or deform and increase interaction with the cryopanel and lead to failure.

### 2.1.2.1 Silicon Carbide Heater Upgrade

The standard tantalum filament for semiconductor growth fails in less than six months when exposed to oxygen for growth. The heater failure is problematic for several reasons, including cost, time, and contamination. The PBN shielding, tantalum filament, and tantalum reflective shielding vaporize into the chamber creating the possibility for boron, nitrogen, and tantalum oxide contamination. In addition to contamination from the filament, the frequent venting to replace the tantalum heater also introduces contamination to the chamber, especially since the substrate heater is the component closest to the surface of the grown crystal. In addition to increasing contamination, the subtle changes in the chamber make it difficult to compare samples before and after venting. Finally, while a \$14,000 heater (Figure 21 left) that lasts at least 10-20 years in a MBE chamber designed for semiconductor growth is a cost-effective solution, when the heater only lasts six months, it is cost prohibitive to use.

Riber began developing a silicon carbide heater (Figure 21 right) that is resistant to high temperature and oxygen. The cost was also reduced to \$2,000 and lasted for more than two years. The major disadvantage is the fragile filament and the risk in breaking it during installation. Even after installed, hot spots can develop near the connection that would lead to disintegration and shortened lifetime.



**Figure 21.** Tantalum heater (left) oxidizes while SiC (right) can operate in high heat and oxygen.

The design of the Inconel block had significant impact on evaluating the limitations of the SiC heater. The Inconel blocks had a 10 mm x 10 mm square cut out for the substrate with a 1 mm lip for the substrate to rest on. An 8 mm x 8 mm region of the substrate was exposed directly to the SiC filament as there was no PBN shield with the tantalum design. While testing the temperature range of the heater it was discovered that above 14.5 amps, SiC broke down and SiO<sub>2</sub> films formed on the back of the STO substrates (Figure 22). The ability to remove the sample and examine the composition using XPS revealed a limitation. In order to prevent silicon contamination in the chamber, constant 14.5 amps current was used during growth to ensure no silicon was deposited in the chamber.

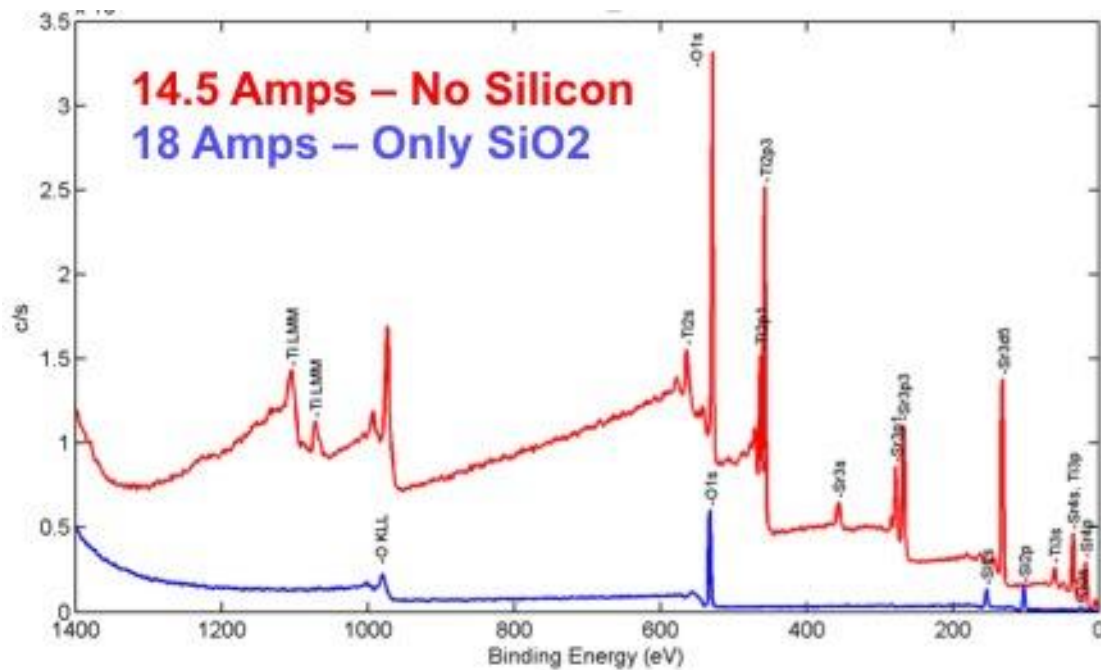


**Figure 22.** XPS results comparing backside of STO sample after operating SiC at 14.5 Amps (Red) and 18 Amps (Blue).

The heater was operated with a constant 14.5 amps, corresponding to heater filament of about 800 °C. The filament heats substrates for growth through radiative heating in the infrared (IR) range wavelength. However, most oxide substrates are transparent to IR; the primary way of

heating of the substrate is indirectly through contact with the Inconel block which is radiatively heated. Thus, heat transfer to the sample is poor and not uniform across the sample. Therefore, the substrate was not able to reach high enough temperatures in order to obtain epitaxial growth of barium titanate. In order to increase the substrate temperature and temperature uniformity across the substrate, an oxide resistant backside coating that could be radiatively heated was developed. In addition, a new method to monitor temperature were developed.

#### 2.1.2.2 Substrate Temperature Monitoring

With a working SiC heater, attention was focused on developing a way to monitor the surface temperature during growth of the most commonly used substrate, strontium titanate. During MBE growth, the surface temperature is the most important, but also the most difficult, to determine accurately. Thermocouples are excellent references for repeating the same growth temperatures, but since their location is far from the surface they do not reflect that temperature. RHEED can be used to monitor reconstruction which happens at certain temperatures [113], [132]-[135], but is not necessarily useful for a wide range of temperatures depending upon the substrate. The use of integrating a kSA BandiT system (k-Space, Dexter, MI) was developed for monitoring the substrate temperature, which could measure both the band edge of STO and blackbody radiation. Integration for real time measurements with the substrate etching procedure is discussed next.

Growth on STO substrates requires etching in order to obtain atomically flat uniformly terminated surfaces [136] as opposed to increasing the surface smoothness through the growth of a buffer layer in semiconductors. Unlike other semiconductor systems, growing a buffer layer is difficult to improve surface quality because no adsorption controlled growth window exists. Instead, selective etching techniques have been developed for oxide substrates to remove SrO



from the surface. For STO, the ‘Arkansas method’ [137], [138] was used to avoid the use of hydrofluoric acid common in other etching procedures [139]. With this procedure, mixed SrO-TiO<sub>2</sub> terminated surfaces were removed (Figure 23 left) and uniformly terminated TiO<sub>2</sub> surfaces with atomic steps measuring 3.905 Å were produced (Figure 23 center).

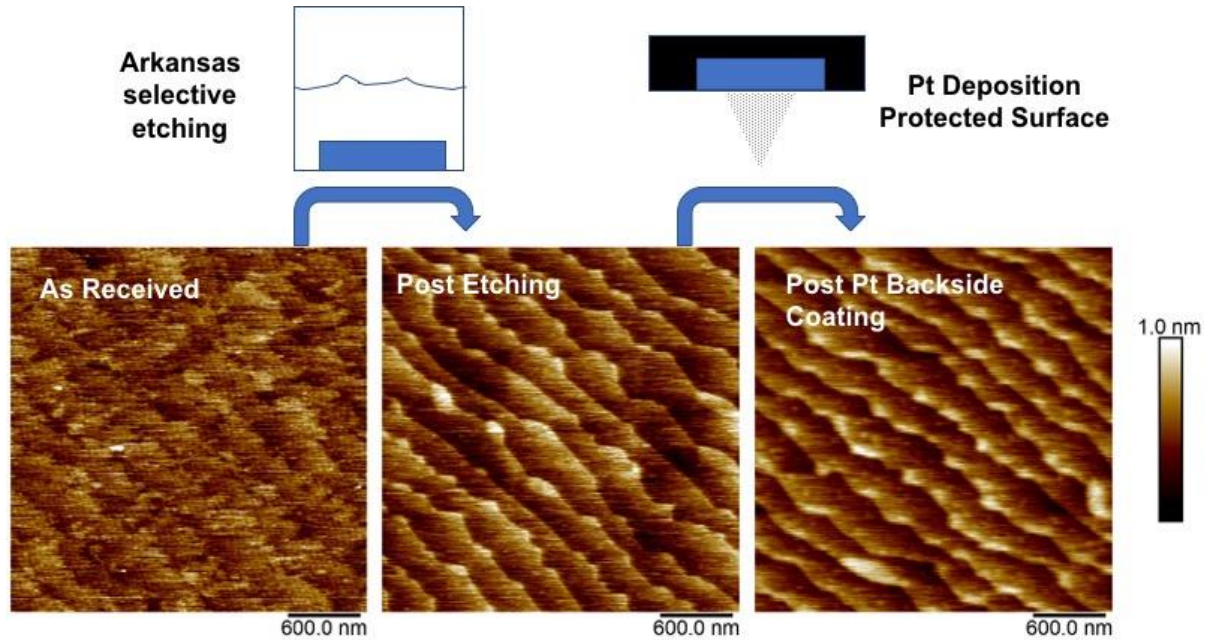


**Figure 23.** STO substrate preparation for growth and optical monitoring.

With a uniformly terminated surface, the band edge temperature was measured. It was found that with the 14.5 A limit on the SiC heater, the hottest the substrate could be heated was ~500 °C (Figure 24). The band edge measurement for the kSA BandiT works off of diffuse reflection on the backside of the single polished STO substrate from a white light source. The diffusely reflected light was absorbed by the whole STO substrate on its way to the detector. The transmitted light received by the spectrometer showed a band edge over the whole thickness. Thus, the band edge represented an average temperature over the thickness of the substrate. The band edge intercept was compared to a calibration file from kSA where two thermocouples had



been placed on the surface of a STO substrate, so that this temperature represented the actual STO surface temperature.

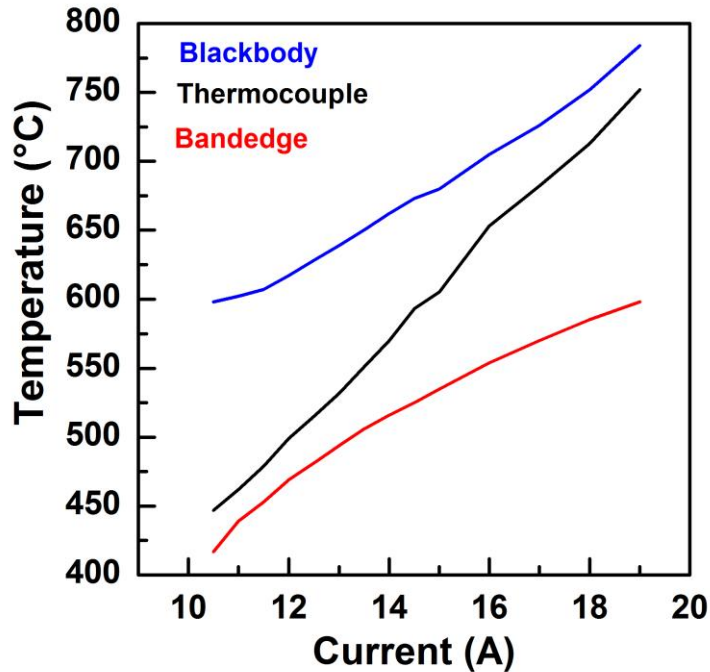


**Figure 24.** Temperature comparisons of blackbody, thermocouple, and bandedge.

It was noticed that this 500 °C bandedge temperature corresponded to a thermocouple temperature of ~575 °C, which was low for producing high quality BTO compared to previous growth studies carried out in this lab. In order to enhance the absorption of the infrared light coming from the heater, it was decided to incorporate a backside coating to enhance the absorption and increase the transfer of heat to the substrate.

In order to integrate a backside coating, a way to coat the backside without destroying the atomically flat surface was developed. Titanium, molybdenum, and platinum were evaluated as potential backside coatings. It was found that both titanium and molybdenum coatings vaporized during high temperature in oxygen and were removed during the course of growth. Platinum was able to last since it's a noble metal that can resist oxidation and doesn't vaporize under growth

conditions. One  $\mu\text{m}$  of Pt was deposited to ensure the skin depth for infrared radiation was met [14], [132], [140], [141]. A custom holder was developed to protect the surface during electron beam deposition and showed that the atomic steps appeared with no detectable contamination to the surface.

After coating, the blackbody radiation of the metal coating was measured and it was found that the backside was over  $650\text{ }^\circ\text{C}$  at 14.5 A. It was unclear how this changed the band edge temperature reading since the coating on the backside modified the transmission spectra thus altering the calibration file that was used. At a constant 14.5 A, strontium titanate and barium titanate were easily grown epitaxially. The backside coating also improved the heating uniformity.

A way was developed to more closely monitor the surface temperature of STO and improve the heat transfer to the sample. The blackbody monitoring of the backside coating allowed monitoring other oxide substrates since no other band edge was calibrated for the kSA BandiT system. With the ability to monitor substrate temperature, developing flux measurements was next considered.

### 2.1.3 Flux Monitoring

Since the growth of strontium titanate and barium titanate can't be grown with an adsorption-controlled growth window, understanding how the fluxes of cations change is important. The stoichiometry of the film is essentially determined by how accurately one can deposit the exact number of atoms put down. Understanding flux stability is important.

Ideally, monitoring fluxes quantitatively in real-time would be a major advantage during growth. There are some challenges in implementing real-time monitoring techniques. Oxygen pressure was on the order of  $\sim 10^{-5}$  Torr in the chamber which dominated the signal of any ion

gauge flux measurements. Furthermore, in a Riber MBE 32, the ion gauge that measures flux cannot be in the growth position simultaneously with the substrate preventing real time monitoring for a second reason. Additionally, an ion gauge can only monitor the flux of barium and strontium cations since the cross-section of titanium is too small and cannot be read. Other techniques have been developed for real-time monitoring of cation fluxes

Quartz crystal microbalances (QCM) and AAS are potential techniques to measure cation real-time fluxes. QCM is useful for detecting titanium, and ideally it is as close to the growth substrate position as possible to reduce the error in sensitivity. Implementing a titanium flux measurement was tried, but failed to find a suitable design that matched a Riber MBE32 system. AAS is possible for barium and strontium, but difficult for titanium with its small cross-section of interaction. Also, a commercial system was not known for purchase at the time.

However, RHEED oscillations have been studied and can be used to determine stoichiometric growth conditions [118], [121]. Even without real-time monitoring techniques, modifying cell temperatures and shutter times would allow for finding stoichiometric growth condition. There are some disadvantages such as longer calibration times, which means use of more growth material and more frequent venting. Also, using material and exposing it to oxygen changes the fluxes. While a calibration sample can be used to find stoichiometric growth conditions, the fluxes are stable only for a few hours.

#### 2.1.3.1 Flux Monitoring

While the ion gauge could not be used to monitor real time fluxes, understanding the starting barium or strontium flux before oxygen was introduced to the chamber could give a clue as to how to adjust the cell temperatures and times during calibration. The cell temperature was raised to 20 °C above the previous growth temperature of the cell to outgas the cell. The shutter

was then opened and closed for 30s intervals, mimicking shuttered growth. The average flux was then calculated from the saturated values during these shutter intervals. The flux was examined before every sample grown as shown in Figure 25.

Barium fluxes changed for every growth even under the same growth conditions. One reason fluxes changed was due to consumption of source material. Oxidation of the source material impacted the stability of the flux. In addition to oxidation, transients and a decrease in the flux after shutter opening were also observed, which complicated being exact in the deposition. It was found that lengthening the shutter time gave less error since the flux was stable after 10 seconds. As long as the shutter time was longer than this, the effect was minimized.

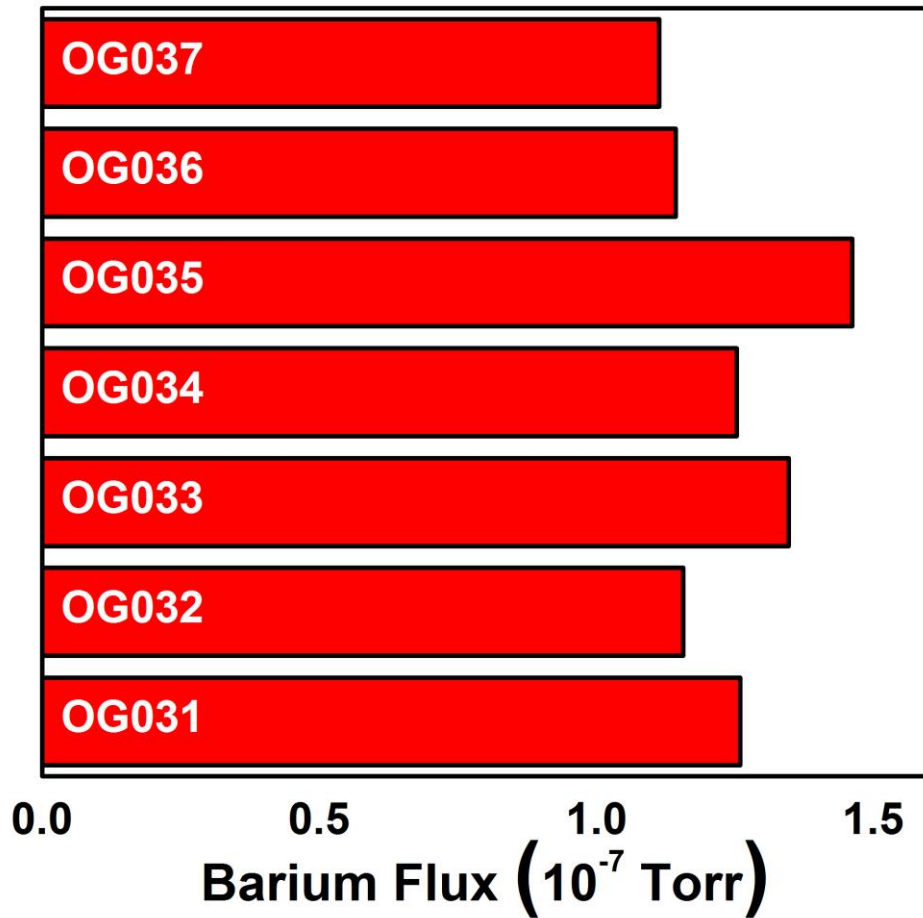


**Figure 25.** Barium flux changes from sequential growths.

### 2.1.3.2 Shuttered RHEED

With the barium or strontium flux determined, the cation cell temperatures were fine tuned to achieve stable RHEED oscillations. The RHEED oscillations came from material deposited on the surface from opening and closing the strontium and titanium shutters in an alternating pattern. A single oscillation resulted from BaO being deposited and increasing the RHEED intensity followed by a decrease from a TiO<sub>2</sub> layer forming on the surface. The intensity of these oscillations was from changes in both roughness and composition. At the end of a BaO layer (Figure 26 B), the intensity was higher since BaO has an atomic number of 64 while TiO<sub>2</sub> has an atomic number of 38 [61]. When complete layers of both BaO and TiO<sub>2</sub> were deposited, the same oscillation repeated. Deviation from this resulted in different patterns of the RHEED envelope [118].

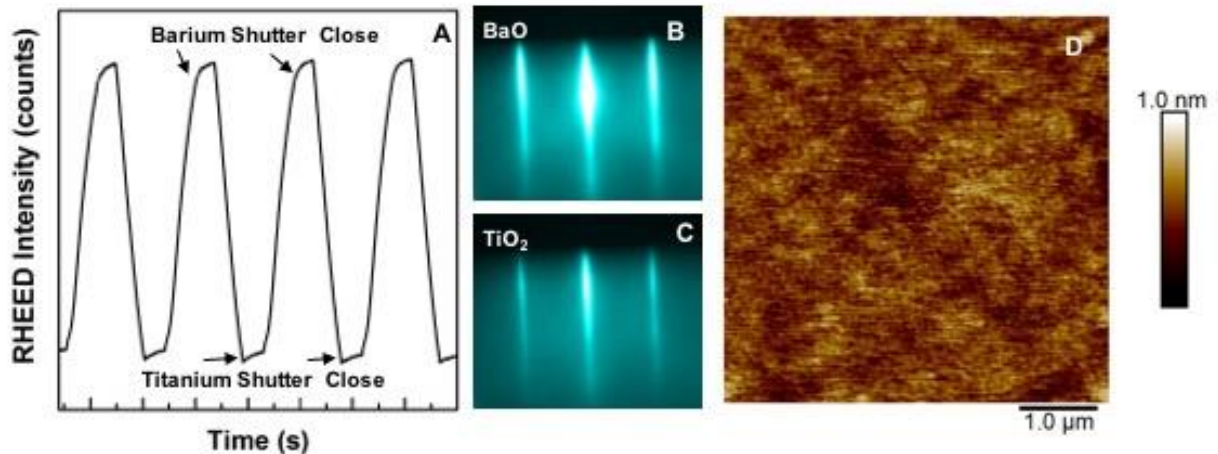


**Figure 26.** (A) Shuttered RHEED oscillations with (B) high intensity of BaO layer and (C) low intensity of TiO<sub>2</sub> layer, results in (D) smooth surface.

In order to obtain stable oscillations, a calibration sample was grown to determine the times the cell shutters needed to be open. Homoepitaxial growth of strontium titanate was employed [121], [132] for its simplicity. Once stable oscillations of SrO and TiO<sub>2</sub> were

achieved, the shutter time and cell temperatures for titanium were used to calibrate growth parameters for barium titanate.

## 2.2 Calibration

The titanium source was calibrated using a series of homoepitaxial strontium titanate growths. Constant cell temperatures were used and adjusted a shutter time after different growths (Table 2). It was discovered that the STO RHEED oscillations were stable over a long period of time for OG014. There was a shift in the XRD peak toward the substrate with the change in shutter times which will be reported in Chapter 3, Section 1. Near complete overlap of film XRD peak with substrate XRD peak showed near perfect stoichiometry of STO.

**Table 2.** SrTiO<sub>3</sub> calibration sample growth parameters

<b>Sample</b>	<b>T<sub>Sr</sub> (°C)</b> (Strontium Cell Temperature)	<b>t<sub>Sr</sub> (s)</b> (Strontium Shutter Time)	<b>T<sub>Ti</sub> (°C)</b> (Titanium Cell Temperature)	<b>t<sub>Ti</sub> (s)</b> (Titanium Shutter Time)	<b>t<sub>Ti</sub>/t<sub>Sr</sub></b> (Titanium-to-Strontium Shutter Time Ratio)
<b>OG010</b>	522	23.5	1720	30	1.277
<b>OG011</b>	522	24.5	1720	30	1.224
<b>OG012</b>	522	24.5	1720	28	1.143
<b>OG013</b>	522	23.5	1720	25	1.064
<b>OG014</b>	522	23.5	1720	26	1.106

During calibration and monitoring the temperature with BandiT, a dramatic temperature oscillation correlated with the RHEED oscillations (Figure 27). The blackbody temperature of the backside coating increased ~10 °C when the titanium cell was opened. Considering the 1720 °C temperature of the titanium cell, an increase in surface temperature of the STO substrate was expected.

With the titanium cell temperature calibrated using STO, the growth of barium titanate was next studied.

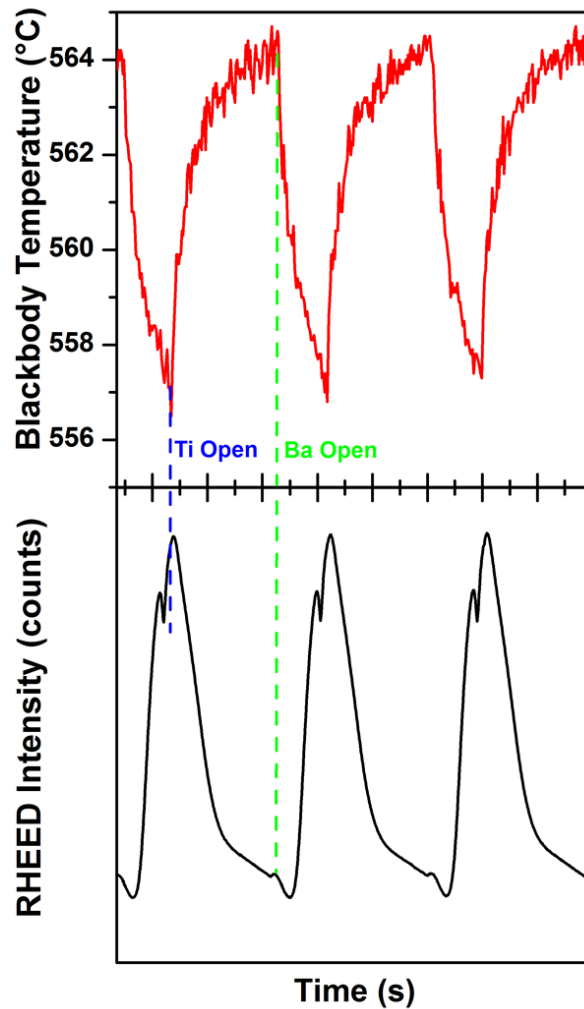


**Figure 27.** Temperature oscillations correlated to RHEED oscillations.

### 2.3 Barium Titanate

RHEED oscillations of barium titanate are the only in situ feedback available to give an indication of the cation fluxes. Identifying key features of oscillations early in growth allow for determination of barium-rich (Figure 28) and titanium-rich (Figure 29) growth conditions. In shuttered RHEED, the key features arise at three different points during the deposition of a layer – shutter opening, shutter closing, and during dwell time.

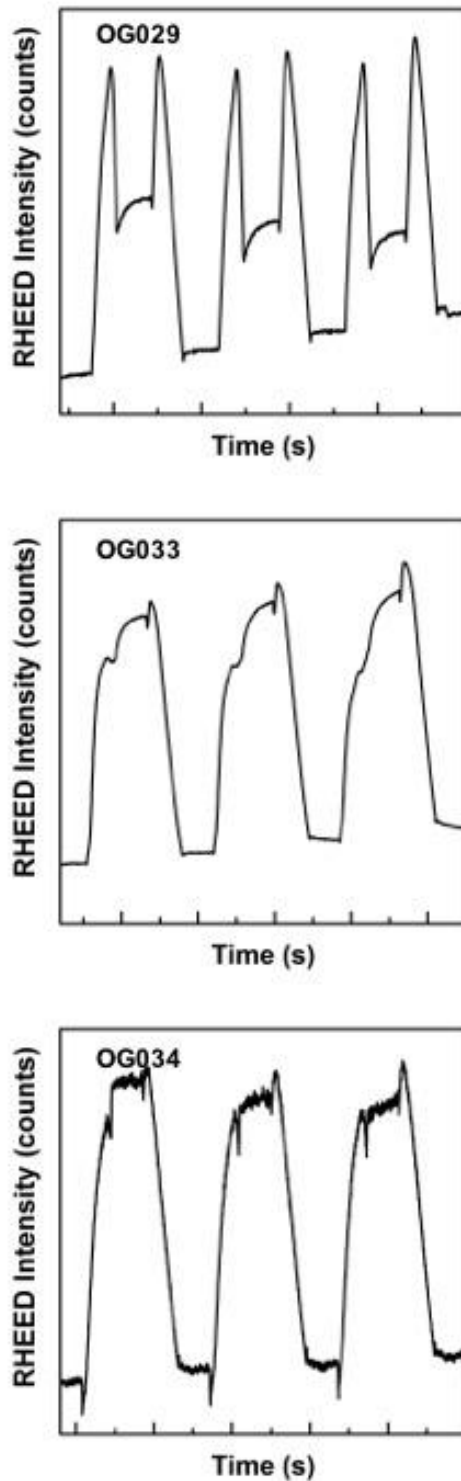


**Figure 28.** Barium rich oscillations for (top) OG029 (middle) OG033 and (bottom) OG034.

Barium-rich oscillations were primarily characterized by peaks at the close of the barium shutter and the opening of the titanium shutter as shown in Figure 28. RHEED oscillations of



ternary materials have at least two mechanisms for intensity variation: roughness and composition. While traditional RHEED oscillations in binary semiconductor systems such as gallium arsenide are related purely to roughness, the change from BaO to TiO<sub>2</sub> surfaces also changes intensity and had to be considered when identifying features and understanding their meaning. When the barium shutter opened, the intensity increased even though there was a slight bump. The peak at the end of the barium opening indicated that more than enough barium had been deposited and the intensity started decreasing due to roughness. During the dwell time, a rise in intensity occurred indicating time for barium atoms to rearrange on the surface, reducing some roughness through island formation. When the titanium shutter opened an increase in intensity occurred, forming a peak before roughness and lower electron reflectivity of the titanium dioxide layer took over. The slant at the end of the titanium indicated no excess has been deposited to complete the layer. During the dwell time after the titanium closed, the intensity remained flat. In summary (Table 3), for barium-rich oscillations, the first half of the oscillation (Ba RHEED) was characterized slant/peak/rise and the second half of the oscillation (Ti RHEED) was peak/slant/flat.

Titanium-rich oscillations were characterized by two curved portions at the opening of the barium shutter and the close of the titanium shutter. When the barium shutter was opened, the intensity remained flat for a few seconds before increasing (hook). At the close of the barium shutter, there was no peak as no excess was deposited on that layer. During the dwell time the intensity remained flat. When the titanium shutter opened there was no peak, instead the intensity started dropping. Toward the end of the titanium oscillation, the slope changed from a slant to a curve. The dwell time after the titanium shutter was flat. In summary (Table 3), the titanium-rich RHEED oscillation was characterized in the first half hook/no peak/flat and in the second half no peak/curve/flat.

**Table 3.** BaTiO<sub>3</sub> samples grown to identify barium-rich and titanium-rich growth conditions.

<b>Sample</b>	<b>Ba Flux (Torr)</b>	<b>t<sub>Ba</sub> (s)</b>	<b>t<sub>Ti</sub> (s)</b>	<b>t<sub>Ti</sub>/t<sub>Ba</sub></b>	<b>Ba RHEED Open/End/Dwell</b>	<b>Ti RHEED Open/End/Dwell</b>	<b>Ti/Ba</b>
<b>OG029</b>	N/A	14.2	17.8	1.25	Slant/Peak/Rise	Peak/Slant/Flat	0.78
<b>OG031</b>	1.26e-7	20.0	25.0	1.25	Curve/Slant/Flat	Peak/Slant/Rise	1.07
<b>OG032</b>	1.16e-7	19.0	25.0	1.32	Curve/Slant/Flat	Down/Curve/Flat	1.23
<b>OG033</b>	1.35e-7	19.2	23.5	1.22	Slant/Peak/Rise	Peak/Slant/Flat	0.68
<b>OG034</b>	1.25e-7	18.7	23.5	1.26	Slant/Peak/Rise	Peak/Slant/Flat	0.65
<b>OG035</b>	1.46e-7	18.0	25.0	1.39	Curve/Slant/Flat	Down/Curve/Rise	1.12
<b>OG036</b>	1.14e-7	17.5	25.0	1.43	Curve/Slant/Flat	Down/Curve/Flat	1.11
<b>OG037</b>	1.11e-7	19.2	25.0	1.30	Curve/Peak/Flat	Peak/Curve/Flat	1.04

Understanding the characteristics of the RHEED oscillations, both individually and collectively, indicate the stoichiometry and how the material grows. Looking at how the oscillations change over time from the beginning to the end of the growth indicate stability of fluxes in a non-equilibrium growth condition (e.g. oxidation of metal source material). Seeing the envelope of the oscillations also gives additional information about how excess material accumulates over time.

A range of barium rich and titanium rich growth conditions was achieved through varying the shutter times for a series of eight samples as shown in Table 3. The barium cell temperature was 600 °C, titanium cell temperature 1838 °C, and the substrate was operated at a constant 14.5 A (~650 °C). The oxygen plasma was operated with 3.5 sccm flow of ultrahigh purity O<sub>2</sub> and 400 W power. The growth approach was shuttered RHEED and incorporated a 20 s dwell time after the barium layer and also the titanium layer. The stoichiometry of the films was characterized by x-ray photoelectron spectroscopy and the Ti/Ba ratio was calculated.

Early RHEED oscillations of the barium-rich samples were characterized. Figure 28 displayed a few of the early RHEED oscillations for each barium-rich sample. The primary characteristics of the two peaks at the close of the barium and open of the titanium varied in intensity.

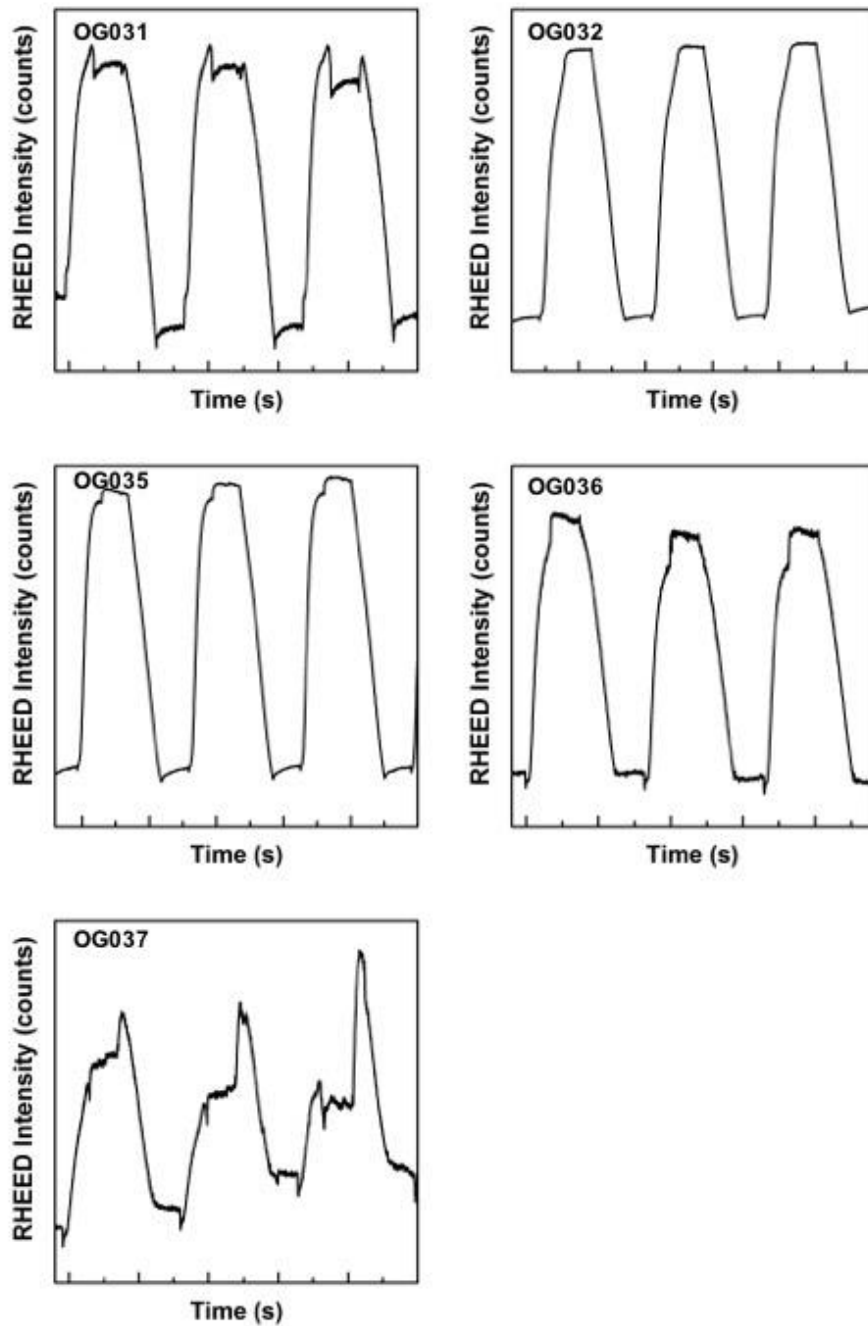


**Figure 29.** Titanium-rich oscillations (TL) OG031 (TR) OG032 (ML) OG035 (MR) OG036 (BL) OG037.

The peak for sample OG033 was very weak but there was still a large rise during the dwell time and a peak when the titanium shutter opened. It's also interesting to note that even though OG029 had the most prominent peaks, it was not the most barium-rich sample. Even with all the variations, a single oscillation from each sample was characterized by slant/peak/rise/peak /slant/flat.

The titanium-rich RHEED oscillations (Figure 29) had identifying characteristics that also varied just as in the barium-rich case. The most common characteristics was a curve at the opening of the barium (hook) and close of the titanium (tail). There was no peak at the close of the barium and the dwell time was typically flat. There also was no peak at the opening of the titanium and most often a curve developed. The curvature of the tail was subtle and developed very gradually and was easy to miss when trying to judge by eye. The dwell time after the titanium was also typically flat.

Sharp jumps in RHEED intensity at the close and open of both shutters for samples OG031, OG035, and OG037 occurred. These were due to light reflecting off the shutter into holes in the RHEED screen. So, though there appeared to be peaks or rises, they were artifacts of the measurement setup.

In addition to early individual RHEED oscillations, the envelope of many oscillations also had identifying characteristics for barium-rich and titanium-rich growth conditions. In Figure 30, an envelope of barium-rich oscillations for a 40 nm thick BTO film showed an arch like behavior with an initial rise in the envelope and then decreased in the envelope as well as the magnitude of the oscillations.

Concerning the titanium-rich envelope (Figure 30), a stark contrast was the more stable form of the oscillations. There was a small arch early on with a subsequent slight downward trend, but the magnitude of oscillations stayed nearly constant. Furthermore, the change in the

individual oscillation was more subtle, merely showing a longer tail at the end of the titanium shutter cycle.

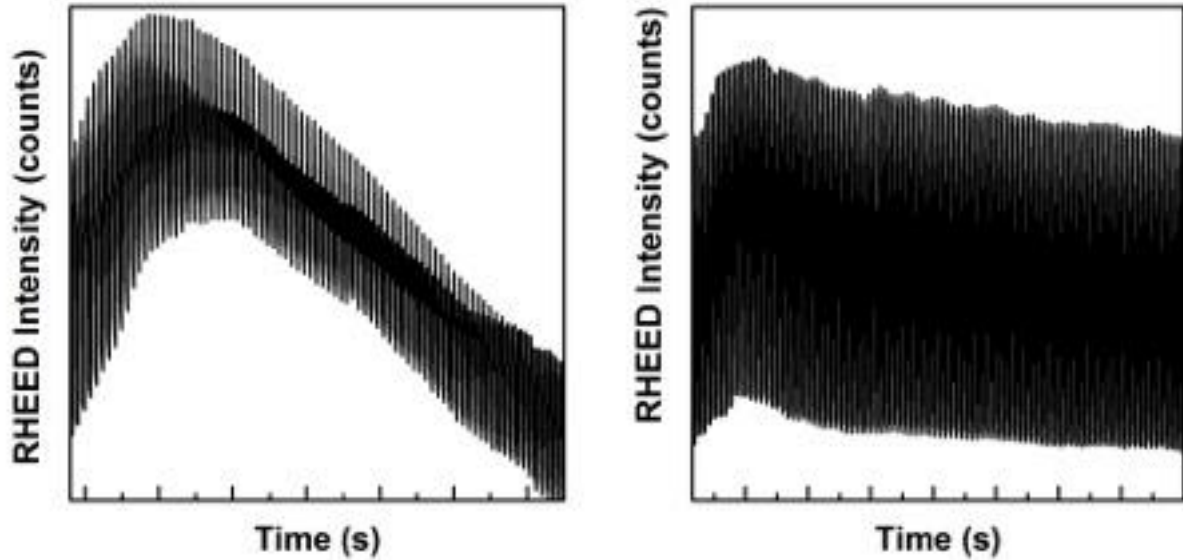


**Figure 30.** Comparing RHEED envelopes of (left) barium rich to (right) titanium rich.

The differences in changes with oscillations over time gave a clue as to how the excess cations incorporated into the film. The ionic radius of titanium is nearly half that of barium, making it easier to fit in as an interstitial or substitute for the barium location. The stability of the oscillations over time indicated that the structure was not being altered greatly and potentially incorporating the excess titanium as defects. However, the size of the barium atom is prohibitive to incorporate excess barium and it accumulated at the surface.

Identifying characteristics of barium titanate RHEED oscillations was completed to properly identify barium-rich and titanium-rich growth conditions. Barium-rich was easily identified by two peaks while the titanium rich condition showed a hook and tail.

### **Chapter 3: Materials Characterization of Barium Titanate Thin Films**

Barium titanate thin films were characterized to determine the stoichiometry, structure and morphology. The stoichiometry was used to verify the barium-rich and titanium-rich growth conditions. The out-of-plane lattice constant was determined as an indirect measurement of stoichiometry and determined the phase of the thin film. The surface morphology was determined to understand how the excess cations affected the surface. The focus of the characterization was to understand how the off-stoichiometric growth conditions impacted the material properties of the barium titanate thin films.

There are three techniques that that give information about how the stoichiometry of the film was affected by the off-stoichiometric growth conditions. X-ray diffraction was used to measure the out-of-plane lattice parameter which is sensitive to substitutional defects that can cause changes in the stoichiometry. XRD has been used to evaluate very sensitive changes in off-stoichiometric growth conditions for strontium titanate [112], [118]. XRD gives an average signal throughout the entire thickness of the film to indicate the uniformity over the whole sample. To complement the average stoichiometric determination from XRD, x-ray photoelectron spectroscopy (XPS) was used to look at the surface chemistry to understand how the excess cations may have bonded or incorporated into the lattice. XPS was limited, however, in that it probes only the top 5 nm of the film and, therefore, did not accurately measure the stoichiometry of the entire 40 nm BTO films. The last technique used was atomic force microscopy (AFM) to look at the surface since different chemistry can result in different morphology.

In this chapter, each analytical technique will be described in terms of the physics of operation as well as fundamental components necessary to operate. Furthermore, the type of data that was collected will be described and how it was analyzed. The raw data and the results from

each of the 40 nm thick barium titanate thin films are explained. A summary of what was learned about how the growth conditions affected the film properties is presented.

### 3.1 Thin Film Structure

The structure of the barium titanate thin films was measured using x-ray diffraction. The out-of-plane lattice parameter could be calculated from the  $2\theta$ - $\omega$  scans to confirm the phase of BTO. Indirectly, the structure might give stoichiometric information since defects such as substitutions or vacancies could affect the lattice parameter.

#### 3.1.1 X-ray diffraction

X-ray diffraction is a scattering technique that looks at the constructive interference patterns from periodically spaced atoms. XRD uses electromagnetic radiation to oscillate the electrons in the atoms and reradiate on the same frequency in all directions (Figure 31). The incident angle,  $\theta$ , for constructive interference of radiation with wavelength,  $\lambda$ , reflecting from lattice planes with spacing,  $d$ , is given by Bragg's law.

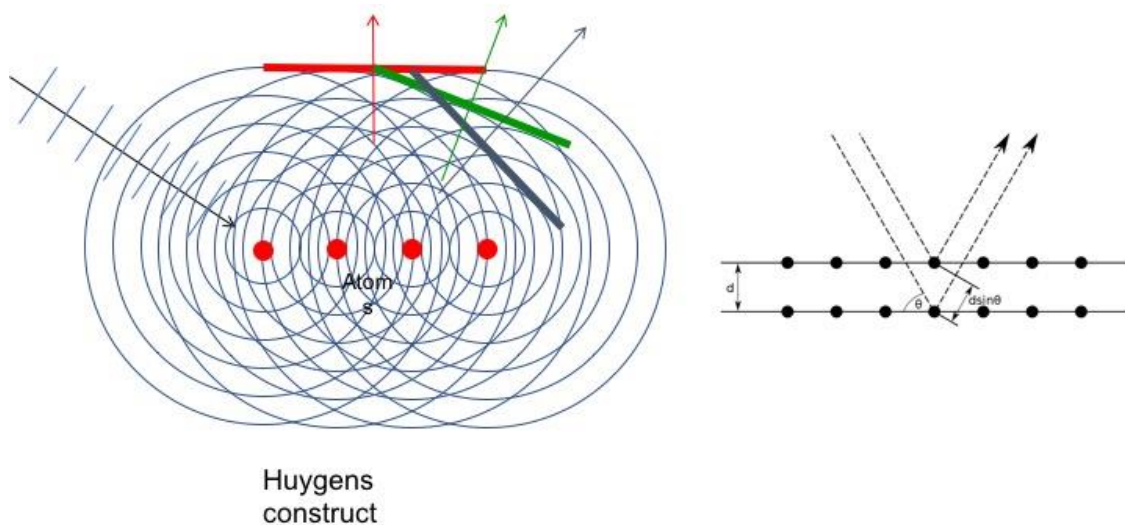


**Figure 31.** X-ray diffraction excites spherical waves (left) and constructive interference between planes occurs at certain angles.

The high-resolution x-ray diffraction measurements were performed using a PANalytical X'Pert MRD diffractometer (PANalytical, Almelo, Netherlands) equipped with a 1.6 kW x-ray tube (vertical line focus) emitting CuK $\alpha$ 1 radiation ( $\lambda = 1.540598 \text{ \AA}$ ), a symmetric  $4 \times \text{Ge}(220)$  monochromator and a Pixel detector.  $2\theta$ - $\omega$  scans were performed to probe the out-of-plane lattice parameter. The  $2\theta$ - $\omega$  curves of the (002) BTO peak were fitted using Gaussian peaks to accurately fit the top half of the peak for peak position. The lattice parameter was then determined using Bragg's law.

$$n\lambda = 2d \sin \theta \quad (\text{Equation 3})$$

To understand the BTO peak broadening (Figure 32) in the different thickness of BTO film, XRD simulations were performed (Figure 32). The FWHM of these simulated XRD peaks could be determined.

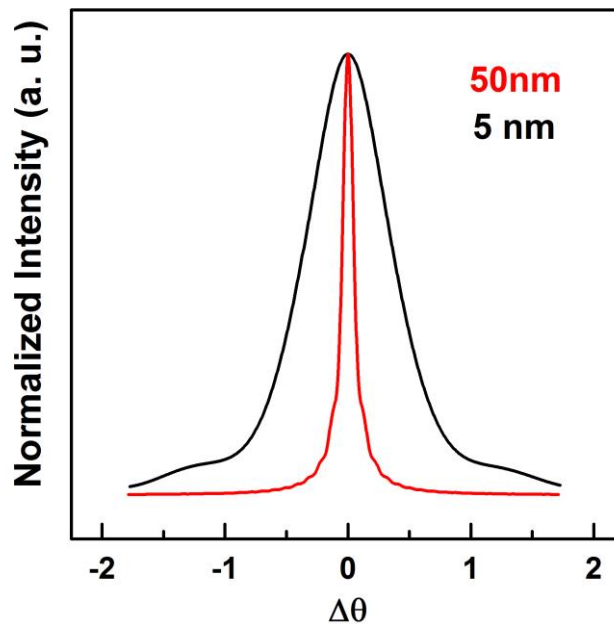


**Figure 32.** XRD simulations comparing the FWHM of 5 and 50 nm thick films. The 5 nm film has a FWHM that is six times larger than the 50 nm FWHM.



The Scherrer equation [3] was used to give an estimate of the broadening (Equation 4).

The change in FWHM based upon the Scherrer equation agrees with the simulations.

$$\epsilon = \frac{\lambda}{b \cos \theta} \quad (\text{Equation 4})$$

where  $\epsilon$  is the crystallite size (thickness in the case of thin films),  $b$  the FWHM,  $\lambda$  the x-ray wavelength, and  $\theta$  the Bragg angle. The ratio of FWHM for 5 and 50 nm was calculated using Equation 4 for each thickness.

For more accuracy, XRD simulations modeling thin films of 5 and 50 nm thicknesses were carried out using a diffuse interface. The full width at half maximum (FWHM) of both 5 and 50 nm film peaks were determined through Gaussian peak fitting (Figure 33) to be  $0.79^\circ$  and  $0.13^\circ$ , respectively. The 5 nm thick film was six times broader than the 50 nm film purely due to thickness. This matched really well experimentally where the 5 nm film was  $\sim 5$  times broader than the 50 nm film.

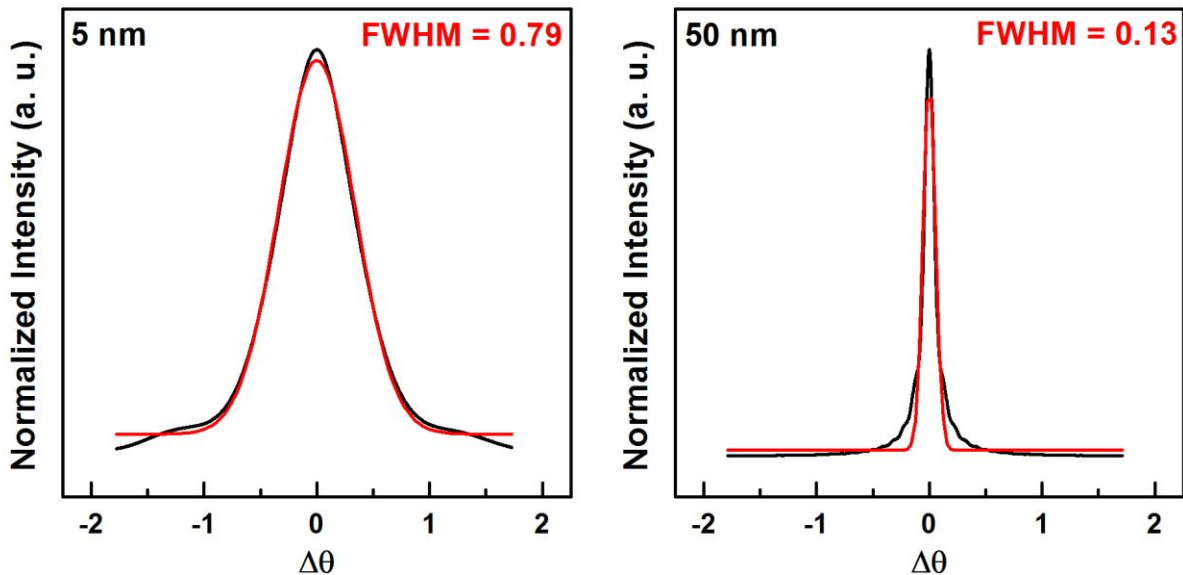


**Figure 33.** Gaussian fits of the simulated 5 nm and 50 nm films to determine the FWHM at each thickness.

### 3.1.2 XRD Results

The results in Figure 34 are for a series of strontium titanate thin films where the only parameter that was varied was the titanium to strontium shutter time ratio. This series of samples was grown in order to calibrate the titanium flux to determine the shutter time for a single layer of titanium. The peak of the STO film for final sample (light blue) nearly overlapped with the peak for the STO substrate (indicated by the dashed vertical line in Figure 34) indicating near ideal stoichiometry. This sample also showed good RHEED oscillations that repeated with consistent peak intensities for a long time.

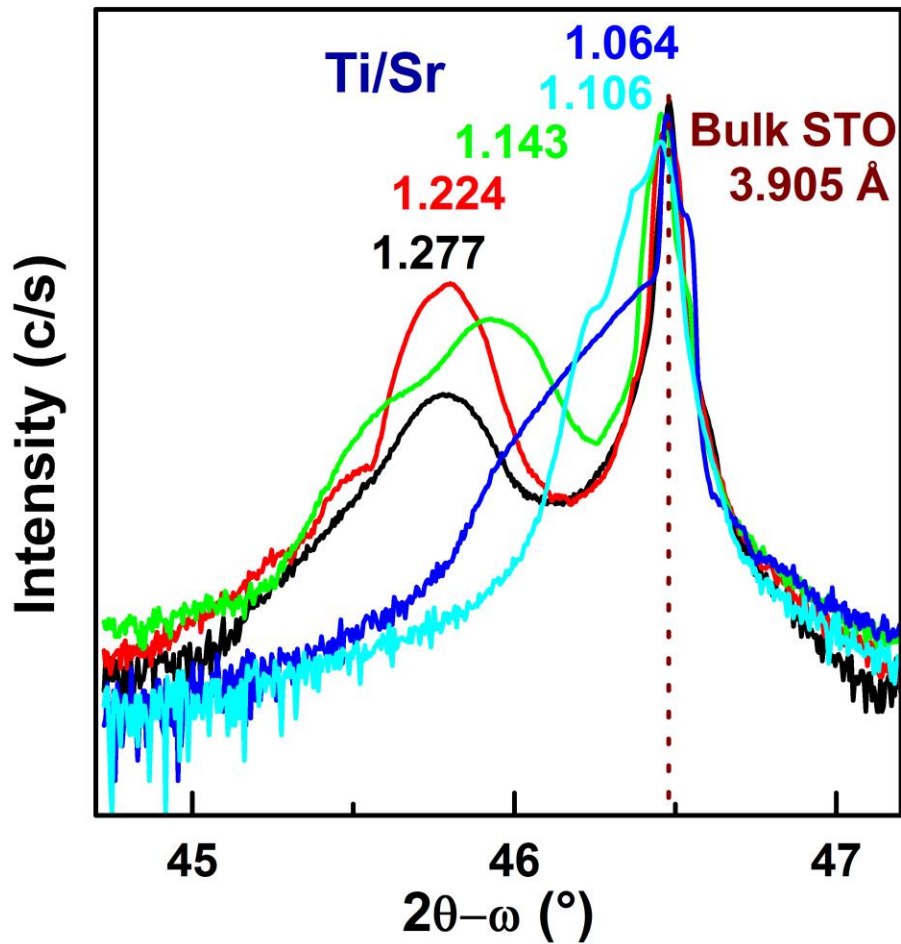


**Figure 34.**  $2\theta$ - $\omega$  scans of strontium titanate thin films grown with various Ti/Sr shutter time ratios.

The peak shifted toward the substrate STO peak as the titanium shutter time was increased. In Figure 35, it can be seen that when the titanium-to-strontium shutter time ratio was reduced, the lattice parameter was reduced to values of bulk, stoichiometric strontium titanate, which is 3.905 Å. Also, the trend had a nearly linear relationship between the lattice parameter and titanium-to-strontium shutter time ratio as shown in Figure 35. This indicated that the titanium and strontium excess atoms incorporated into the lattice, thus changing the composition and the lattice parameter as measured from the XRD scans. The change in larger lattice parameter with excess strontium was expected [118].

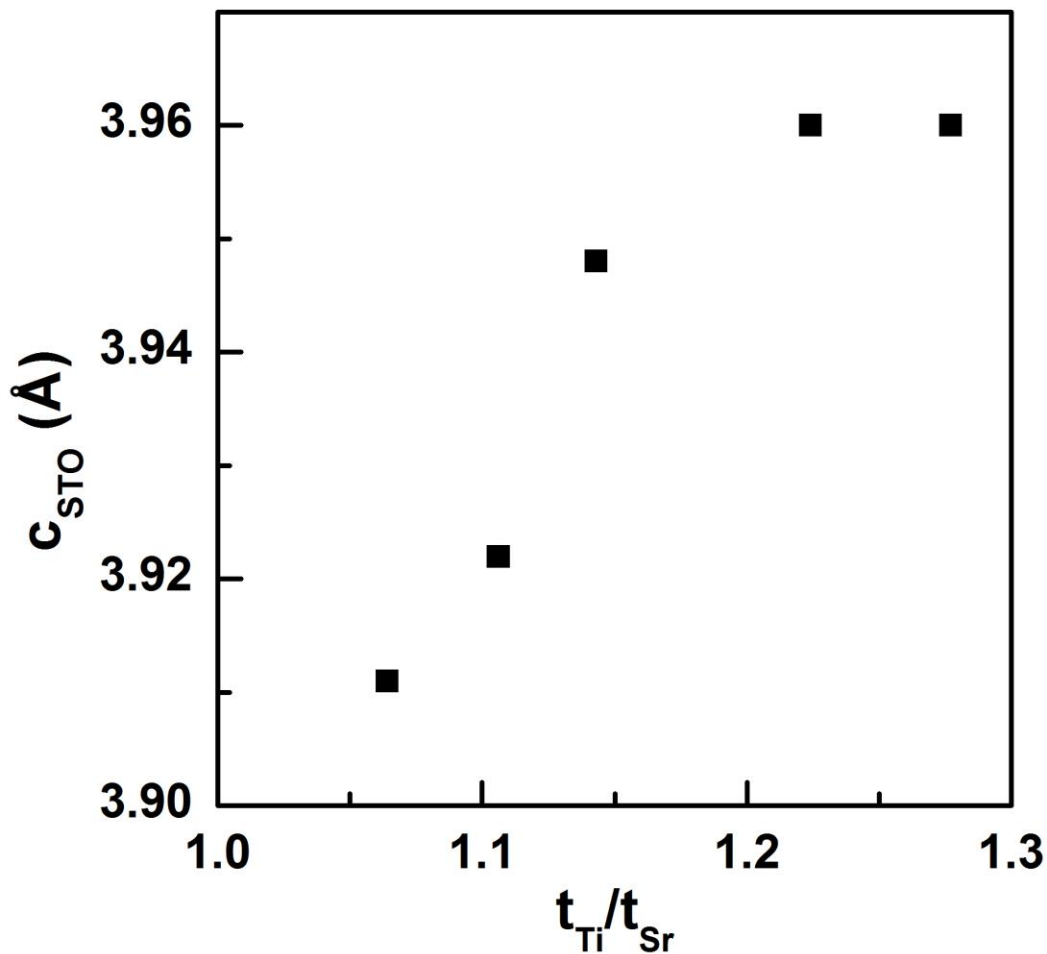


**Figure 35.** SrTiO<sub>3</sub> out-of-plane lattice parameter change with shutter time ratio.

Table 4 summarizes the XRD analysis of the  $2\theta$ - $\omega$  curves for the STO films. The substrate and STO film angles are displayed along with the titanium-to-strontium shutter times and the out-of-plane lattice constant, calculated from Bragg's law for a cubic structure. The STO film peak position varied from 45.784-46.400°, a range of 0.616°, that corresponded to a change in titanium-to-strontium shutter time ratio ranging from 1.064-1.277, a range of 0.213. Figure 35 displays a near linear relationship between the titanium-to-strontium shutter time ratios and the XRD peak position. The linear relationship between shutter times (pseudo composition) and lattice parameters is similar to Vegard's law.

**Table 4.** SrTiO<sub>3</sub> XRD analysis as function of growth conditions.

Sample	$t_{Ti}/t_{Sr}$	Substrate (°)	STO Film (°)	$c_{STO}$ (Å)
OG010	1.277	46.480	45.784	3.960
OG011	1.224	46.470	45.788	3.960
OG012	1.143	46.458	45.934	3.948
OG013	1.064	46.477	46.400	3.910
OG014	1.106	46.450	46.260	3.922

Similar to the STO, the stoichiometry of the BTO films was measured. The titanium to barium shutter times were varied to change from barium-rich to titanium-rich. XRD  $2\theta$ - $\omega$  curves were also taken of these films (Figure 36). A difference between strontium titanate and barium titanate growth is that the BTO growth is heteroepitaxial since no epi-ready barium titanate substrates exists for high quality growth. The lattice mismatch creates compressive strain that makes it difficult to grow. However, the 2.2% mismatch between BTO and STO yields compressive strain that should be completely relaxed at 10 nm. So, the 40 nm films should have

been completely relaxed. Thus, the bulk of the signal coming from XRD  $2\theta$ - $\omega$  curves should represent the relaxed lattice constant of the films. Measuring the relaxed lattice parameter gave better understanding how the excess cations incorporated into the films. Any shift in the relaxed lattice parameter could give an indication that excess cations incorporated as defects that could change the lattice spacing.

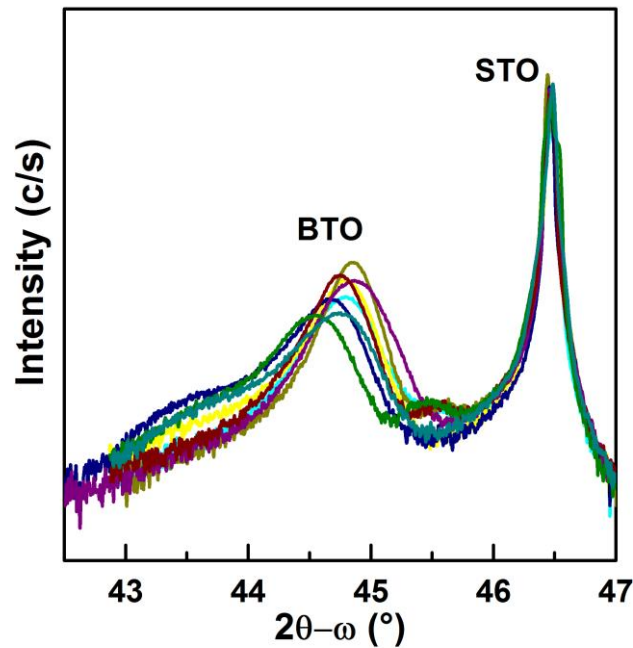


**Figure 36.** XRD  $2\theta$ - $\omega$  curves for all BTO films.

The STO substrate peaks were all aligned to  $46.4^{\circ}$  so that the BTO peak position variation would be accurate. All of the BTO peaks could be fitted using a Gaussian fit for the top of the peak to accurately determine the peak position. A couple of the films had shoulders at higher angles around  $43.5^{\circ}$ , possibly due to a strained layer. A couple of the scans showed a small peak in between BTO and STO around 45.5 degrees. Neither of those peaks were related to other BTO phases such as  $\text{Ba}_2\text{TiO}_4$  and  $\text{BaTi}_2\text{O}_5$ . To verify this, broad range  $2\theta$ - $\omega$  scans were taken to ensure no other primary peaks for those phases existed.

**Table 5.** BaTiO<sub>3</sub> XRD analysis as a function of growth conditions.

Sample	t <sub>Ti</sub> /t <sub>Ba</sub>	Substrate (°)	BTO (°)	c <sub>BTO</sub> (Å)
OG029	1.25	46.487	44.861	4.038
OG031	1.25	46.463	44.790	4.044
OG032	1.32	46.444	44.825	4.041
OG033	1.22	46.460	44.633	4.057
OG034	1.26	46.467	44.849	4.039
OG035	1.39	46.473	44.738	4.048
OG036	1.43	46.464	44.563	4.063
OG037	1.30	46.483	44.745	4.047

When the change in lattice parameter with respect to titanium-to-barium shutter time was examined (Figure 37), the same trend with STO did not appear. From 1.25 to 1.45 the relationship was linear. There was one outlier for the most extreme titanium-to-barium shutter time. This sample was included for completeness, however, complications during growth evidenced by the starting RHEED pattern indicate that it may have been an anomaly.

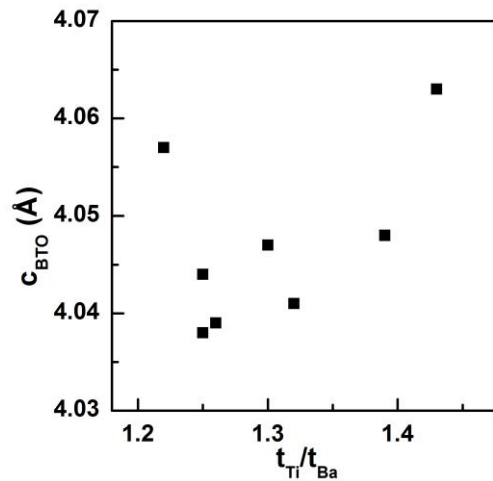


**Figure 37.** Out-of-plane lattice parameter of BTO films as function of shutter time ratio.

In order to investigate why the lattice parameter is less variant than the strontium titanate case, the surface stoichiometry was investigated.

### 3.2 Thin Film Surface Composition

While XRD is useful for determining the crystal structure and phase, it is an indirect measurement of the stoichiometry. In ternary materials such as barium titanate, it is not a direct measurement of the stoichiometry since BaO and TiO<sub>2</sub> do not alloy in a predictable pattern according to the phase diagram. Other techniques are needed to directly measure the stoichiometry.

X-ray photoelectron spectroscopy is a surface sensitive technique suited to directly measure the stoichiometry of the barium titanate thin films. XPS analysis was used to determine the titanium-to-barium ratio based on the titanium to barium shutter time ratios. The cation ratio would determine if the excess barium or titanium was incorporated into the films. If the changes in lattice parameter were indicative of the excess incorporating into the films, different chemical environments would be revealed in XPS spectra.

#### 3.2.1 X-ray Photoelectron Spectroscopy

XPS is based on the photoelectric effect which Albert Einstein received his Nobel Prize for in 1921. The basic concept is electrons are ejected from the sample using x-rays (Figure 38). These core level electrons have a unique signature because the binding energy of the electron to the nucleus of an atom is different for each element, thus different elements will show up at different BE peaks as seen in Figure 39. Furthermore, this binding energy is sensitive to the chemical bonding environment; for example, carbon bonded to carbon will have a different BE than if carbon was bonded to oxygen. The valence electrons change the electron energy levels of

the core level electrons depending upon the bonding (Figure 39). When an x-ray is absorbed by a core level electron, it is ejected from the sample if the energy of the x-ray is greater than the binding energy and work function of the material. The work function is the energy from the Fermi level to the vacuum energy level. XPS is the technique correctly suited for investigating an unknown material under various growth conditions. Furthermore, the systemic change in the barium titanate thin films under the same process is ideally suited for showing systemic changes in the stoichiometry.

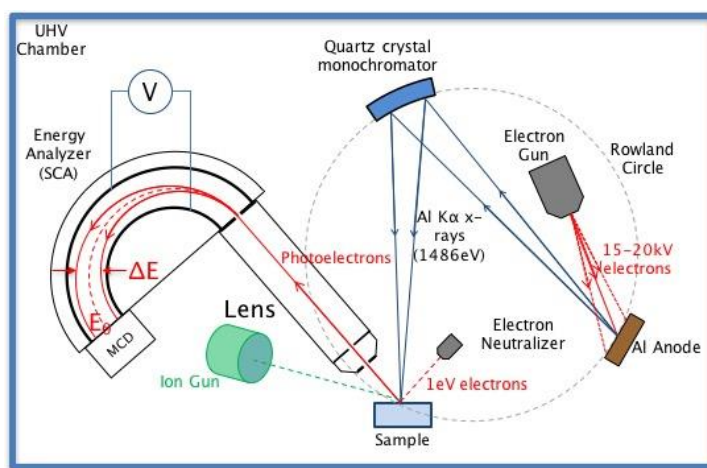


**Figure 38.** Primary concepts of x-ray photoelectron spectrometer.

The PHI Versaprobe 5000 (Physical Electronics Inc., Chanhassen, MN) was used to perform XPS surveying elemental spectra analysis of the barium titanate thin films. The base pressure of the XPS main chamber is  $10^{-8}$  Pa, which is sufficient for running an experiment for more than 24 hours and accumulating only one layer of carbon on the surface. The Versaprobe is equipped with a focused x-ray beam that allows for 10 to 100  $\mu\text{m}$  spot size. The x-rays were generated from an aluminum target and aluminum K $\alpha$  x-rays were monochromated and focused on to the film using the Rowland circle geometry. The energy of the Al K $\alpha$  x-rays is 1484.2 eV. The electrons that were ejected from within  $\sim 5\text{nm}$  of the surface, typically with a  $45^\circ$  takeoff angle (TOA), were collected and analyzed by electrooptics and filtered using a hemispherical



analyzer. The stage has five axes of movement, including xyz translation, rotation, and tilt. It is this latter degree of freedom that made angle resolved XPS (ARXPS) useful for determining the layering.

Angle resolved photoelectron spectroscopy was used to become more surface sensitive. As the take-off angle was lowered, more material was put in between the electron and the detector. So, while the electron mean free path in the material did not change, the depth from which the electrons could escape did. This was extremely useful in determining where the chemical composition was coming from in the sample, if it was not uniform.

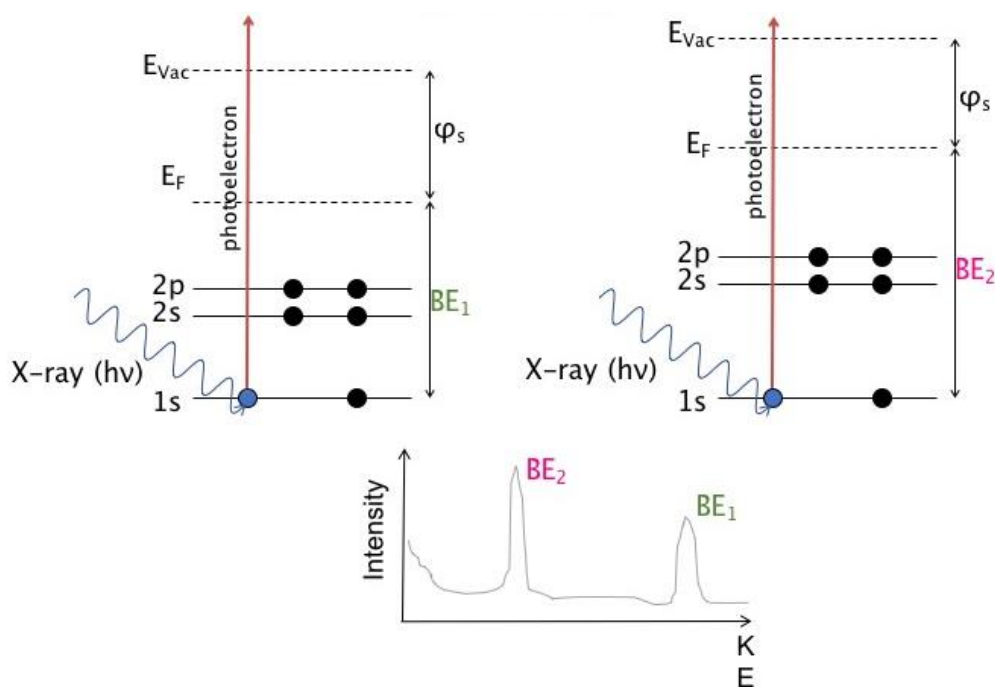


**Figure 39.** Binding energy (BE) of an electron is defined as the energy difference from the core level to the fermi level. The BE uniquely identifies an atom chemically.

As a general step for XPS, a survey spectrum was always taken first in order to prove that only barium, titanium, oxygen, and carbon were found. Following the survey, elemental scans were performed based upon which elements were discovered in the survey spectrum. The survey spectrum also helped set up a strategy for determining which electron levels of the elements had

the most intensity and which ones, if any, overlapped. The Ba3d<sub>5/2</sub>, Ti2p, O1s, and C1s levels were scanned.

In Figure 40 an abbreviated survey spectrum shows the barium 3d<sub>5/2</sub>, the titanium 2p, and the oxygen 1s peaks. All barium titanate films had a very weak carbon 1s peak from the adventitious carbon from transporting the sample between the MBE and the XPS. There were no overlaps between any of the barium, titanium, or oxygen collection peaks. The above mentioned core levels could be used for binding energy determination and elemental ratios. In barium titanate, the titanium dioxide is extremely stable. The titanium 2p<sub>3/2</sub> and 2p<sub>1/2</sub> peaks were used together for ratio determination, since their separation was smaller. This increased the accuracy of the ratio determination especially since the analysis of XPS was focused on the titanium-to-barium ratio of the film. In contrast, just the Ba 3d<sub>5/2</sub> peak was used for analysis since the energy separation between it and the 3d<sub>3/2</sub> peak was significant enough to clearly curve fit the peak. Traditionally, carbon is used as a reference for correcting the binding energies, but since the carbon peaks were so low due to the quick transfer between MBE and XPS chambers, it was

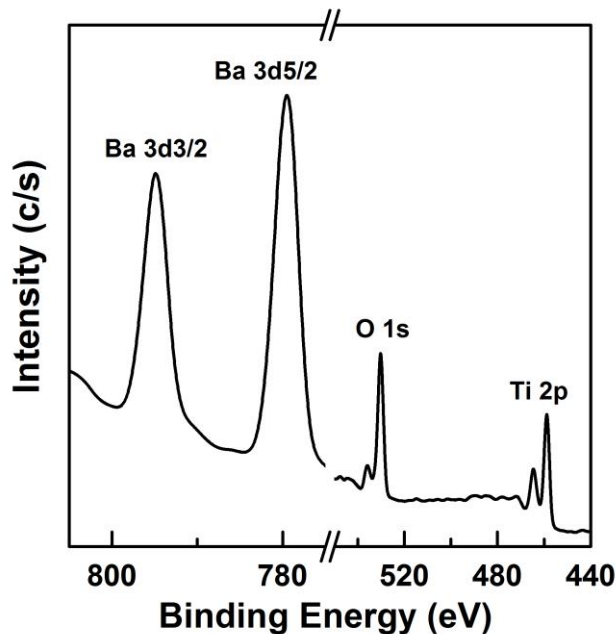
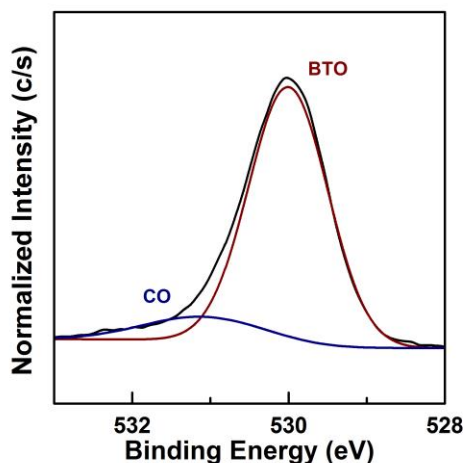


Figure 40. Partial XPS survey spectrum of a BTO film.

found that using the very stable Ti 2p<sub>1/2</sub> peak was more reliable in detecting any changes in binding energy shifts of the barium or oxygen atoms. The 2p<sub>3/2</sub> peak binding energy for titanium was set to 458.8 eV corresponding to the NIST database [142]. Furthermore, from all peak fittings for the titanium 2p peaks, the single Gaussian fitting indicated that there was no second chemical environment.

The oxygen 1s peak (Figures 40-41) from XPS showed two different chemical environments. The stronger lower binding energy peak at 530 eV was from barium titanate. The higher energy shoulder was attributed to adventitious oxygen in the form of carbon dioxide at around 530.15 eV. When looking at ratios for barium titanate, the adventitious oxygen was eliminated so that the stoichiometry would represent only that which was from the barium titanate. Furthermore, the carbon was used to increase the accuracy of the titanium-to-barium ratios by eliminating the filtration of different energy photoelectrons [143]. Hydrocarbons accumulated on the surface of samples that had been exposed to atmosphere when transferred from UHV growth chamber to UHV analysis chamber in the XPS. While the exposure time to atmosphere varied, the carbon correction in the analysis ensured quantitative comparisons were accurate. Additionally, a technique was developed to reduce the carbon overlayer to an equal thickness for every sample which will be discussed in Chapter 4.



**Figure 41.** Oxygen curve fit showing surface oxygen and BTO oxygen.

The barium peak (Figure 42) provided the most interesting insight into how changing the barium and titanium shutter times affected the chemical composition of the barium titanate thin films. The barium  $3d_{5/2}$  and  $3d_{3/2}$  peaks both showed a shoulder to the higher binding energy side. The dominant peak was at 779 eV related to barium titanate and the 781 peak was related to a surface BTO reconstruction that was barium rich [104], [144], [145]. In the literature, this surface chemistry is similar to BTO but has a lower electron density and is present in bulk barium titanate even when freshly cleaned in UHV environment [146]. The entire  $3d_{5/2}$  peak was used to calculate the titanium-to-barium ratio of the films. For thorough analysis, the barium peak was curve fitted for every barium titanate thin film.

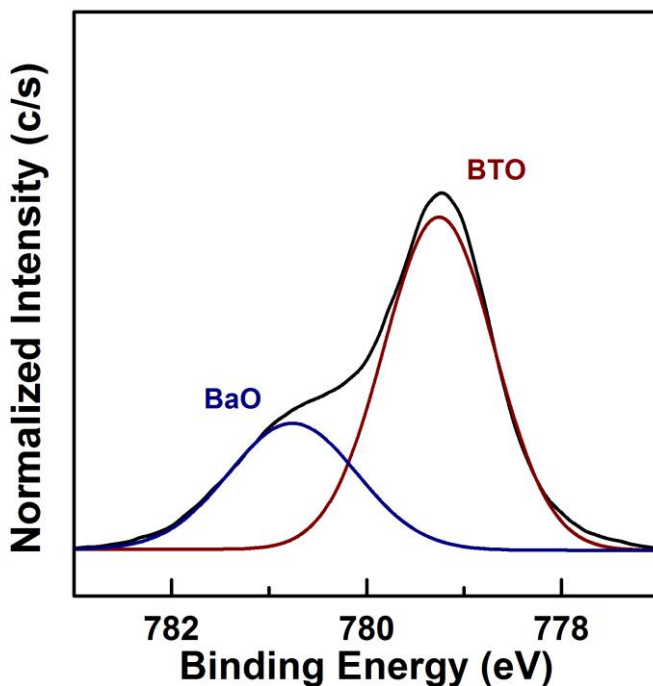


**Figure 42.** Barium  $3d_{5/2}$  curve fit showing two chemical environments: BaO and BTO.

A complete analysis of the curve fitting for all of the elements and the ratios were completed for all the barium titanate thin films. In Table 6, a specific example of that analysis is given. However, many of the parameters such as binding energies for all of the elements and

many of the full width half max (FWHM) were identical for all of the samples so the analysis focused on the differences which will be highlighted in the results section below.

**Table 6.** Summary of XPS analysis of a BaTiO<sub>3</sub> thin film.

	XPS TOA		Ba 3d <sub>5/2</sub>		Ti 2p <sub>3/2</sub>	O 1s		Sr 3d <sub>5/2</sub>
			BTO	β		BTO	Surface	
Before Methanol Cleaning	45°	BE (eV)	779.03	780.41	458.84	530.07	531.77	133.7
		FWHM	1.21	1.81	1.07	1.2	1.68	1.05
		Stoichiometry	22.32%		19.53%	56.83%		1.32%
			60.1	39.9		84	16	
	15°	BE (eV)	778.97	780.43	458.77	530.07	531.79	
		FWHM	1.23	1.84	1.12	1.22	1.68	
		Stoichiometry	25.09%		21.37%	53.54%		
			38.63	61.37		77.56	22.44	
After Methanol Cleaning	45°	BE (eV)	779.02	780.35	458.8	530.06	531.7	133.67
		FWHM	1.3	1.69	1.12	1.23	1.68	0.94
		Stoichiometry	17.90%		22.46%	58.44%		1.19%
			76.85	23.15		84.18	15.82	

Additional XPS experiments were performed as needed during different parts of this investigation. The barium titanate thin films were cleaned in methanol for piezoforce microscopy measurements as will be discussed in the next chapter. Also, the surface barium oxide peak was proven to be surface related through angle resolved x-ray photoelectron spectroscopy. The focus of the XPS analysis was to determine the impact of titanium-to-barium shutter time ratio on the stoichiometry of the BTO films, thus the Ti/Ba was calculated for every sample. Furthermore, since x-ray diffraction showed very little lattice parameter change for an average throughout the film, it was interesting to discover that the stoichiometry changed at the surface post methanol cleaning.

### 3.2.2 XPS Results

The titanium-to-barium ratio of all of the films were extracted from the elemental analysis. The titanium peaks were not different in any way and were comparable from sample-to-sample. However, there was a significant difference in the barium 3d peaks. For example (Figure 43), when a sample was shown to be titanium-rich, the barium oxide shoulder was less than in the barium-rich case. It was interesting that the surface barium oxide amount changed with a change in the titanium-to-barium shutter time.

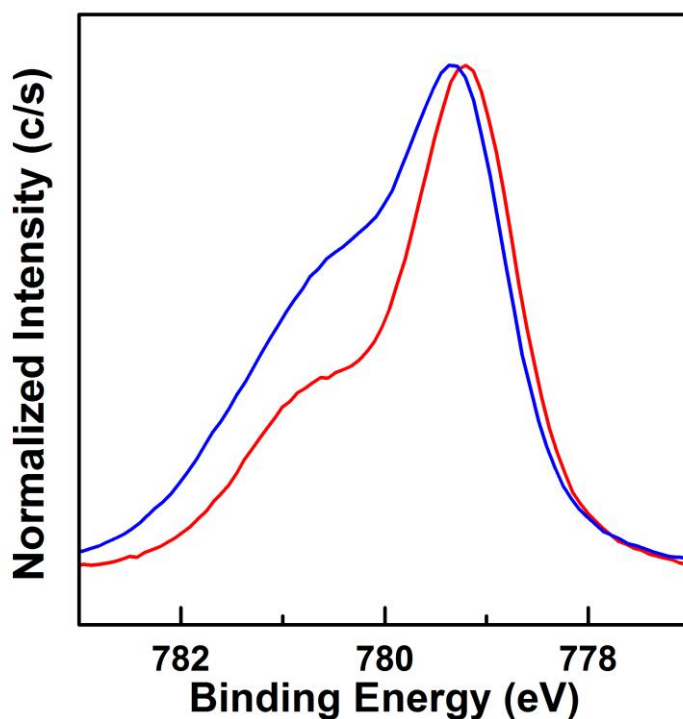


**Figure 43.** Barium rich (blue) vs barium poor (red) comparison of Ba 3d<sub>5/2</sub> peak.

Immediately following the growths, the titanium-to-barium ratios for all of the films with the same shutter time ratios were found to be highly variable, within the range from 0.65 to 1.23, which was a much wider variation in stoichiometry than was subsequently determined by XRD  $2\theta$ - $\omega$  peak positions. Furthermore, the barium oxide full width at half max on the barium-rich samples was wider than all of the titanium rich samples (Table 7) indicating that it was the

change in barium oxide surface that was giving rise to this. The XRD analysis did not show the existence of the surface BaO layer. Actually, it is not reported in the literature what a barium-rich XRD lattice parameter should be, so there was nothing to compare it to. Complementary to this, in terms of the ratio of barium oxide to barium titanate in the barium rich samples, the barium rich samples had higher values than 0.5.

**Table 7.** BaTiO<sub>3</sub> XPS analysis (BC – Before Cleaning, PC – Post Cleaning).

<b>Sample</b>	<b>Ti/Ba (BC)</b>	<b>Ti/Ba (PC)</b>	<b>BaO FWHM</b>	<b>BTO FWHM</b>	<b>BaO/BTO</b>
<b>OG029</b>	0.78	1.18	1.73	1.29	0.569
<b>OG031</b>	1.07	1.47	1.54	1.33	0.404
<b>OG032</b>	1.23	1.40	1.54	1.33	0.437
<b>OG033</b>	0.68	1.08	1.77	1.28	0.649
<b>OG034</b>	0.65	1.16	1.82	1.24	0.993
<b>OG035</b>	1.12	1.45	1.65	1.27	0.496
<b>OG036</b>	1.11	1.38	1.60	1.28	0.495
<b>OG037</b>	1.04	1.34	1.63	1.26	0.456

XPS analysis indicated a difference from the XRD analysis in terms of the stoichiometry of the films. The surface composition was different than the stoichiometry throughout the thin film; XPS also indicated a change in stoichiometry post methanol cleaning as shown in Figure 44. The discrepancy between surface and the entire film is further discussed in Chapter 5. The amount of BaO on the surface varied between titanium-rich and barium-rich samples. The impact of stoichiometry on ferroelectricity was investigated and is presented in Chapters 4 and 5.

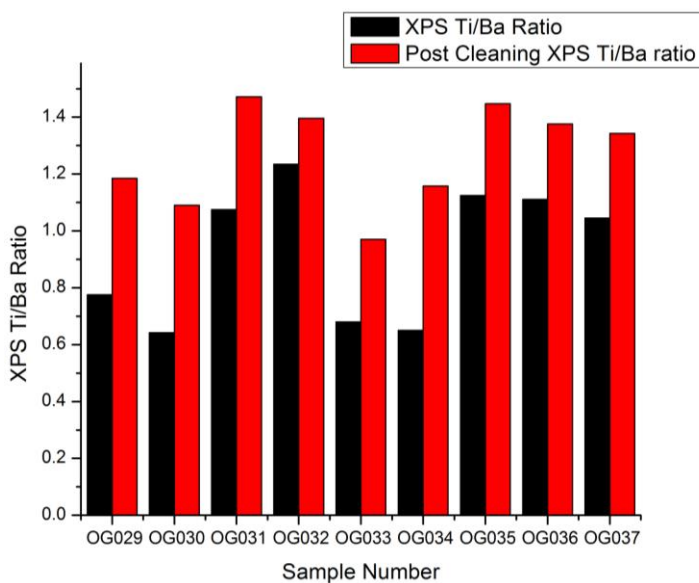


**Figure 44.** Cation ratio change before and after methanol cleaning.

### 3.2.3 Barium-Rich Surface Layer

To validate that the extra barium oxide found in these films was from the surface, ARXPS studies were performed. In addition to the 45° TOA, the same elements were scanned with a 15° TOA thus becoming more surface sensitive. Of particular interest, the barium 3d<sub>5/2</sub> peak was curve fitted for both 45 and 15° angles. Overall, the difference found was that the barium oxide peak increased when the take-off angle was shallower at 15 degrees (Figure 45). This was true for all of the barium titanate thin films.

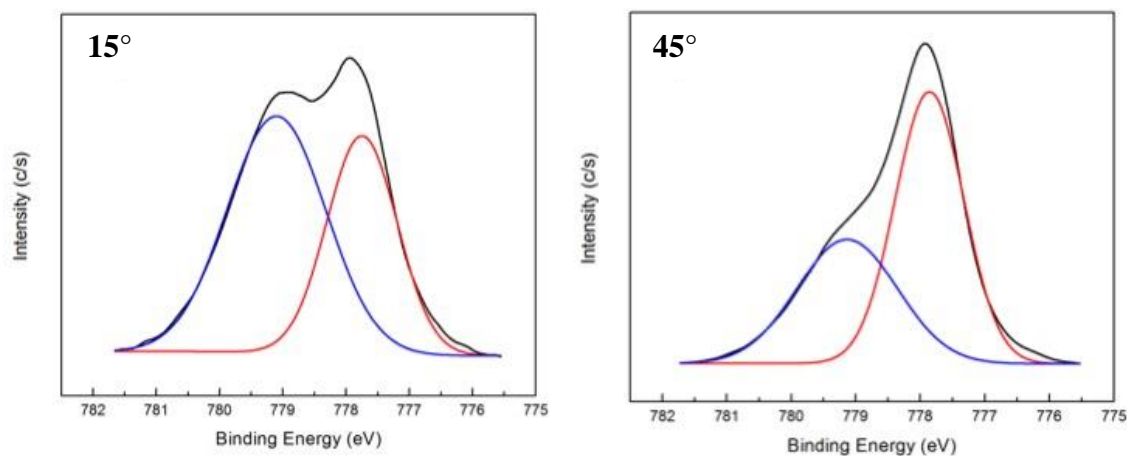


**Figure 45.** Comparison of Ba3d<sub>5/2</sub> Curve fitting showing increase in surface BaO peak when changing to more surface sensitive angle (15°).



### 3.3 Thin Film Morphology

Atomic force microscopy (AFM) is a technique that allows for sub-nanometer Z resolution to investigate the morphology of surfaces. AFM relies upon the atom-atom (probe-surface) interaction modeled by the Lennard-Jones potential. The XY resolution of AFM is limited by the tip radius which, in these experiments, was an average of 10 nm. An AFM consists primarily of a scanner, a probe, a laser, and a feedback system in order to collect the data. A schematic of an AFM is shown in Figure 46. The cantilever bends as the interaction between the sample and probe increases. The interaction increases when the probe encounters a feature that is taller than its surroundings. The change in interaction is then compared to the setpoint and the piezotube is adjusted so that the interaction is restored to the setpoint level. The scanning is accomplished by applying voltages along the side of the piezotube.

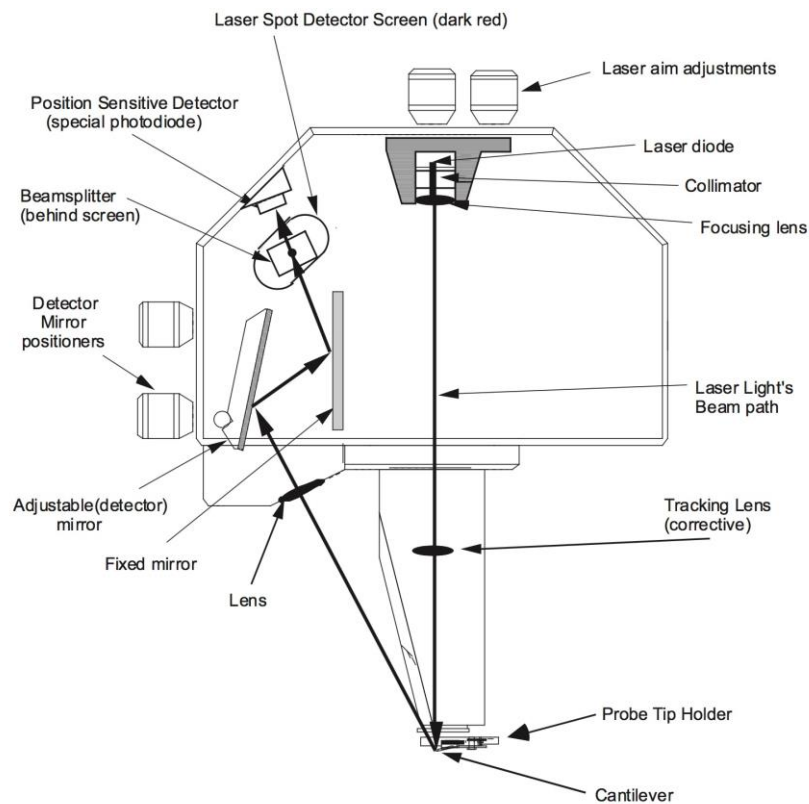


**Figure 46.** Basic components of a Bruker Dimension 3100 AFM head [149].

AFM was used to determine the surface roughness of the barium titanate thin films. The surface morphology revealed a difference in morphology between barium-rich and titanium-rich growth conditions. The streaky RHEED pattern throughout all of the growths indicated a smooth surface should have resulted. The barium-rich samples were rougher than the titanium-rich samples. All of the titanium-rich samples had a surface roughness around 0.19 nm while the barium-rich samples had a surface roughness of 0.3 nm or greater as shown in the Figure 47.

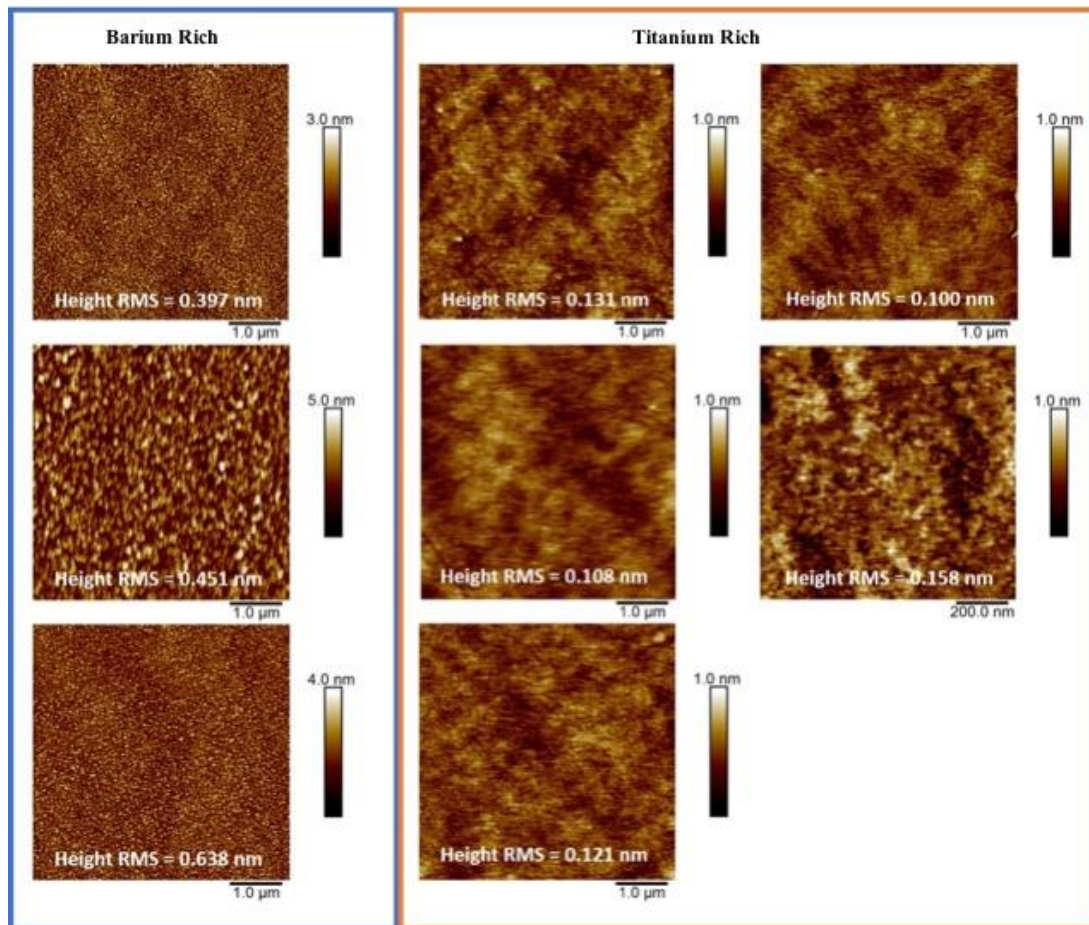


**Figure 47.** Comparison of morphology based on barium-rich vs. titanium-rich.

Both XPS and AFM indicated that excess barium oxide accumulated at the surface. Explaining why the excess barium oxide formed three dimensional structures on the surface is another research topic. However, one possibility was that the excess barium accumulated at the

surface during growth and would prefer to bond to each other rather than to the barium titanate film underneath. In contrast, the titanium-rich samples allowed for excess titanium to incorporate into the thin film and gave a smoother surface. Exploring how the excess barium accumulated at the surface will be discussed in Chapter 5. The impact of excess barium oxide on the ferroelectric properties will be discussed in Chapters 4 and 5.

## Chapter 4: Ferroelectric Properties of Barium Titanate Thin Films

The ferroelectric properties of barium titanate thin films were compared using a quantitative piezoforce microscopy technique. A procedure was developed to reduce the standard deviation of the piezoelectric coefficient to ~20%. Key factors that impacted the standard deviation were identified: surface cleaning, tip force, and probe shape. Strategies to reduce the variation in measurement each factor introduces are discussed.

### 4.1 Piezoforce Microscopy

Piezoforce microscopy is a scanning probe technique used to measure an electromechanical response of a surface. A metal-coated probe allows application of voltages for poling and sensing. The technique takes advantage of the inverse piezoelectric effect in which applying a voltage causes a mechanical displacement [147]-[149].

The mechanical expansion detected in PFM is on the order of picometers for thin films [150]-[152]. Typically, AFM measures nanometers and has angstrom resolution. An order of magnitude lower, requires the use of a lock-in detector in order to extract a small signal from the large signal generated from typical movement of the AFM probe. The AC voltage applied during sensing is a reference frequency and phase that allows for the small signal on the photodiode to be detected through frequency comparison in the lock-in detector (Figure 48).

A ferroelectric response from a known ferroelectric material is visualized in PFM through the creation and detection of domains. A typical PFM experiment first creates  $180^\circ$  domains through application of a DC bias (e.g.  $\pm 10$  V). The sample is biased between the top contact, the conductive probe, and the sample stage. To detect the domains, an AC voltage is applied with a frequency between 20-60 kHz. As the probe is scanned over the surface, the signal from the

photodiode is sent to the lock-in with two channels; the X (i.e. InPhase) channel is the component that is in-phase and the Y (i.e. Quadrature) is out-of-phase with the applied AC voltage. In a ferroelectric, the c+ domain will oscillate in-phase and c- out of phase with the AC voltage. The amplitude and phase are calculated from these channels. The contrast in the phase image of the poled areas is a visualization of these domains. Since there is no DC field being applied, the domains could represent proof of a ferroelectric material[153]-[155].

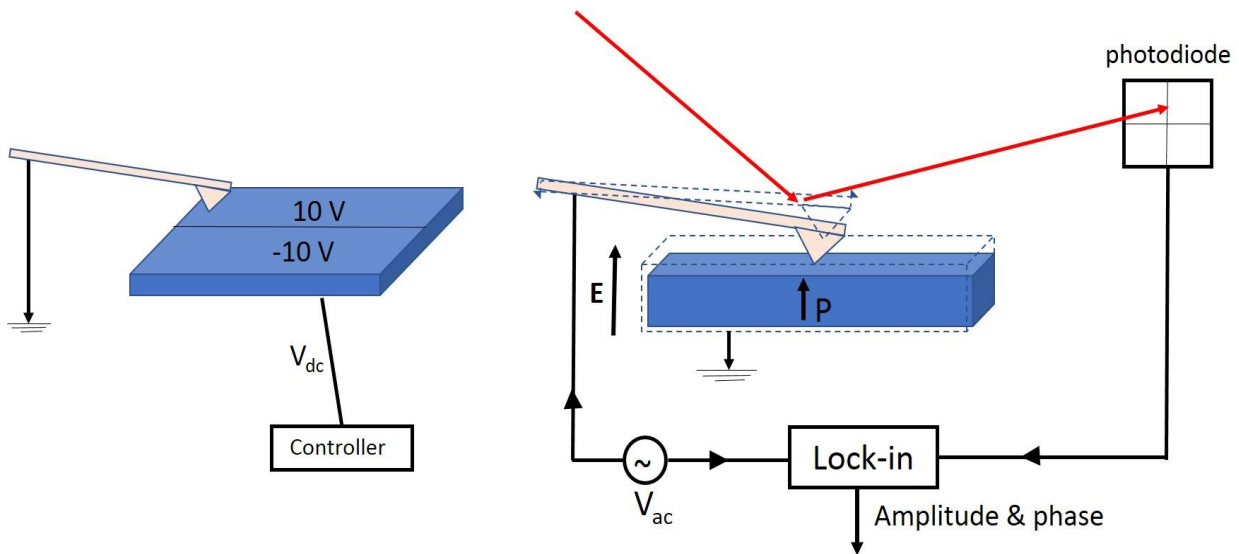


**Figure 48.** A PFM experiment consists of poling with DC voltage (left) and sensing the poled regions with AC voltage and a lock-in detector.

PFM can also measure hysteresis loops. Similar to a polarization-electric field hysteresis loop, a saw tooth voltage signal can be applied via stationary probe and the piezoresponse measured. Typically, in PFM a phase vs voltage loop is created as shown in Figure 49. Also the analog to the C-V loop in PFM is an amplitude-voltage loop. The phase-voltage hysteresis loop is not helpful in comparing ferroelectric properties because the amplitude of the phase will not change with polarization. Furthermore, the DC poling voltage used to create hysteresis loops are not pulsed in the Bruker D3100 Nanoscope V controller (Bruker, Inc., Tucson, AZ), which

contribute to the measured piezoresponse. A component of the piezoresponse is coupled when a  $V_{DC}$  is applied through the cantilever as shown in the following equation:

$$PR_{\omega,ES} = k^{-1}C'V_{DC}V_{AC} \sin(\omega t), \quad (\text{Equation 5})$$

where  $PR_{\omega,ES}$  is the measured piezoresponse,  $k$  is the spring constant of the probe,  $C'$  is the capacitance between the cantilever and the surface,  $V_{DC}$  is the DC voltage on the probe during measurement,  $V_{AC}$  is the applied AC voltage to sense the PR, and  $\omega$  is the frequency of the

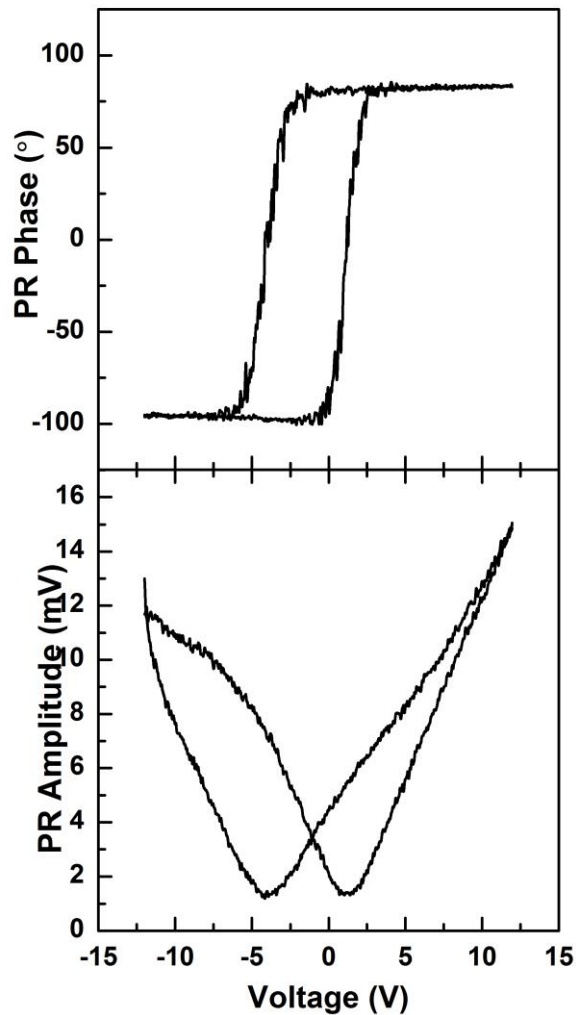


**Figure 49.** Piezoresponse hysteresis loops (top) phase and (bottom) amplitude.

applied AC voltage. Extracting the DC component would not be straightforward, so the focus of piezoelectric coefficient determination relied on creating micron sized 180° domains (Figure 50).

In a ferroelectric material, the piezoelectric coefficient is related to the polarization as shown in the following equation:

$$d_{33} = 2\epsilon_{33}QP_s, \quad (\text{Equation 6})$$

where  $d_{33}$  is the piezoelectric coefficient in the +z-direction,  $\epsilon_{33}$  is the permittivity in the +z-direction,  $Q$  is the electrostriction, and  $P_s$  is the polarization in the +z-direction (out-of-plane).

$d_{33}$  can be extracted from domains as seen in Figure 50; the piezoelectric coefficient allows for quantitative comparison between samples of ferroelectricity.

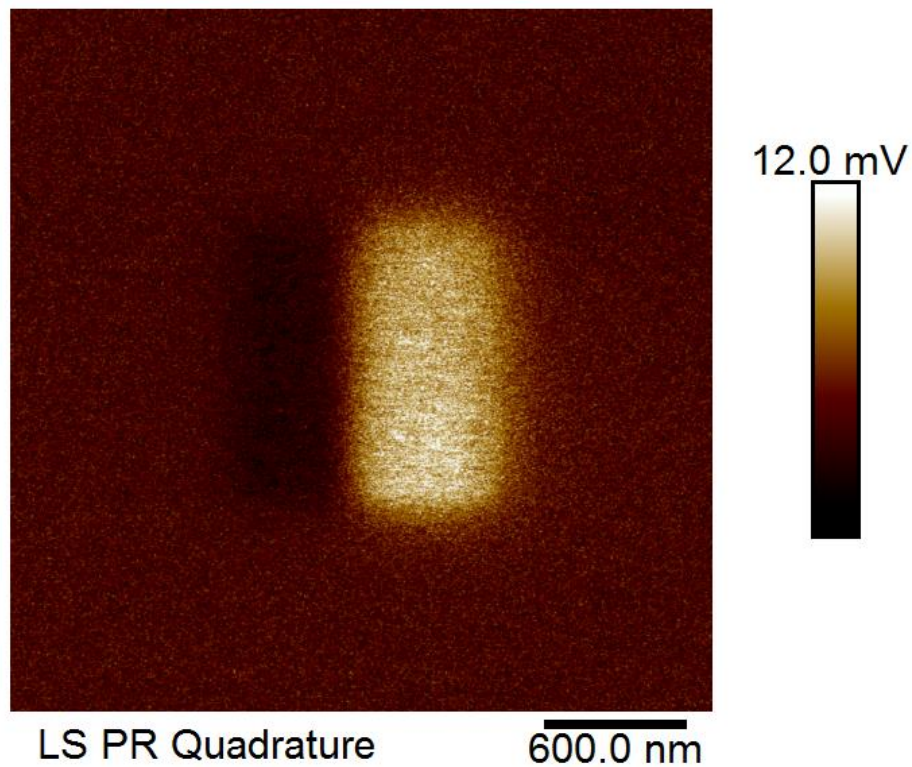


**Figure 50.** Piezoresponse data from a BTO film poled with -3 VDC (dark area on left) and +7 VDC (bright area on right).

## 4.2 Quantitative PFM

While piezoforce microscopy has been used since the 1990s to investigate ferroelectricity, developing it for quantitative comparisons has been an active area of research in for more than a decade. While the piezoelectric response of the system is ideally just the mechanical expansion of the film, there are many factors that contribute to a piezoresponse. Many of the factors are environmental and are hard to completely remove. The method developed by Soergel et al. [156]-[160] that is the basis for extracting the piezoelectric coefficient from a PFM measurement (Figure 51) is discussed.

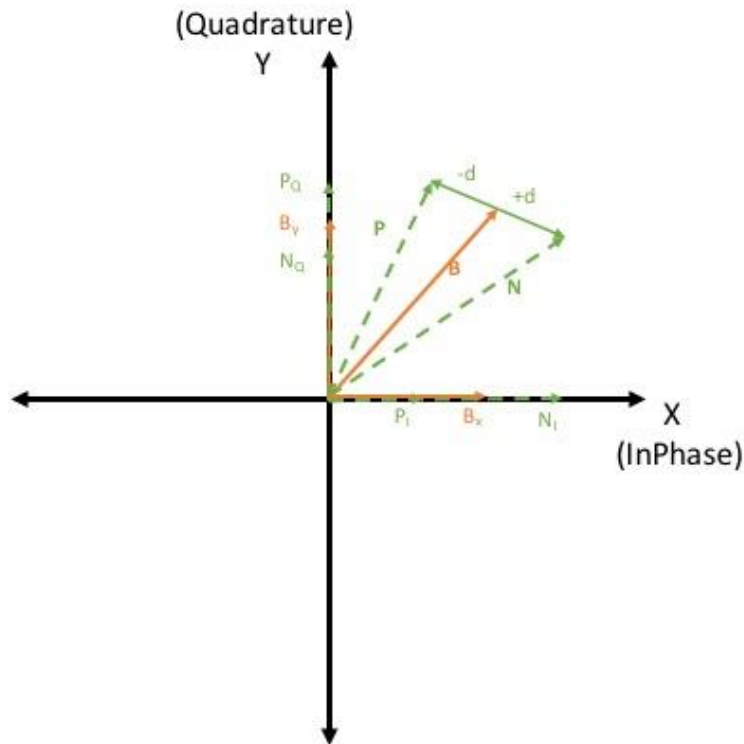


**Figure 51.** Many factors contribute background noise; vector analysis of PFM response helps to identify those sources.

One of the primary discoveries made by Soergel et al. [158] was the background noise from the system. While glass has no piezoresponse, when an applied ac field was applied over a wide range in the kHz frequency range, the piezoresponse varied widely indicating a background



signal from the system (Figure 52). The background signal is also phase dependent. The measured response is a combination of the real piezoresponse and the background. The piezoresponse can be considered a vector (Figure 51). In order to obtain the real piezoresponse, the background must be subtracted out of the measurement.

The measured vectors (Figure 51) can be broken up into the x and y components. For example,  $P_i$  is the x component (i.e. the in-phase component of the piezoresponse) and  $P_Q$  is the y component (i.e. the out-of-phase, or quadrature, component of the piezoresponse). The piezoresponse from the positive domain (c+) is represented by the vector  $P$  and piezoresponse from the negative domain (c-) by the vector  $N$ . To simplify the pure piezoresponse, the phase can be adjusted so that the measured signal has a zero in-phase component, leaving just  $P_Q$  and  $N_Q$ . The piezoelectric coefficient is represented by the following equation:

$$\frac{1}{2}(P_Q - N_Q) = d_{33}(\text{mV}). \quad (\text{Equation 7})$$

In order to determine the piezoelectric coefficient, the probe deflection sensitivity is needed along with experimental parameters to convert  $d_{33}$  from mV to picometer per volt as in the equation:

$$d_{33} \left( \frac{\text{pm}}{\text{V}} \right) = d_{33}(\text{mV}) \times \frac{\text{Deflection Sensitivity} \left( \frac{\text{nm}}{\text{mV}} \right) \times 1000 \left( \frac{\text{pm}}{\text{nm}} \right)}{16 (\text{deflection gain}) \times V_{ac}(\text{V})}. \quad (\text{Equation 8})$$

$d_{33}$  in units of pm/V removes the experimental setup and allows for comparing samples to each other. With the basic theory of measurement established, the steps in the measurement process used are described next.

#### 4.2.1 Background Measurement

The background was measured and the frequency selected to minimize the background contribution to the measured signal. Since the probe was part of the system, at the beginning of every measurement a quadrature vs ac frequency measurement was generated. While Figure 52 represents glass, the measurement was typically made on the sample as it merely produced an offset [156], [161], [162]. The frequency was also an important factor in determining the response of the sample. A frequency was selected that had a minimum amplitude; in Figure 52, for example, the frequency around 11 kHz was selected. While 20 kHz would be the lowest, it was near the highest amplitude and slight shifts would make it undesirable. Minimizing the background is important, especially if the piezoresponse of the sample is small. Selecting the

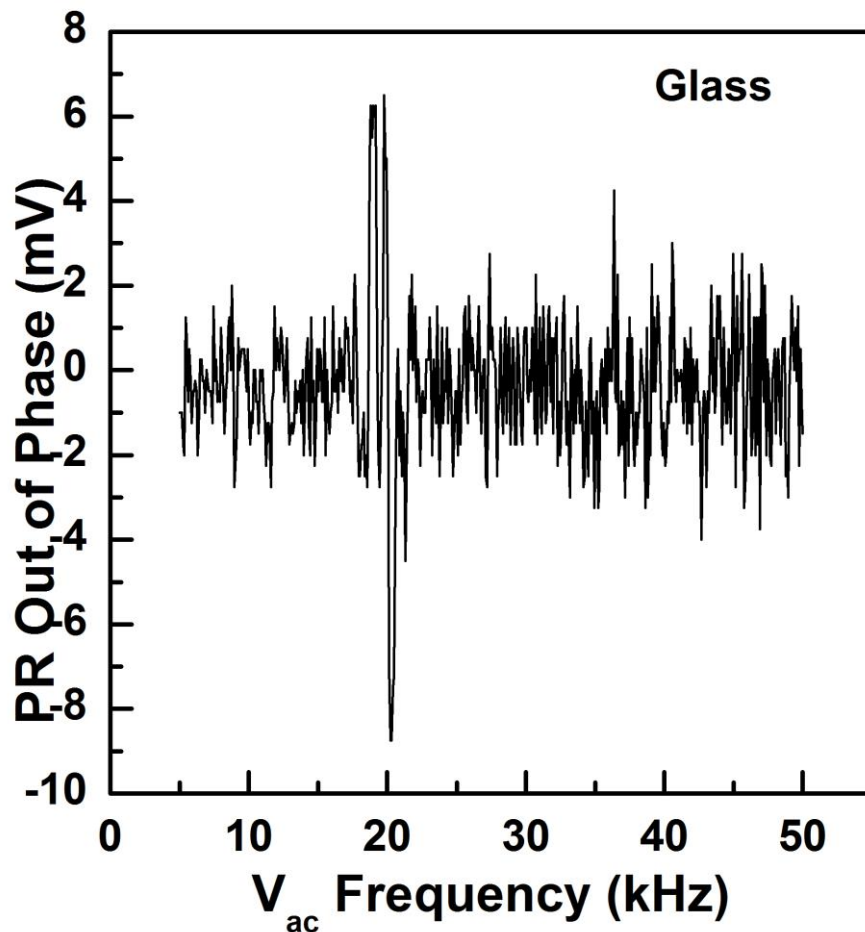
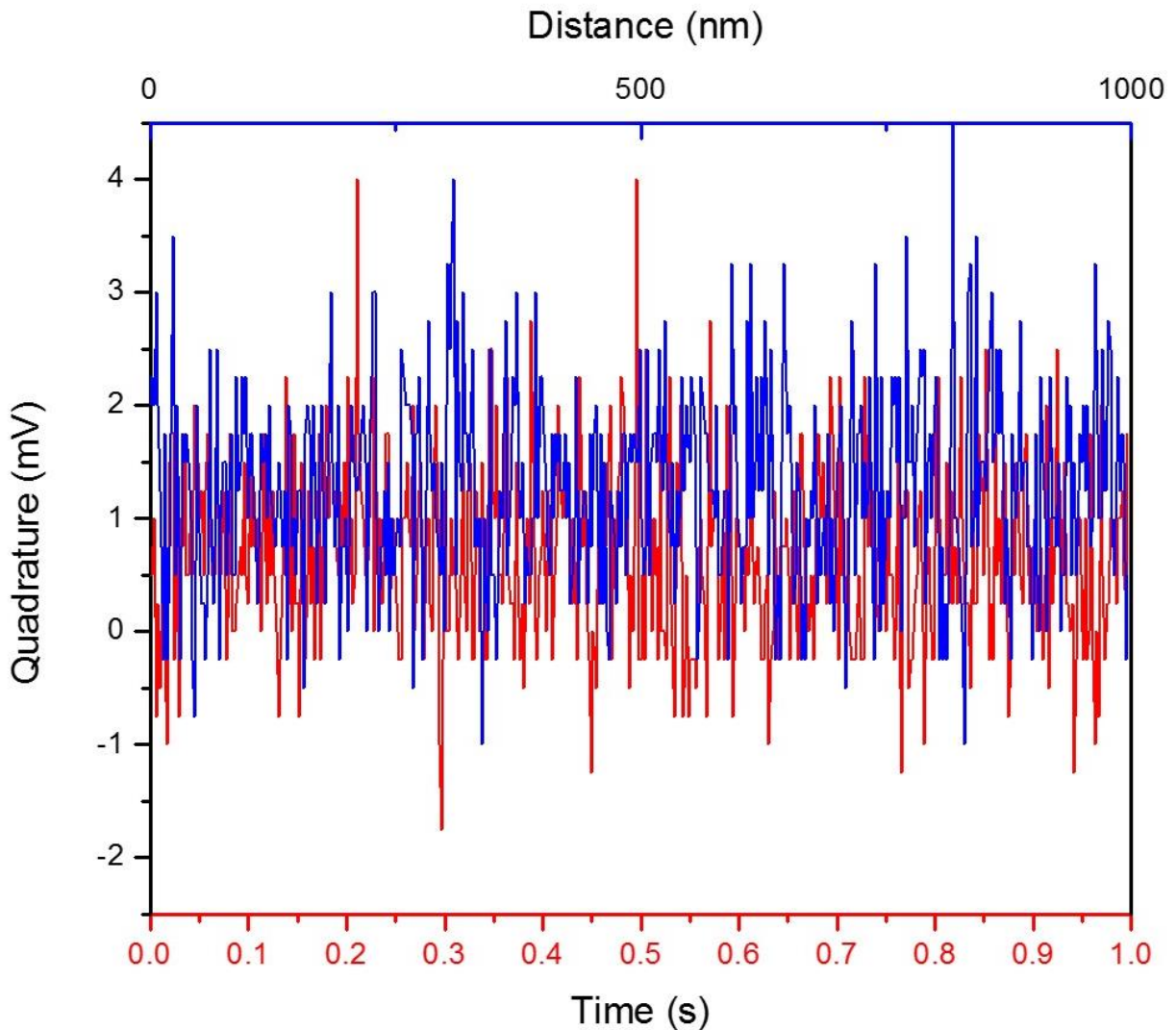


Figure 52. Piezoresponse of glass as function of  $V_{ac}$  frequency.

correct frequency reduced the variance in the measurement. For every probe, the frequency was fixed so that all of the measurements could be compared. Similarly, the relative phase was also fixed to maximize the quadrature and minimize the in-phase. This removed a large part of the variance and made quantitative PFM more viable.

The background noise observed in a measurement was determined by applying an AC field to an unpoled BTO sample. As shown in Figure 53, even when the probe was stationary there was an average 1 mV background signal with a 1 mV offset. The offset came from a capacitive force between the probe and charge on the sample; humidity was a factor in the



**Figure 53.** Time and distance in PFM measurement showing background noise.

magnitude of the offset. The RMS noise represented the lower limit of detectability and could give rise to error in the measurement of  $P_Q$  and  $N_Q$ . The offset was subtracted in the difference between  $P_Q$  and  $N_Q$ .

The deflection sensitivity of every probe was measured. Just like the probe changed the background noise, the deflection sensitivity of every probe was different. A force-distance curve was obtained by lowering the probe a certain distance and watching the photodiode voltage change once engaged upon the surface (Figure 54). The probe was not scanned in the x-y direction during this measurement and thus a stationary deflection sensitivity was obtained. The deflection sensitivity was obtained by curve fitting the engaged part of the force-distance curve (red fit in Figure 54). The slope of the fitted line was in millivolt per nanometers. The inverse of the slope gave the deflection sensitivity in nanometers per millivolt which was then inserted into Equation 8 to calculate the piezoelectric coefficient.

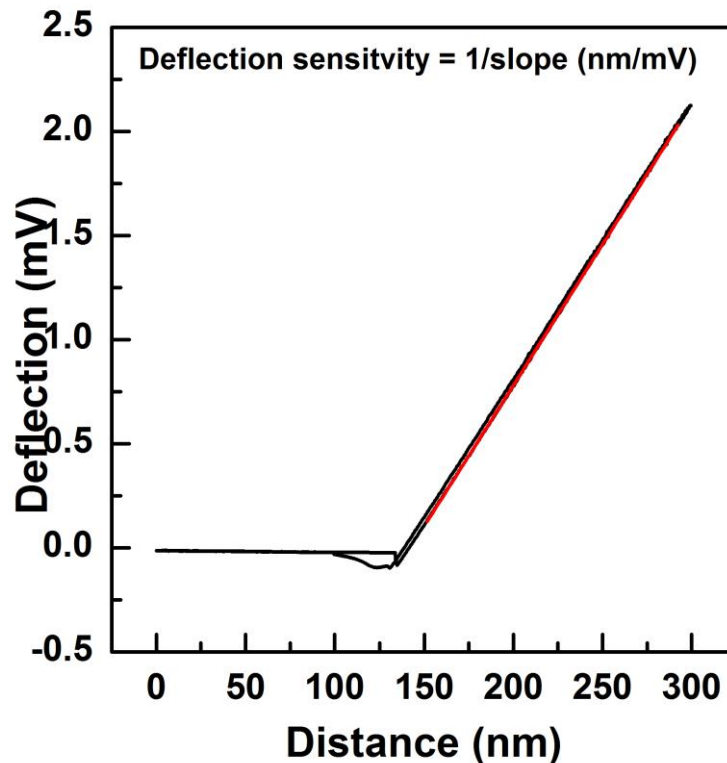


**Figure 54.** Slope of repulsive region in deflection sensitivity curve to extract piezoelectric coefficient.

The background and deflection sensitivity were two measurements done before every probe in order to convert the measured piezoelectric coefficient into one comparable between samples. The way the piezoelectric coefficient was measured will be shown in the next subsection. Additional sections contain strategies developed to handle other experimental factors that introduced large amounts of variation in order to make PFM semi-quantitative.

#### 4.2.2 Measuring the Piezoelectric Coefficient

$d_{33}$  was measured from the quadrature difference in a c+ and c- domain. A  $1\ \mu\text{m} \times 1\ \mu\text{m}$  area was poled half with a positive voltage (e.g. +7V) and half with a negative voltage (-3V). The poling procedure was repeated twice to ensure saturation with a total pole time of 2 hours. A larger negative voltage caused shorting in the film and deformed the surface. A  $3\ \mu\text{m} \times 3\ \mu\text{m}$  area was then imaged with a  $10\ \text{V}_{\text{AC}}$  at the optimized frequency and phase. The quadrature value was measured as shown in Figure 55. The average difference was then measured between the c+ domain, the bright region, and the c- domain, the dark region, using the step height feature in the Bruker NanoScope analysis software (Figure 55). Averaging over the area rather than a single point, such as in a hysteresis loop, improved the accuracy in representing the real signal of the BTO film. The measured piezoresponse difference from the c+ domain to the c- domain was  $P_Q - N_Q$  from Equation 7. Thus, dividing  $P_Q - N_Q$  by 2 gave  $d_{33}$  in mV.

An example of extracting  $d_{33}$  in pm/V from piezoresponse data is described. In Figure 55, the measured piezoresponse in the c+ domain (bright region) has a value of 4.2 mV, thus,  $P_Q = 4.2\ \text{mV}$ . Similarly, the piezoresponse in the c- domain (dark region) has a -0.5 mV value; thus,  $N_Q = -0.5\ \text{mV}$ . The raw  $d_{33}$  is calculated from Equation 7;  $P_Q - N_Q = 4.7\ \text{mV}$ , thus,  $d_{33} = 2.35\ \text{mV}$ . In order to convert  $d_{33}$  to real units, the other experimental parameters are used. The deflection sensitivity for the probe used in Figure 55 was  $80\ \text{nm/V}$ . Using Equation 8,  $d_{33}$  is 3.34

pm/V. Thicker BTO thin films have been reported to take on these values which are correct for bulk BTO as measured by PFM [163].

However, it was quickly found that sequential measurements gave different  $d_{33}$  values. A procedure was developed to determine an accurate value and ensure that the same condition was present for every measurement for quantitative comparison. The factors that altered the  $d_{33}$  values will be discussed in the following subsections along with the procedure on how to determine the correct  $d_{33}$  value.

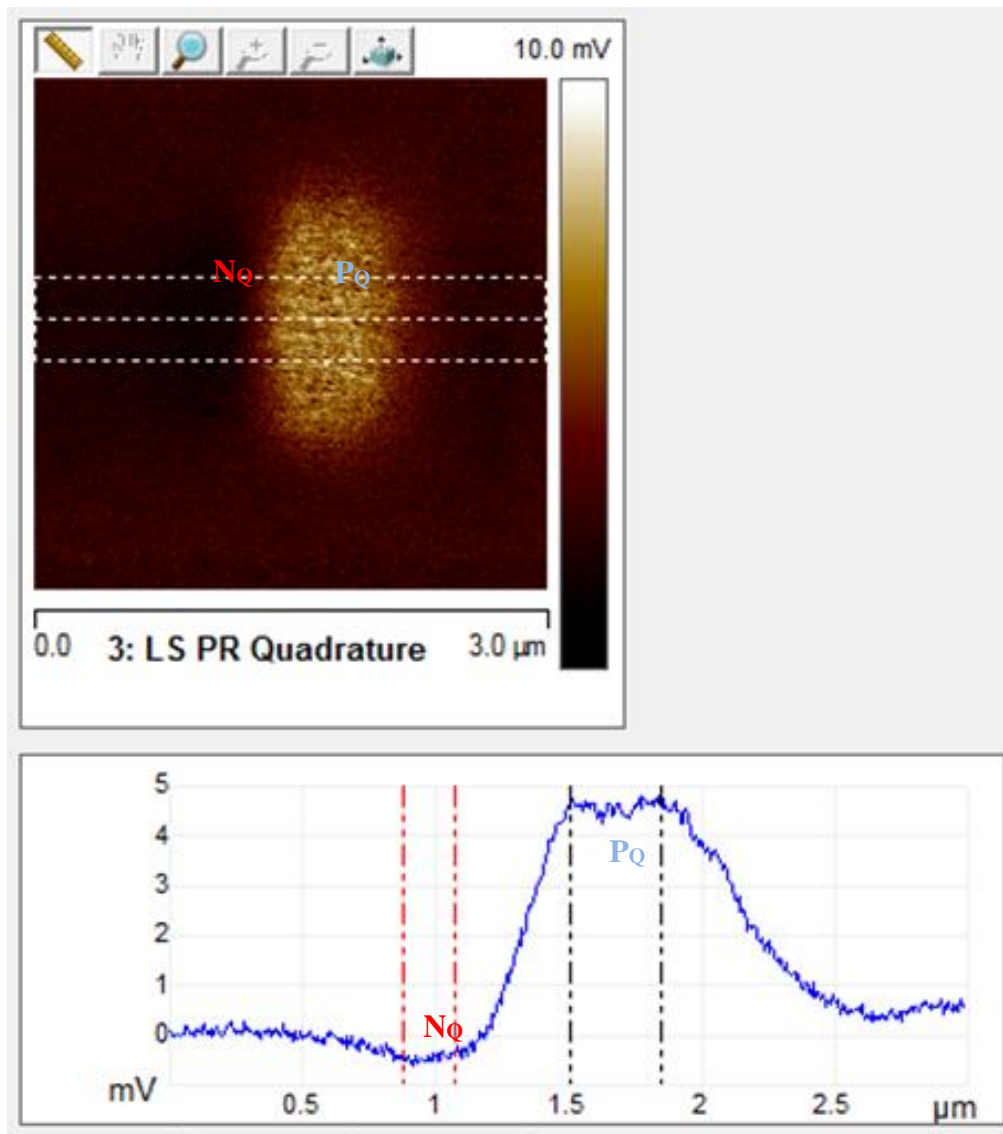


**Figure 55.** Measuring  $d_{33}$  from difference in  $c^+$  and  $c^-$  domains.



### 4.3 Impact of Surface Chemistry on Piezoresponse

The surface chemistry plays a large role in determining the piezoresponse of the BTO thin films [150]. The amount of time a BTO film was exposed to atmosphere increased the thickness of carbon on the surface; the thicker the carbon overlayer, the greater the reduction in  $d_{33}$  observed. A 40 nm thick BTO film was measured immediately after growth. Contrast was observed in the piezoresponse of the sample as shown in Figure 56a. The

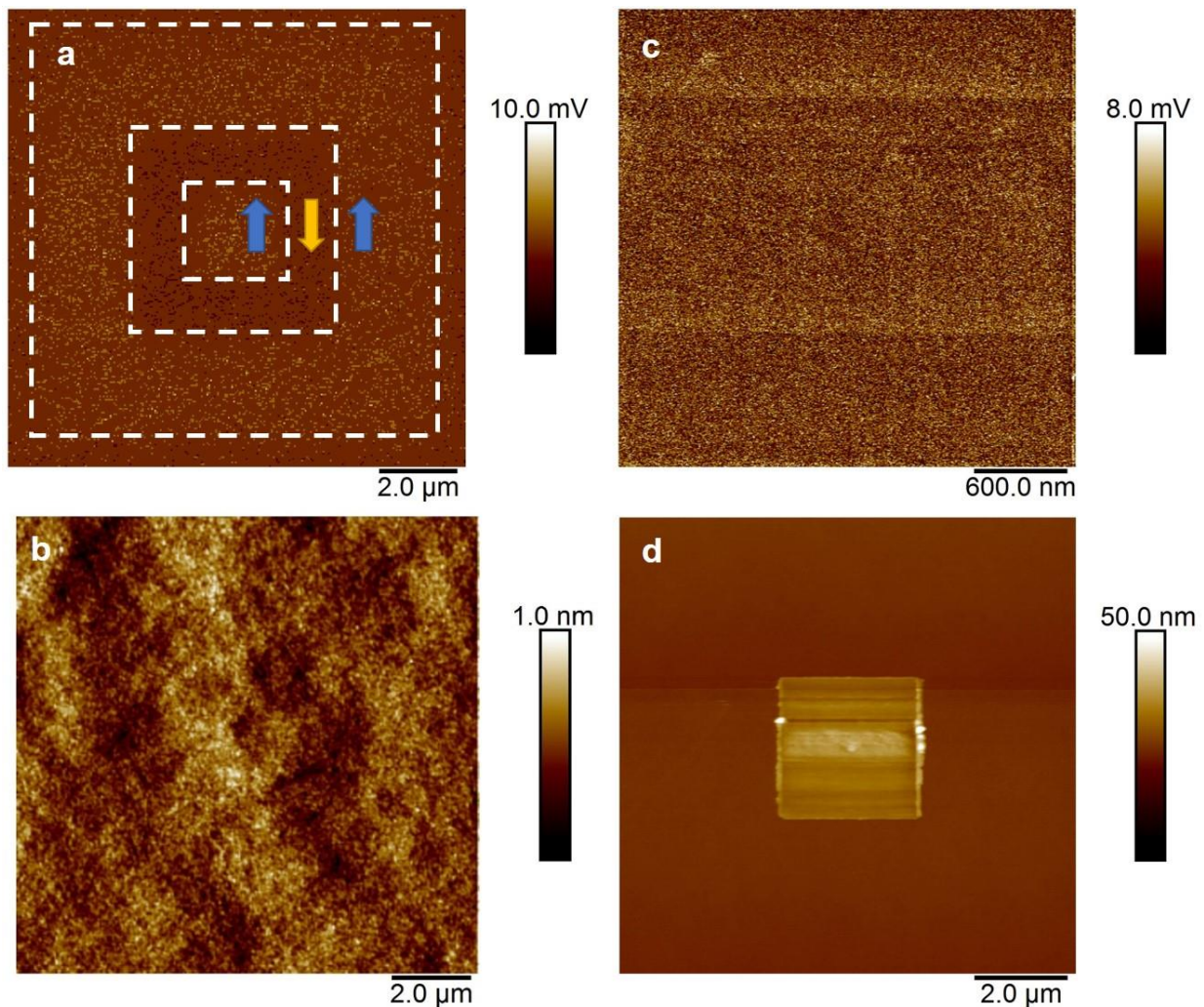


**Figure 56.** (a) Piezoresponse of OG029 immediately after growth and (b) height. Three months later, (c) No piezoresponse existed and (d) large height features observed in the poled area.

corresponding height showed a root mean square roughness around 0.1 nm (Figure 56b), which was expected for a high quality film. However, after waiting several weeks, the piezoresponse was zero (Figure 56c). The corresponding height showed large features covering the entire poled area (Figure 56d). It was found that adventitious carbon from the atmosphere accumulated on the surface and when the voltages were applied to the measurement attracted these charged forms of carbon to the poled area. Since the dielectric constant of carbon is two orders of magnitude less than barium titanate, the voltage drop was almost all in the carbon layer, making the piezoresponse of the BTO too weak to measure. Depending upon exposure time, various amounts could accumulate and give largely varying piezoresponse. In order to reduce the variance of carbon accumulating on the surface, a solvent cleaning procedure was developed to keep the carbon concentration around 14% for all samples. Developing a consistent cleaning protocol before measurement reduced the measurement variance.

#### 4.3.1 Carbon Surface Layer

Carbon accumulated on a BTO film within minutes of exposure to atmosphere. The relative carbon concentration on a 40 nm thin film that had been exposed for several days was ~17% (Figure 57). The sample was sputtered for six seconds at 1 kV and the carbon was completely removed (inset of Figure 57); the black peak represents after exposure for a few days and red curve represents after 6 s sputtering. Then, the sample was exposed to the atmosphere for 15 minutes. The carbon peak increased to 4% and remained at that level after another hour of exposure. The initial carbon accumulation on the surface was known to chemisorb onto BTO [2], [164]-[170]. Through time, a weaker physisorption process allowed for more layers of carbon to accumulate on the surface, which explains the 17% carbon after days of exposure. PFM measurements required a couple of hours to make a single measurement.



In order to compare PFM measurements from samples, the same amount of carbon needs to be on the surface. A method was investigated to control the amount of carbon contamination on the surface and consistently provide the same amount of carbon after applying the procedure. Secondly, since many measurements were done to acquire enough statistics, the procedure should be quick and easily accessible within the lab.

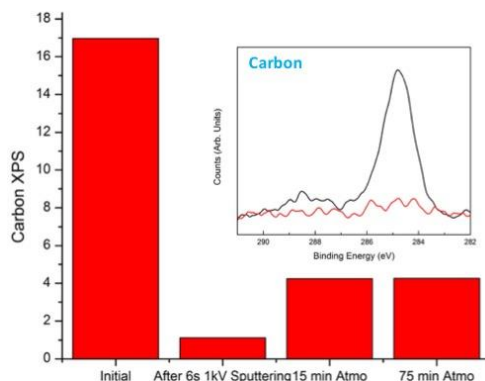


**Figure 57.** Time dependence of carbon accumulating on BTO surface.

#### 4.3.1.1 Solvent Cleaning Optimization

A solvent sonication method was developed to remove carbon from the surface of BTO films and consistently produce ~14% carbon on the surface. A study was performed on solvent cleaning methods and an optimization process was developed to reduce carbon on bulk BTO to a minimum level in the least amount of time. Three solvents were investigated to understand which one would leave the least amount of carbon residue: acetone, methanol, or trichloroethylene (TCE). Application of solvents were investigated and included soaking, mechanical rubbing, and sonication. The amount of time for ultrasonication the sample in each solvent was tested to determine the minimum time needed to obtain the lowest amount of carbon for each. Both AFM and XPS were used to evaluate the results in order to understand which method provided most consistently the lowest amount of carbon in the shortest amount of time.

The optimal solvent cleaning procedure was found to be sonication for 10 minutes in acetone followed by 20 minutes of sonication in methanol. Pieces of bulk BTO were measured by XPS and AFM to observe the amount of height features and determine the amount of carbon remaining on the surface. For the first trial, a single piece would undergo equal times of TCE, acetone, and methanol for 1, 10, 20, and 60 minutes. The second trial included just acetone and methanol for the same time intervals. TCE did not lower the amount of carbon concentration or reduce to the minimum amount more quickly than just acetone and methanol. Overnight soaking in just methanol consistently reduced the carbon on the surface to the same level as the optimal procedure described above, but this approach was considered too long to be practical for making many measurements on different samples within a day. ~14% carbon was repeatedly obtained for all samples after cleaning. To further prove the usefulness of the cleaning procedure, PFM response of the bulk BTO was measured and found to give a  $d_{33}$  value of 4 pm/V. Additionally, polarization domains formed naturally due to the thickness of the sample and corresponded to high or low regions in the height scan as expected for a bulk ferroelectric (Figure 58).

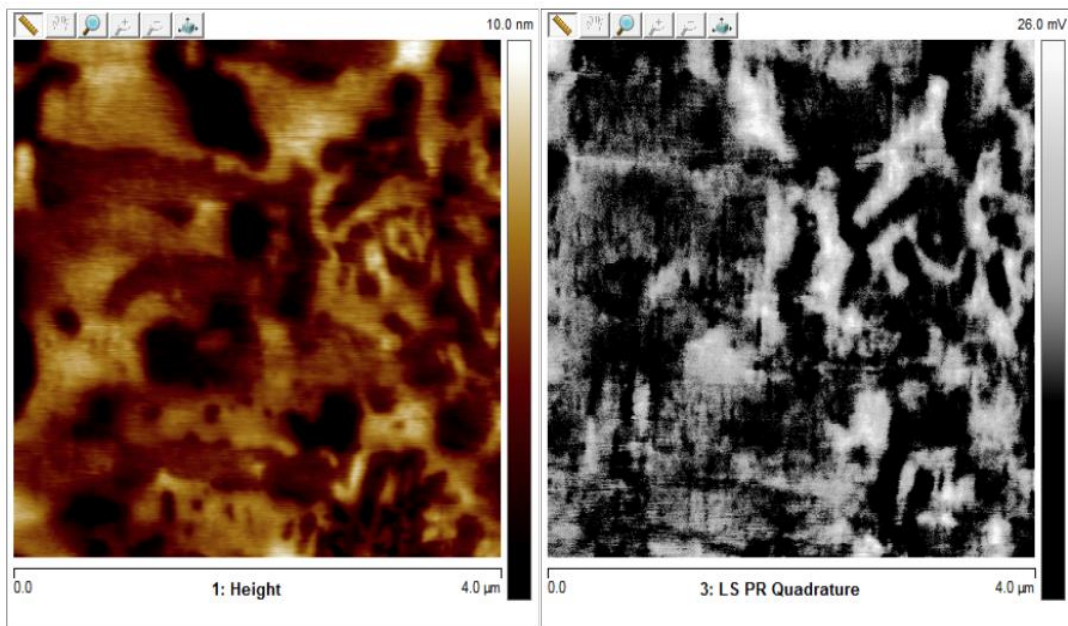


**Figure 58.** Bulk BTO height (left) and piezoresponse (right).

### 4.3.1.2 Oxygen Plasma Cleaning Optimization

Oxygen plasma cleaning procedure was optimized to reduce carbon to ~2% without modifying the surface morphology (Figure 59). However, the surface became charged and altered the piezoresponse. The oxygen plasma cleaning procedure is not recommended for PFM measurements.

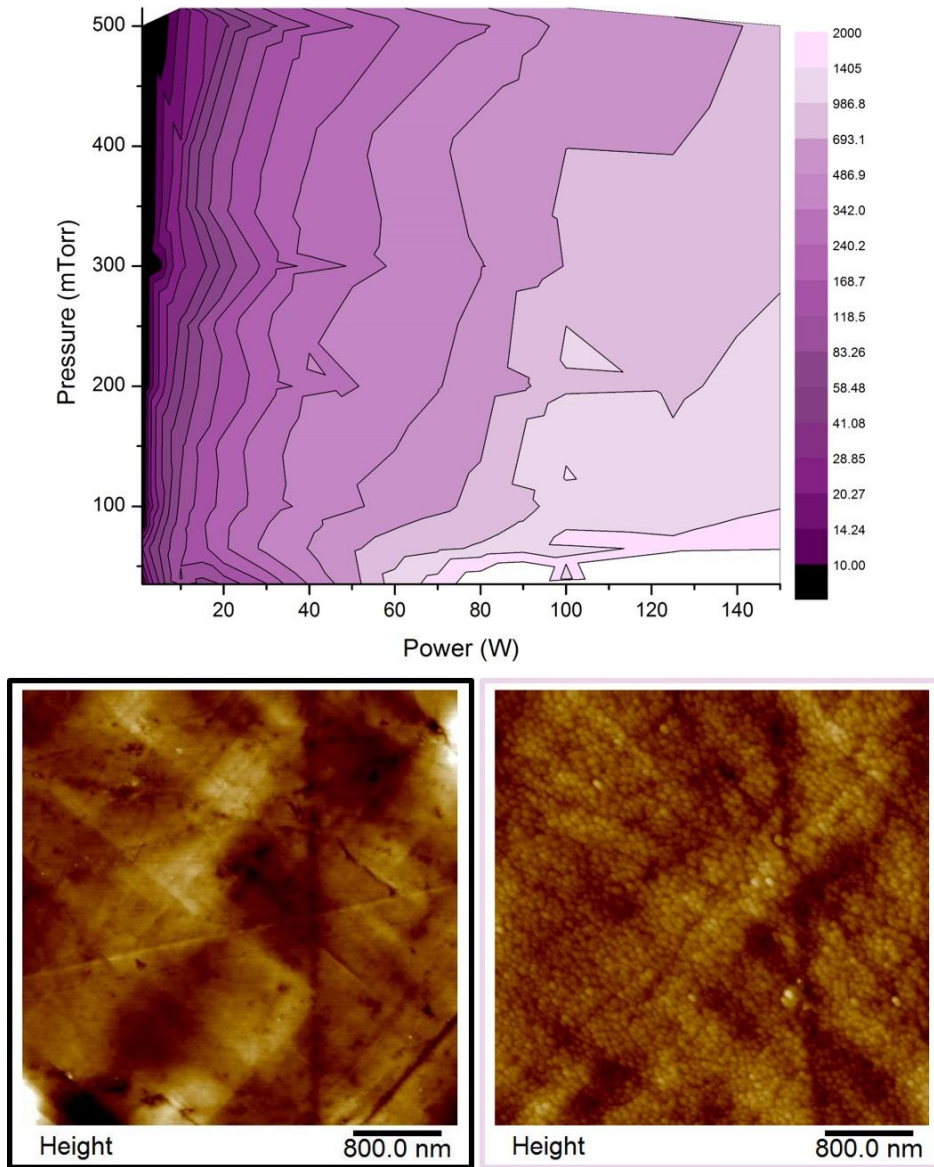


**Figure 59.** Oxygen plasma intensity map (top). Surface morphology at low intensity (bottom left) and high intensity (bottom right).

In order to optimize the surface cleaning, the plasma intensity was mapped as a function of chamber pressure and applied power (Figure 59 top). Pieces of bulk BTO post solvent sonication were exposed to different combinations of power and pressure based on plasma intensity; following the plasma cleaning, AFM was used to examine the morphology of the surface. The oxygen plasma conditions of 500 mTorr of oxygen pressure at 5 W for 30 s removed carbon without showing any change in morphology (Figure 59 bottom left). At higher plasma intensities (75 Torr, 150 W), the oxygen plasma created a rough surface with 3D features (Figure 59 right).

XPS studies revealed extra BaO on the surface post-exposure to high oxygen plasma intensities (Figure 60). Introducing a material with a lower dielectric constant and modifying the surface chemistry would reduce the piezoresponse of the film. While the oxygen plasma was not useful for sample cleaning before PFM measurement, it did open another path to modifying surfaces for growth or creating nanostructures in alternate ways.

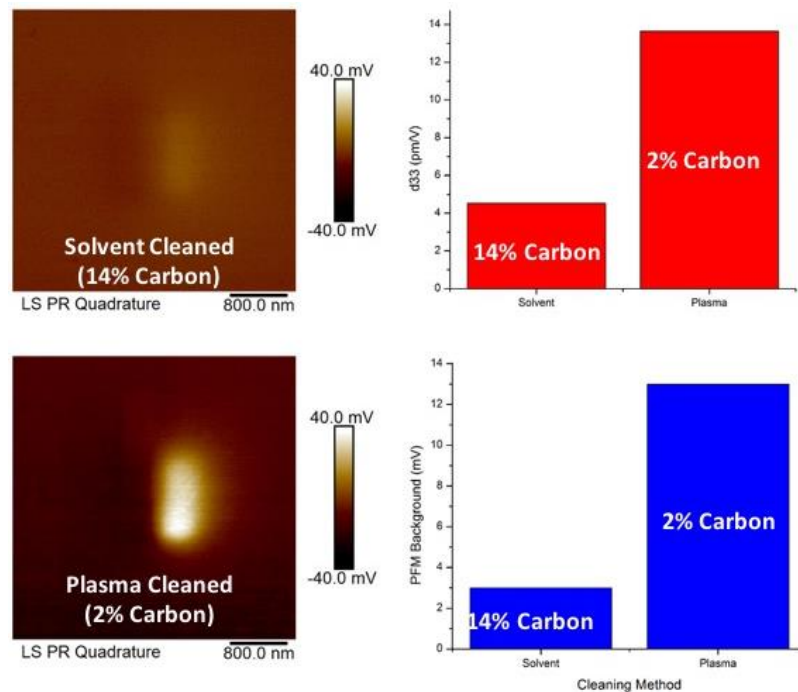


**Figure 60.** Piezoresponse of solvent cleaned (TL) vs plasma cleaned (BL). The  $d_{33}$  (TR) changes primarily because of surface charge background (BR).

The piezoresponse of the optimally plasma cleaned sample was measured and both the piezoresponse and the background were found to be high. Using the solvent cleaning method, the carbon was found to be about 14% and  $d_{33}$  around 4 pm/V. Using the oxygen plasma cleaner, the carbon was reduced to 2% and the  $d_{33}$  increased to ~13 pm/V.

The background of the PFM measurement increased proportionally with the  $d_{33}$ . The background measurement is an indication of non-local charge on the surface. A capacitive force between the cantilever and a charged surface will produce a piezoresponse since it oscillates at the same frequency of the applied voltage. It was concluded that the oxygen plasma cleaning put charge on the surface, most likely in the form of atomic oxygen. The only non-destructive way of removing carbon without modifying the chemistry of the surface was to heat in UHV and measure PFM under the same conditions.

#### 4.3.2 Surface Charge

Local charge contributes to a larger piezoresponse than just the piezoresponse coming from material expansion and contraction [163], [171], [172]. The electrostatic contribution can be reduced by using a stiff probe ( $k > 1$  N/m). Surface charge is necessary to stabilize domains and will always be present. However, for comparing piezoelectric coefficients, cleaning helps to keep the typical charged molecules, such as  $\text{CO}_2$ , reduced to the same level and reduce the variance local charge could have on the measured piezoresponse.

#### 4.4 Tip Force

A change in tip force resulted in up to four times the change in  $d_{33}$  (Figure 61). Since a cantilever can be considered a spring, a deflection set point controls the amount of interaction (i.e. force) to interact with the sample to image the surface. In the Bruker D3100 Nanoscope V

(Bruker, Tuscon, AZ), the set point is controlled by a laser that bounces down a tube and back in to a photodiode. A laser beam is bounced off of two mirrors, one fixed, and one adjustable by a screw. In typical AFM measurements, there can be variation in the set point due to thermal or mechanical drift of the mirror that aligns the laser set point on the photodiode. For normal morphological measurements in AFM, a change in setpoint from 0.1 to 0.09 mV is negligible and has no bearing on the measurement. However, in a PFM measurement, the detection of movement by the photodiode is picometers. In Figure 61, the relationship between tip force and  $d_{33}$  was shown to be inversely related. A change in force was significant as shown in the figure where a 10% reduction in setpoint led to a significantly higher piezoresponse.

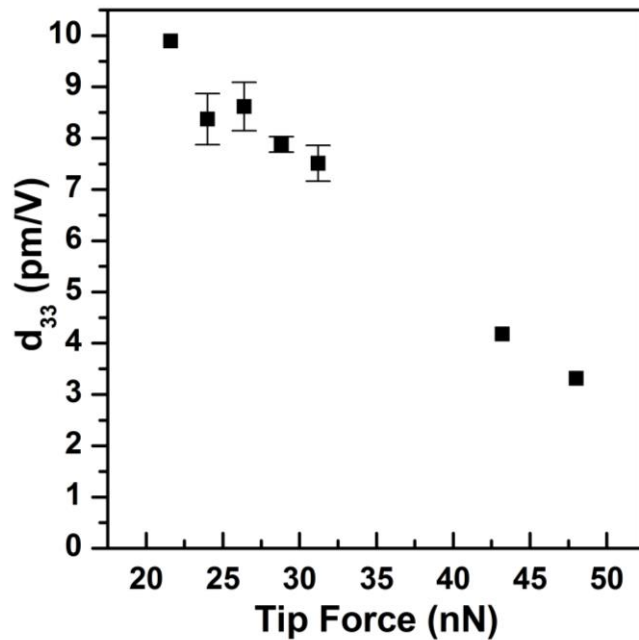


**Figure 61.** Effect of set point (tip force) on piezoelectric coefficient.

While Figure 61 represents changes in set point observed post measurement, an experiment was carried out to show the changes in piezoresponse during measurement to remove other measurement factors. During the measurement, the tip force was changed by altering the set point from 110 to 90 to 70 mV. The piezoresponse changed with tip force. The  $d_{33}$  increased

by ~18% for a ~22% decrease in tip force. A 0.01-0.02 V change in the set point is common in the Bruker D3100 Nanoscope V PFM and can result in  $d_{33}$  changes.

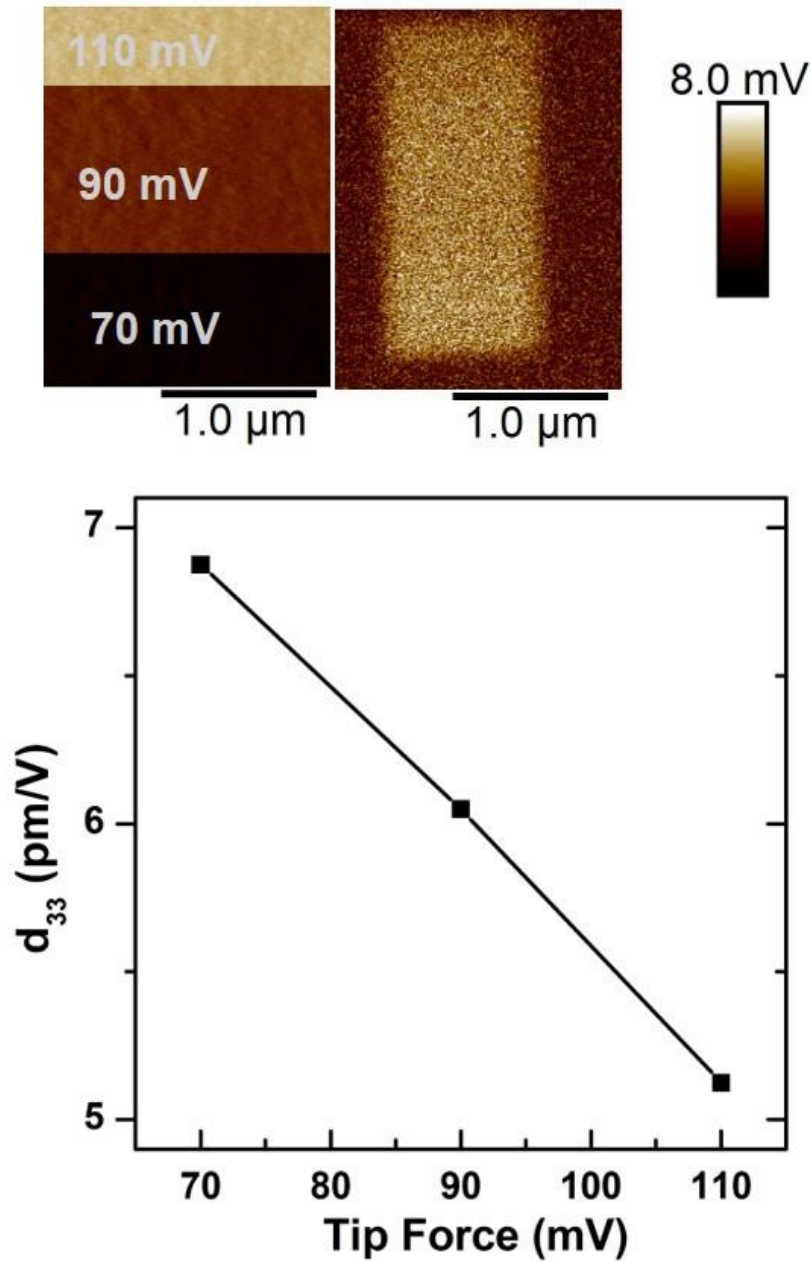


**Figure 62.** Changes in set point (top left) result in changes in piezoresponse (top right).  $d_{33}$  relationship with tip force (bottom).

To reduce variation, the set point was checked after every measurement to ensure there was no drift. If a change in the set point was observed, the data was discarded and not used.



When a constant set point or force on the sample was maintained, the variation was reduced to 10 to 20% as shown in Figure 63.

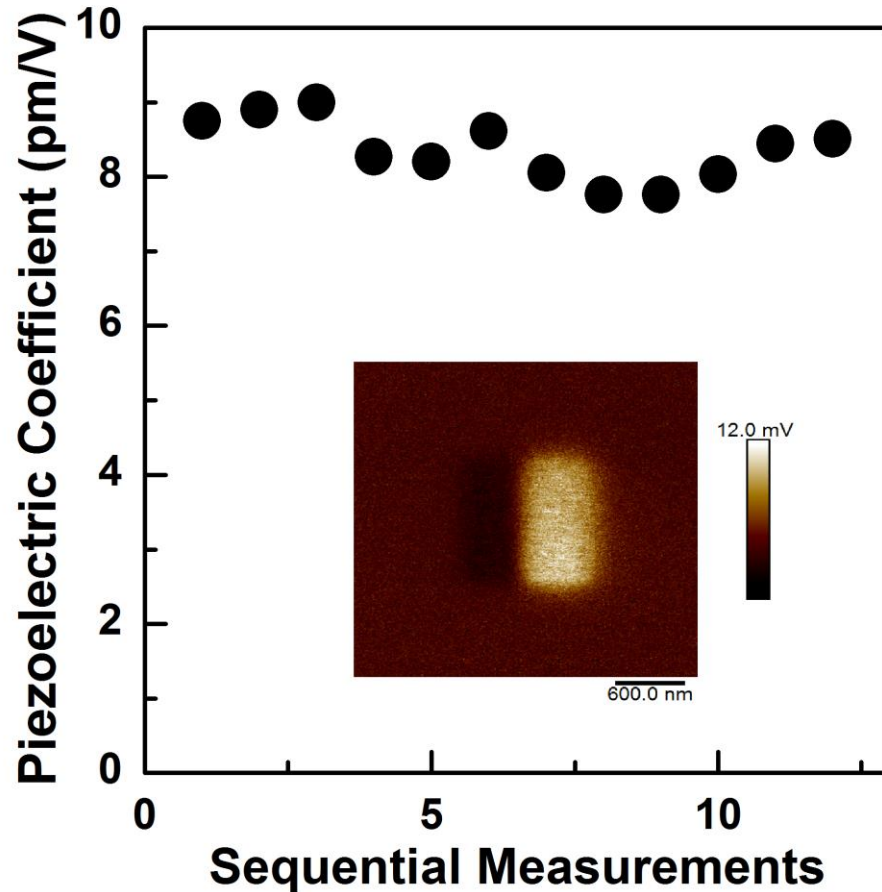


**Figure 63.** Less than 20% variation in piezoelectric coefficient when tip force was held constant.

The tip force was important because of the piezoelectric effect. When force is put upon a ferroelectric, a charge is generated. Also, tip changes can affect how that force impacts the sample, which will be discussed next.

#### 4.5 Probe Effects

It was found that probes could change the value of the piezoelectric coefficient by more than 25%. Figure 64 shows the piezoelectric coefficient ( $d_{33}$ ) for a single BTO film measured by



three different probes with multiple measurements. While some probes yielded similar values, some substantially deviated.

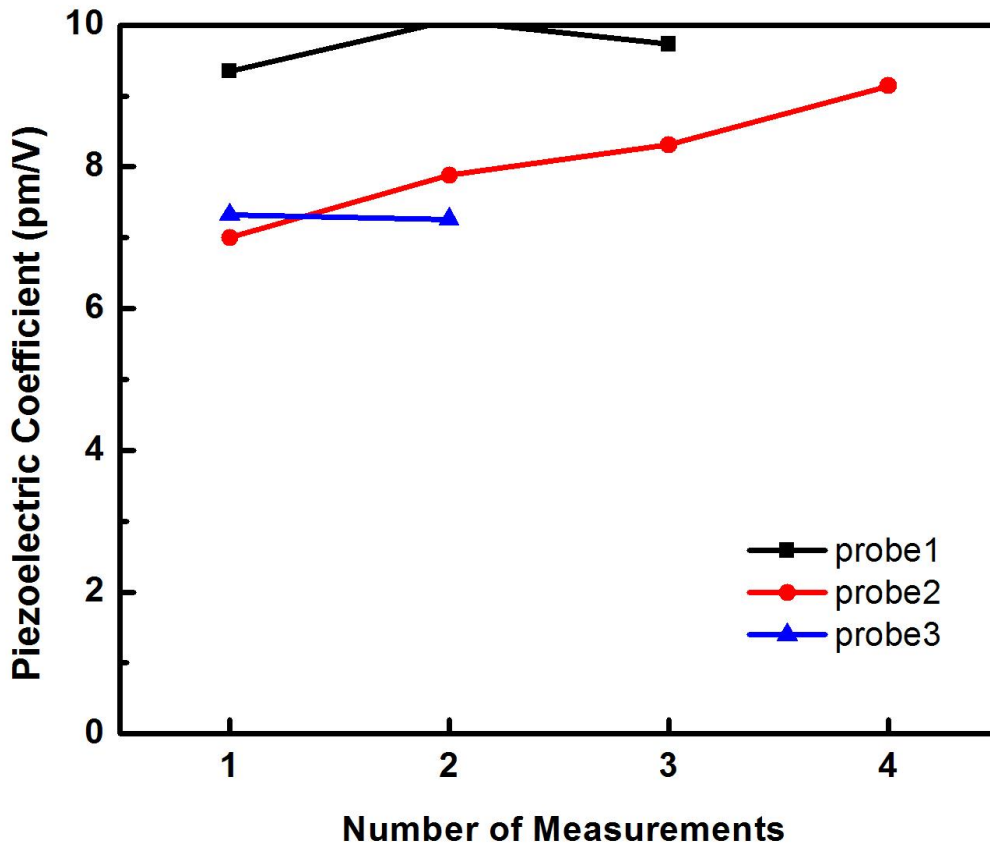


**Figure 64.** Change in piezoelectric coefficient with change in probe.

Probes change for many reasons. The shape can differ from probe to probe in the probe manufacturing process as illustrated by the initial measurements of probe 1 and probe 2 differing. It was found that engaging the probe could change the  $d_{33}$  value, which may have been related to changes in tip force. Using the tip changed the probe shape as the metal coating was removed by wear (Figure 65). Engaging the probe can also deform the tip shape, as more force is often required to find the surface before scanning. In Figure 65, the initial piezoelectric measurement is different for each engagement. The change in metal coating could also impact how uniformly the electric fields could be applied.

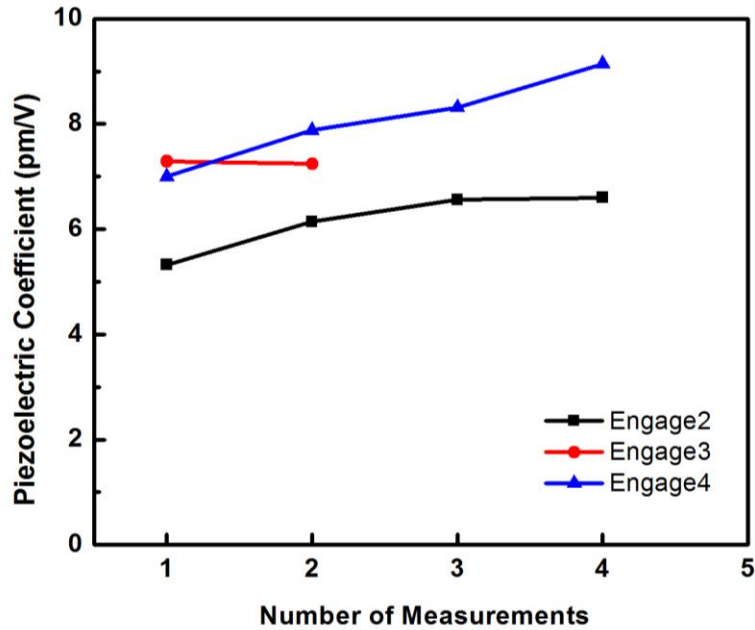


**Figure 65.** Probe engagement changed the  $d_{33}$  value.

On one sample, a dramatic difference was found in the  $d_{33}$  when different probes were used. Tip shape differences were imaged using a SEM as shown in Figure 66. It was obvious that the tip shape was very different which could account for some of the variation between the measurements.

One strategy to reduce variation was to use one probe for comparing samples to each other. This reduced the probe effect but the finite lifetime and multiple measurements per sample limited how many samples could be compared. As seen in Figure 64, large variations in the piezoelectric coefficient can exist when different probes are used.

While using one probe can remove the variation due to tip shape, changes during the probe lifetime could definitely also introduce some variation. In order to maximize the lifetime of one probe, the area that was poled was reduced. Beyond that, the only way to make semi-quantitative comparisons because all of these factors was to make many measurements with many probes and obtain an average and standard deviation for each sample. It was found that a

10 to 20% standard deviation for all measurements could be achieved if at least three probes and with 10 different measurements were taken for each sample.

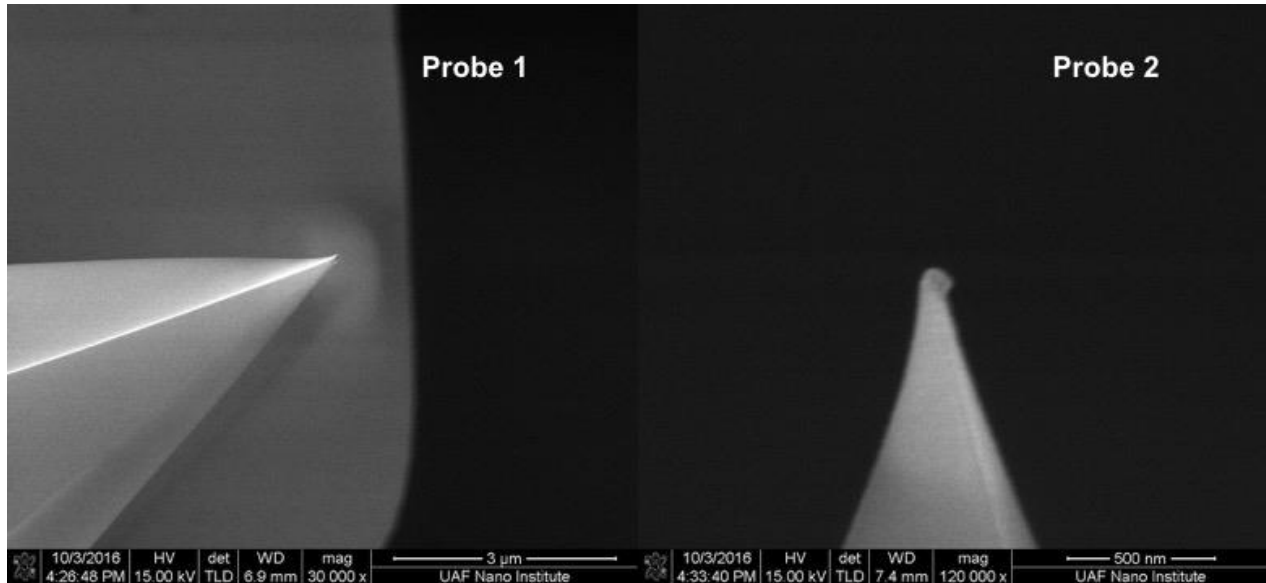


**Figure 66.** SEM images show difference in shape between two probes.

It was also discovered that the  $d_{33}$  value depended upon the speed of the probe during measurement. While this was an easy factor to control, it was necessary to pay attention if scan rates or poled sizes were changed.

#### 4.6 Comparing Growths using Quantitative Piezoforce Microscopy

A procedure was developed to measure piezoelectric coefficients from piezoforce microscopy technique for semi-quantitative comparison between barium titanate thin films. The standard deviation of the  $d_{33}$  parameter was less than 20% when this procedure was followed. There were many factors that contributed to this variation that were difficult to control, including surface chemistry, tip force, and probe shape. In order to minimize their effect, more than 30 measurements that included multiple locations and probes were used to determine the  $d_{33}$  to

ensure accuracy in comparison. It was also discovered that there were important measurement effects that could reduce variation, including solvent cleaning the surface to control the amount of carbon on the surface and ensuring the tip force was not changed.

The QPFM procedure allowed the ferroelectric properties of the samples to be measured and any differences based on growth approach detected. If any additional phases began to form, a decrease in the piezoresponse from the sample was expected.

## Chapter 5: Results & Discussion

This dissertation reports on the self-assembly of barium titanate thin films. It was demonstrated that co-deposition of titanium with excess barium produced stoichiometric barium titanate thin films. In order to confirm the excess barium growth condition, barium-rich and barium-poor shuttered RHEED oscillations were characterized. It was discovered that BTO films grown with excess barium-rich growth condition produced bulk values for stoichiometry, lattice parameter, and piezoelectric coefficient when the films were fully relaxed. The excess barium accumulated at the surface of those films. In contrast, it was shown that fully relaxed BTO films grown barium-poor do not produce bulk BTO properties.

### 5.1 Characterizing BTO Films under Off-stoichiometric Growth Conditions

In order to ensure barium-rich growth conditions, key features were discovered in shuttered RHEED oscillations that predict barium-rich and barium-poor growth conditions. The 40 nm BTO thin films grown with excess barium showed bulk values for stoichiometry, lattice parameter, and piezoelectric coefficient. While the barium-poor samples did not have all of the bulk BTO values. Furthermore, the BTO films grown with excess had a rougher surface than the films grown with excess titanium.

#### 5.1.1 Off-stoichiometric RHEED Oscillations

The shuttered RHEED oscillations were altered by adjusting the shutter times of barium and titanium. The shape of a single oscillation was found to be a good predictor of cation growth condition. Barium-rich RHEED oscillations were identified primarily through a two-peak feature. The titanium-rich RHEED oscillations had no peaks and curved at the close of the titanium. The changes in RHEED oscillations, denoted by the shutter time ratio ( $t_{\text{Ti}}/t_{\text{Ba}}$ ), are

summarized in Table 8 along with the resulting material properties for a series of eight 40 nm barium titanate thin films grown with parameters in Table 3. The purpose of the series of experiments was to hold the cell temperatures constant and change the shutter times to vary the growth conditions from barium-poor ( $Ti/Ba > 1$ ) to barium-rich ( $Ti/Ba < 1$ ).

In Table 8, barium-rich and titanium-rich grown BTO films are grouped. The samples with similar RHEED oscillations are grouped together. Films that showed peaks are grouped together in green, while the samples that showed a curved tail at the end are in blue. The growth condition is quantified by the ratio of the titanium-to barium-shutter time ( $t_{Ti}/t_{Ba}$ ).

**Table 8.** BaTiO<sub>3</sub> material analysis of barium rich and titanium rich thin films.

Sample	$t_{Ti}/t_{Ba}$	Ti/Ba (BC)	Ti/Ba (PC)	c (Å)	$R_q$ (nm)	$d_{33}$ (pm/V)
OG029	1.25	0.78	1.18	4.038	0.378	3.09
OG033	1.22	0.68	1.08	4.057	0.704	4.30
OG034	1.26	0.65	1.16	4.039	0.453	3.10
OG031	1.25	1.07	1.47	4.044	0.092	3.08
OG032	1.32	1.23	1.40	4.041	0.102	3.26
OG035	1.39	1.12	1.45	4.048	0.078	3.14
OG036	1.43	1.11	1.38	4.063	0.088	4.95
OG037	1.30	1.04	1.34	4.047	0.125	3.22

The surface stoichiometry of the films before ('Ti/Ba (BC)') and after ('Ti/Ba (PC)') methanol sonication are the ratios of titanium-to-barium from XPS elemental scans. The structure of the films is represented in the table by the out-of-plane lattice constant (c).  $R_q$  is the

root mean square height, which gives the surface roughness from atomic force microscopy scans.  $d_{33}$  is the piezoelectric coefficient determined from piezoforce microscopy measurements.

The samples with peaks in the RHEED oscillations were confirmed to be barium-rich. In Table 8, all of the green samples have Ti/Ba less than one, indicating more barium was deposited during growth than titanium. The shutter time ratio was lower than most of the titanium-rich samples with the exception of OG031. Changes in cation fluxes can result in different RHEED oscillation features for same shutter times.

The BTO films with curves at the open of barium and close of titanium were confirmed to be titanium-rich. In Table 8, all of the blue samples with these similar RHEED oscillation features have a Ti/Ba greater than one, indicating more titanium than barium was deposited during growth. Just as in the samples with peak features, the shutter time ratio did not predict precisely the change in Ti/Ba.

Even though barium-rich vs. barium-poor growth conditions can be identified from features in RHEED oscillations, predicting precisely the change in stoichiometry is difficult. Despite the shutter time ratios being chosen to have different strength of the peak for the three barium rich samples, the stoichiometry of the film did not change in the same way. For example, even though OG029 had nearly the same shutter time ratio of OG034, the Ti/Ba was different. This difficulty in controlling stoichiometry motivated the discovery of a self-limiting mechanism for BTO growth to automatically lock-in the stoichiometry. The self-limiting mechanism for stoichiometric growth of BTO will be discussed more in this chapter.

RHEED oscillation peak features for barium-rich and titanium-rich are compared in Figure 67. The dwell time after the closing of the barium and titanium shutters was for observing how the surface changed with the excess cations on the surface. In Figure 67A, the peak during the barium shutter open represents that more than a complete layer of BaO had been formed.

RHEED intensity decreases when the surface roughness increases. Furthermore, the RHEED intensity was coming from barium oxide on top of barium oxide, which has a different lattice constant than BTO. During the dwell time after the barium shutter closed, the intensity increased indicating that the surface with excess barium was rearranging. When the titanium shutter opened, additional surface rearrangement occurred since titanium and some barium were on the same surface which is not desirable for a stable BTO structure. This increase in intensity could have been the titanium and barium forming BTO unit cells on the surface. While the roughness would have still been increasing, the restoration of pure BTO on the surface could have increased the intensity.

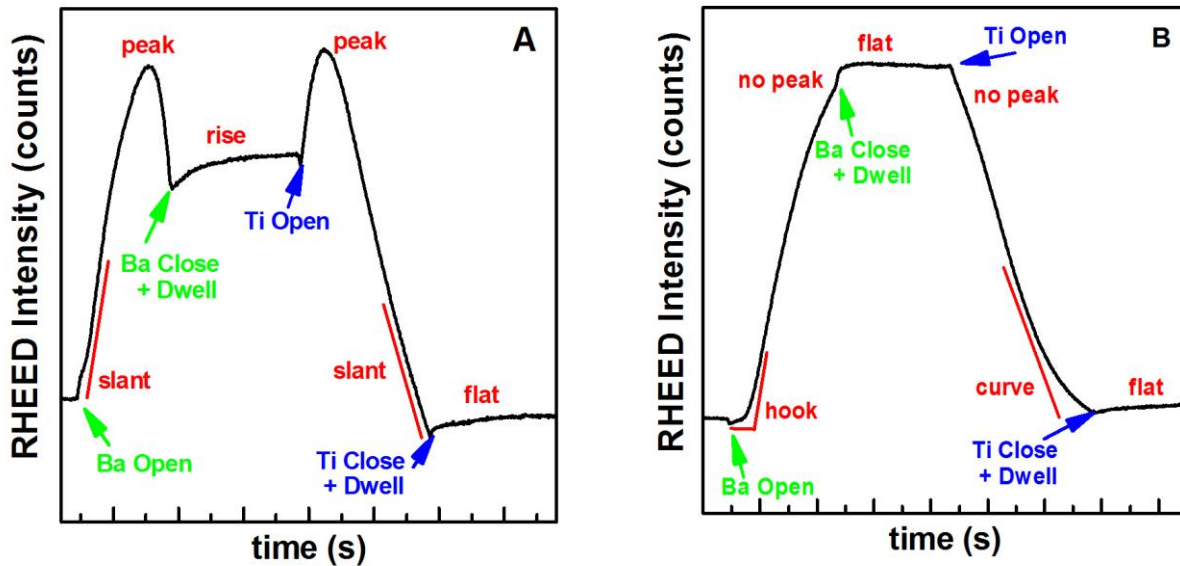


**Figure 67.** Comparing barium-rich (A) and barium-poor RHEED oscillations (B).

The titanium-rich RHEED oscillations were characterized by the curves at the opening of barium and closing of titanium as shown in Figure 67B. The curve at the end of the titanium deposition showed excess titanium accumulating on the  $\text{TiO}_2$  surface. The curve represented a change in the surface roughening process. At the opening of the barium shutter, a curve in the



intensity was also present representing some sort of surface rearrangement before a new barium oxide layer formed on the surface. There were no peaks and the intensity during the dwell time after the barium was shut showed almost no change in intensity.

In addition to the characterization of the RHEED oscillations, the morphology of the barium rich and barium poor samples were unique. As shown in Figure 68, the barium-rich samples had a higher surface roughness than the titanium-rich samples. All of the titanium-rich samples have a  $R_q \sim 0.1$  nm. On the other hand, the barium-rich samples had a surface roughness at least four times greater. Also, as seen previously in Figure 47, three dimensional features appeared on the barium-rich films.

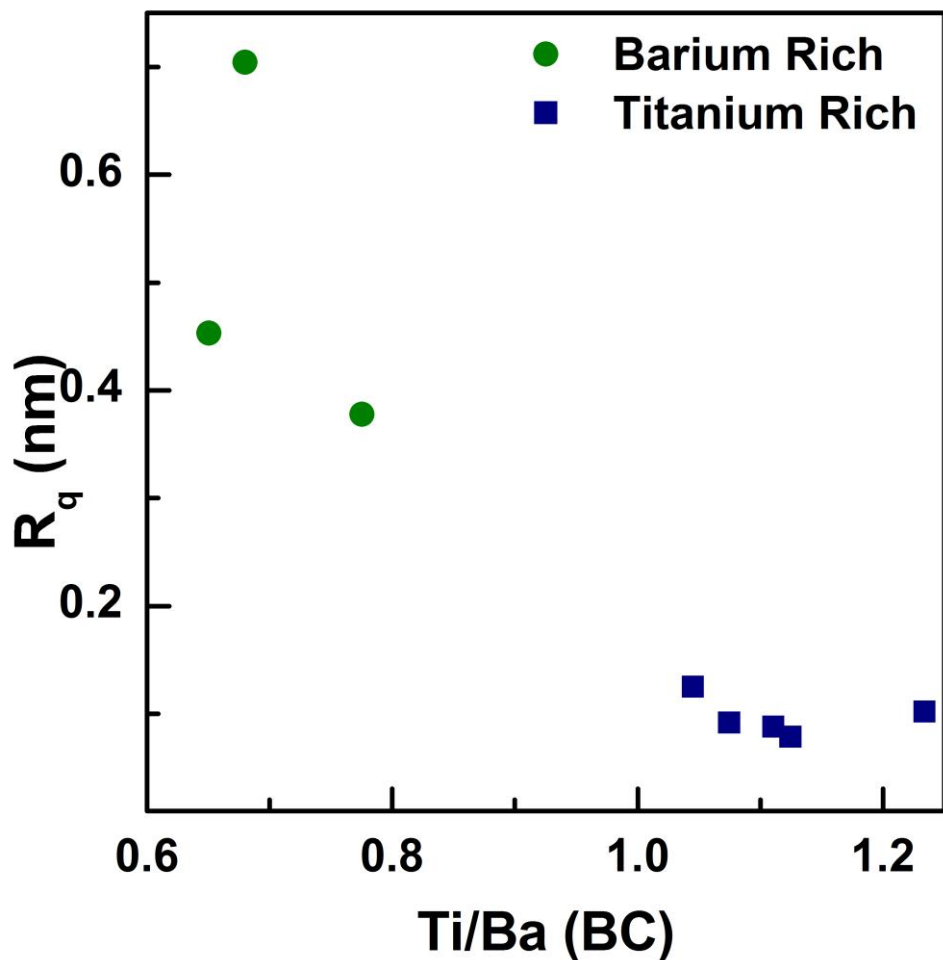


**Figure 68.** Surface roughness as function of stoichiometry.

### 5.1.2 Structure and Stoichiometry of BTO Films

BTO films grown with excess barium showed bulk BTO lattice parameters and surface stoichiometries. The incorporation of excess barium was different than the incorporation of the excess titanium into the BTO films. The BTO films with excess titanium did not have both bulk lattice parameters and surface stoichiometries.

Initially, there was a discrepancy between the surface stoichiometry and the lattice parameter, which was an indirect measurement of the whole film. As shown in Figure 69, two of the barium-rich samples had bulk BTO lattice parameters, but their surface stoichiometry was about 0.5 away from bulk BTO. As a note, the one barium rich sample (OG033) that had a lattice parameter of 4.057 Å had a different starting RHEED pattern indicating the surface was different and would have led to a difference in strain and, thus, lattice parameter.

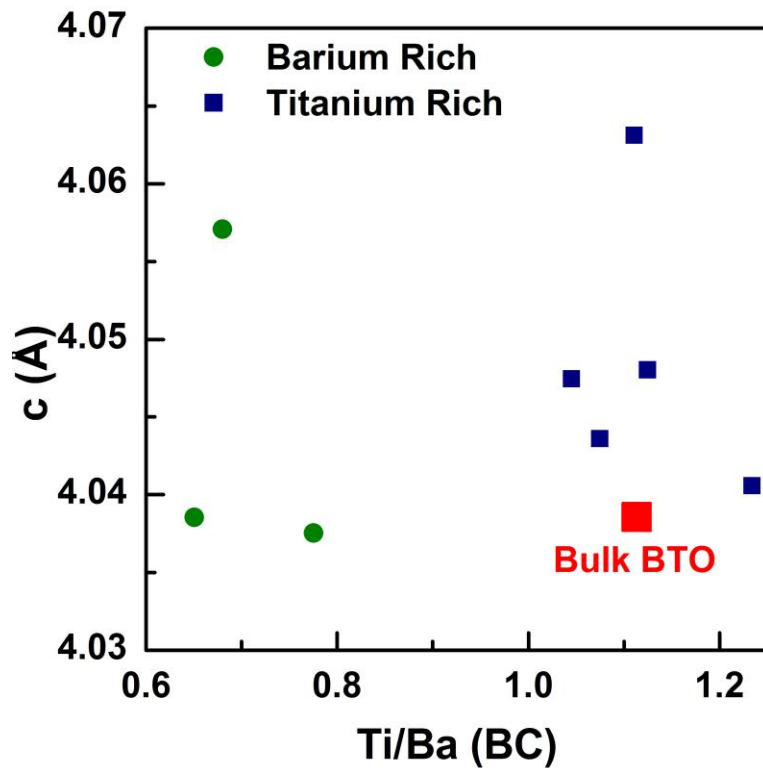


**Figure 69.** Out-of-plane lattice parameter based on surface stoichiometry.

In contrast, the titanium-rich samples had the bulk BTO surface stoichiometry but most did not have the bulk BTO lattice parameter. The relationship between Ti/Ba and  $c$  is not mapped in the literature due to the fact that BaO-TiO<sub>2</sub> do not alloy. So there is no known structure change with stoichiometry. This is primarily due to the perovskite formation rules that disallow barium and titanium from sitting in each other's sites in the ABO<sub>3</sub> perovskite structure. Instead, other phase or solid solutions form, making it difficult to predict what will happen to the structure.

The surface stoichiometries changed when sonicated in methanol. A barium oxide layer forms at the surface of BTO [104], which is soluble in methanol. It was interesting that the barium-rich samples had the same surface stoichiometry as bulk BTO after the methanol cleaning as shown in Figure 70. While the excess titanium samples had higher Ti/Ba than bulk BTO.

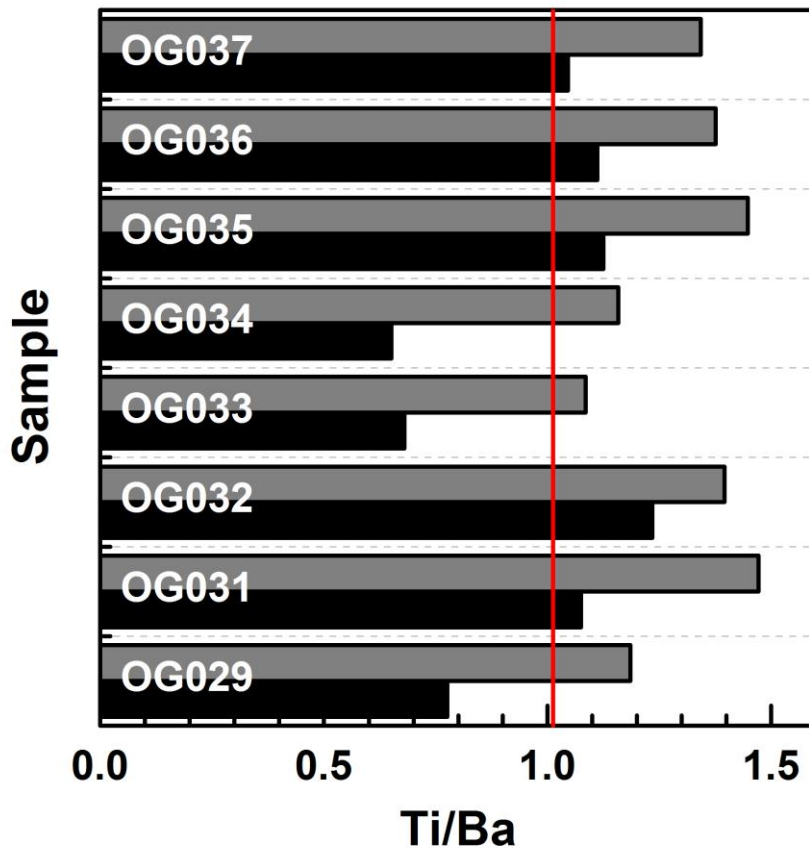
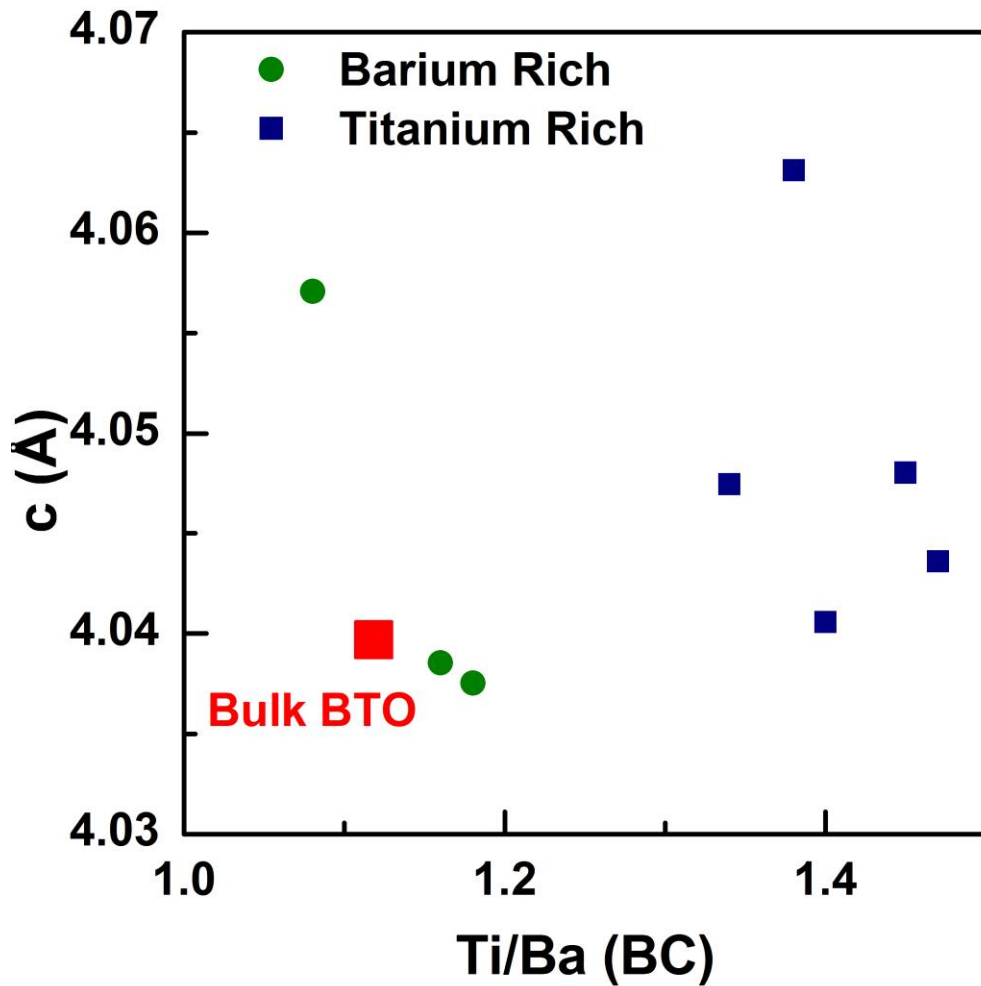


Figure 70. Stoichiometry change after surface cleaning.

After methanol cleaning, both the surface stoichiometry and lattice parameter for barium-rich samples showed bulk BTO properties (Figure 71). The excess barium did not incorporate into the film but rather accumulated at the surface and could be removed with methanol. The titanium-rich samples did not have the bulk BTO surface stoichiometry even though one of the samples had a bulk BTO lattice parameter.



**Figure 71.** Lattice parameter and stoichiometry (Ti/Ba) have bulk BTO values when grown in barium-rich condition.

The barium-rich growth condition produced BTO films with bulk BTO surface stoichiometries and lattice parameters. The excess BaO accumulated at the surface. The titanium-

rich samples showed that the excess titanium incorporated into the film changing both the structure and surface stoichiometry.

### 5.1.3 Ferroelectric properties of BTO films

The BTO films grown with excess barium showed bulk BTO piezoelectric coefficients. The titanium-rich samples with small lattice parameter deviation from bulk BTO also showed corresponding piezoelectric coefficients. This indicated that the excess titanium incorporated into the film did not change the piezoelectric response. The two samples with larger lattice parameter had a larger piezoelectric coefficient (Figure 72 top). These two samples were grown with the most extreme shutter time ratios. Larger out-of-plane lattice constants allowed for larger polarization. The excess cations probably changed the strain applied to the film thus creating a larger piezoelectric coefficient.

The invariance of the piezoelectric coefficients with titanium excess was surprising (Figure 72 bottom). Except for the one sample with a larger lattice constant, the samples had identical  $d_{33}$  values. Understanding how titanium incorporates and why  $d_{33}$  doesn't change are open questions. The BaO-TiO<sub>2</sub> phase diagram does predict a small solubility range for excess TiO<sub>2</sub>. However, outside of this range, a BTO solid solution forms with BaTi<sub>2</sub>O<sub>5</sub>. The substrate acts as a template that selects the BTO phase due to similarity in in-plane lattice constant; BTO has a 3.99 Å, which is closer to STO at 3.905 Å than any of the other phases as seen in Table 1. Excess titanium may incorporate as interstitial or Schottky defects [71], [164].

In order to ensure bulk BTO stoichiometry, structure, and piezoelectric properties, BTO films should be grown under excess barium. The amount of excess barium that can be provided and still obtain stoichiometric BTO remains an open question for further investigation. Excess titanium does not guarantee bulk BTO properties.

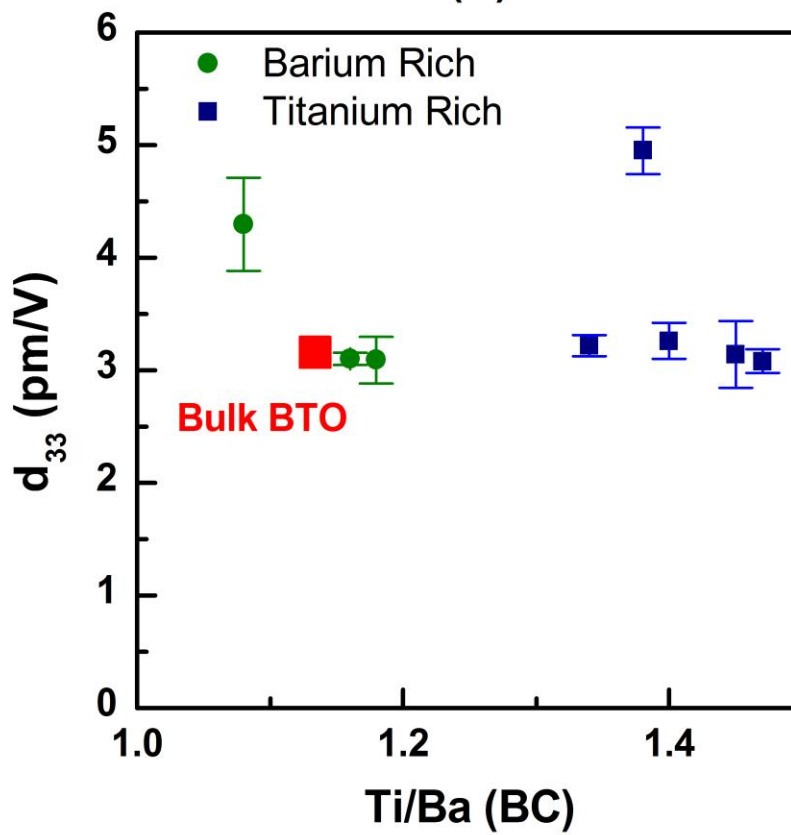
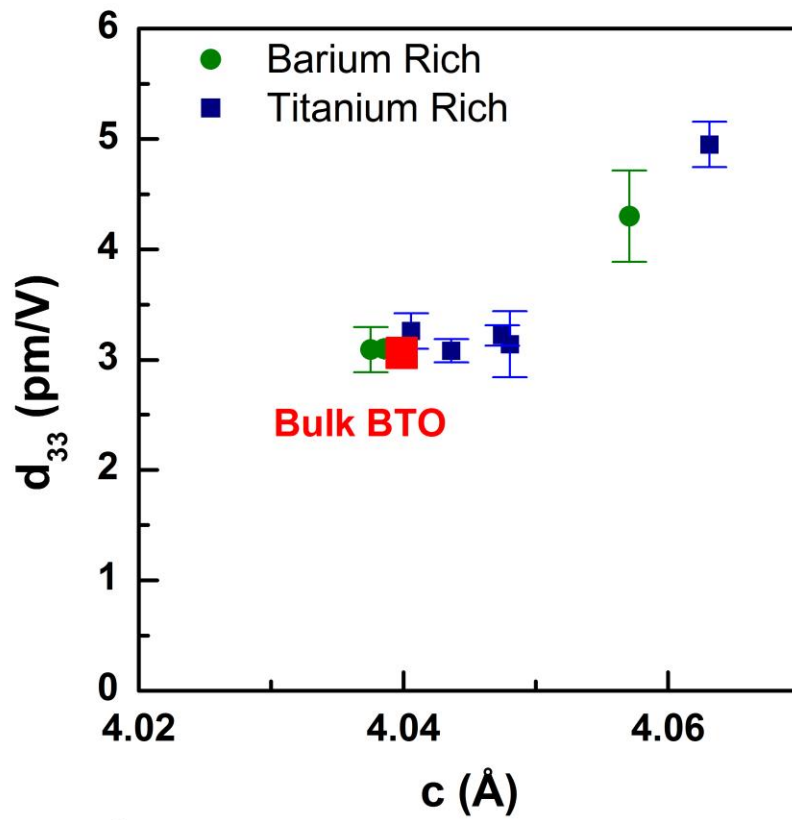
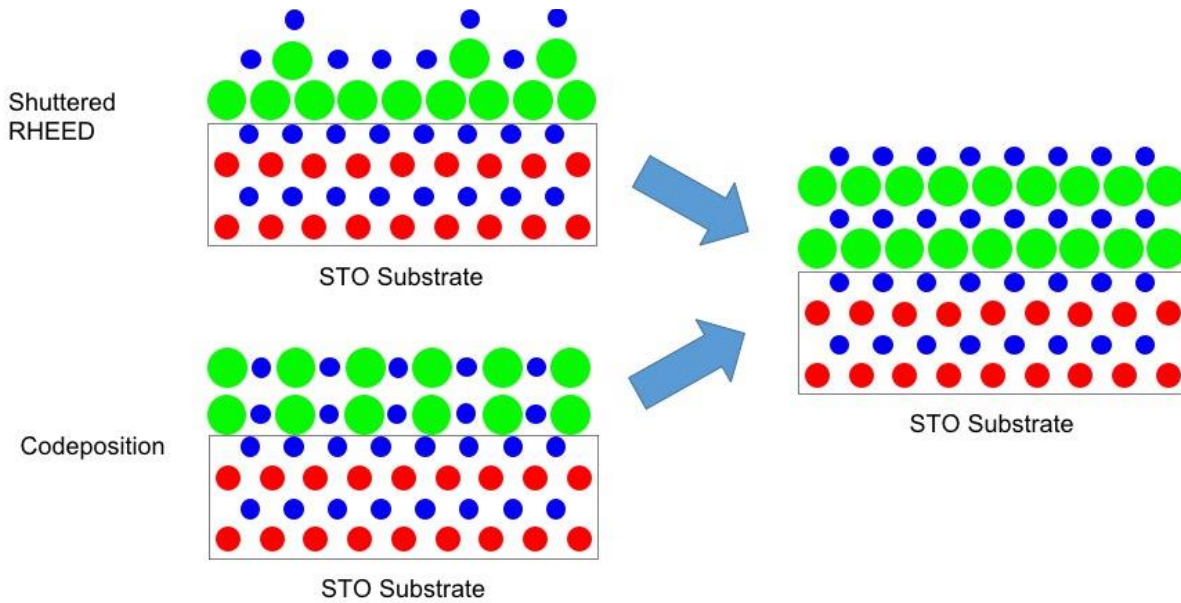


Figure 72. Piezoelectric coefficient as function of  $c$  (above) and Ti/Ba (below).

## 5.2 Self-Assembly of BTO films

With the ability to predict barium-rich growth conditions using shuttered RHEED oscillation, the use of excess barium in codeposition to limit the stoichiometry is reported. In shuttered RHEED, some titanium was deposited on the same layer as the excess barium (Figure 73). It was discovered that the barium oxide and titanium dioxide arranged into BTO (self-assembly). Codeposition extended this barium titanium intermixing in the same layer to the maximum. It was demonstrated that excess barium not only self-limited the stoichiometry but allowed for BTO to self-assemble into the correct crystal structure.



**Figure 73.** Self-assembly of barium titanate.

A novel growth approach is reported that allows for the self-assembly of barium titanate. Excess barium provided during codeposition yielded stoichiometric BTO films. The codeposited films were compared with shuttered RHEED and found to produce BTO films with nearly identical properties. In both cases, the excess barium accumulated at the surface that was subsequently removed with methanol sonication.

For this investigation, a Riber 32 molecular beam epitaxy chamber was used to grow barium titanate thin films on SrTiO<sub>3</sub> (doped with Nb 0.5 wt%) under barium-rich growth conditions using both CD and SR. The substrate was heated using a SiC filament with a constant 14.5 A and a starting growth temperature of 650 °C determined by blackbody radiation using a kSA BandiT. Atomic oxygen was supplied using an oxygen plasma with a partial pressure of  $1.5 \times 10^{-5}$  Torr. A calibration sample was used to determine the cation cell temperatures ( $T_{\text{Ba}} = 596$  °C,  $T_{\text{Ti}} = 1838$  °C), so that the barium and titanium shutter times would be equal. This improved the comparison between SR and CD so that the excess would be distributed evenly throughout the growth and maximize the intermixing of barium and titanium on the surface. RHEED was used to monitor the surface in the (110) direction and the x2 reconstruction was avoided to ensure the excess barium was less than 20% [105].

In order to compare samples grown with both CD and SR, the differences between the two growth approaches were considered. In CD, the temperature of the crystal surface was constant since both shutters were open the entire time, whereas in SR, the opening and closing of the titanium cell provided a change in the amount of infrared radiation hitting the surface [173]. The shuttering of the titanium cell raised and lowered the temperature of the surface. Furthermore, in SR the excess barium was exposed to this change in surface temperature. In order to study the effect of surface temperature change in CD samples, samples were grown with a dwell time in-between layers. To examine those effects, 20 and 60 s dwell times were used after each barium shutter closing and titanium shutter closing in the SR growths to see how the cation stoichiometry was affected. For comparison with the 20 s SR sample, a CD sample with 40 s dwell time was grown after a simultaneous closing of the barium and titanium shutters. This way, the dwell time per complete BTO layer was equivalent and the rearrangement on the surface could be compared. To ensure barium-rich growth conditions, the first sample of the pair



was always grown using SR. A total of five samples were grown: SR 0 s, CD 0 s, SR 20 s, CD 20 s and SR 60 s.

Twenty layers (~5 nm) were chosen so that the stoichiometry of the entire film could be examined by XPS and XRD. A PHI Versaprobe 5000 XPS (Physical Electronics, Chanhassen, MN) with monochromated Al  $k\alpha$  x-rays was used to perform survey and elemental scans of Ba 3d<sub>5/2</sub>, Ti 2p, O 1s, C 1s and Sr 3d. In order to understand where the excess barium existed in the films, elemental scans at 45° and 15° were used to evaluate whether the excess barium was incorporated through the film or at the surface. Methanol sonication was used to remove carbon and BaO from the surface of samples and involved 15 minutes of the sample being ultra-sonicated in methanol. To complement XPS, 2 $\theta$ - $\omega$  curves of (002) plane were acquired using a Malvern Panalytical Materials Research Diffractometer (Malvern Panalytical, Westborough, MA) with Cu  $k\alpha$  x-rays to assess if the excess barium incorporated into the films and changed the lattice parameter.

Piezoforce microscopy (PFM) was used to determine the ferroelectric properties of the BTO films. In order to compare the impact of each growth approach, the piezoelectric coefficient ( $d_{33}$ ) was extracted for comparison. The quantitative PFM technique was described originally by Soerogl et al. [156], [174] and implemented recently by Yu et al. [175]. Using a Bruker D3100 Nanoscope V (Bruker, Tuscon, AZ) with Pt-coated silicon probes with  $k = 3$  N/m, a 1  $\mu\text{m}$  x 1  $\mu\text{m}$  square was poled, half with +7V and half with -3V to create 180° domains. The piezoelectric coefficient was then calculated from the difference in out of phase piezoresponse signals from the 180° domains. More than 30 measurements were made on each sample post solvent cleaning to ensure an accurate  $d_{33}$  value of the sample. QPFM measurements were made before cleaning to observe the effect of the excess barium oxide found on the surface. It was found that the excess barium oxide and carbon both reduced the  $d_{33}$  values.

### 5.2.1 Barium-Rich Co-Deposition RHEED Oscillations

Growing the SR sample first and observing the RHEED oscillations ensured a barium-rich growth condition when grown by co-deposition. A double-peak feature [118] was observed in the barium-rich SR growths similar to those observed in strontium titanate with excess strontium. This similarity provided further support that the growth condition used was under a barium-rich condition. All the films grown by SR with those double peaks were confirmed to have excess barium ( $Ti/Ba < 1$ ). Comparing the SR and CD RHEED oscillations gave evidence for surface rearrangement (Figure 74).

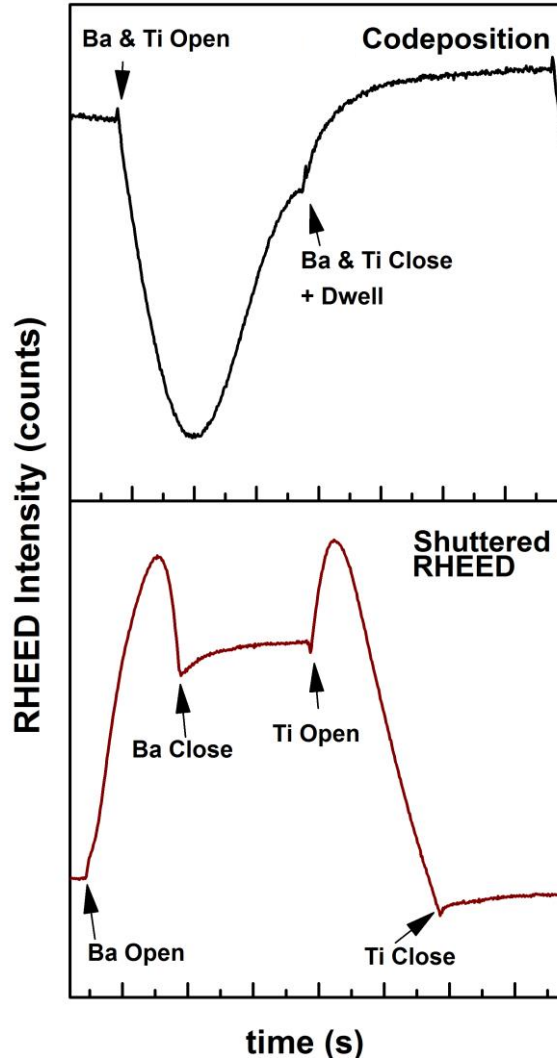


**Figure 74.** Barium-rich oscillations co-deposition (top) shuttered RHEED (bottom).

RHEED intensities increased for CD during dwell time and SR at the opening of the titanium (Figure 74). In the SR, the first peak occurred after a complete layer of BaO formed and the excess was being deposited, increasing the surface roughness and lowering the RHEED intensity. No  $x_2$  was observed so this indicated less than 20% excess barium. After the close of the barium shutter, the increase in intensity (Figure 74 bottom) indicated that the surface rearranged, possibly the excess barium coalescing into monolayer islands. Surprisingly, the RHEED intensity went up at the opening of the titanium shutter which should have increased surface roughness and lowered the intensity. The immediate increase in intensity suggested that the titanium and barium were rearranging to form BTO. The BaO-TiO<sub>2</sub> phase diagram indicated that BaTiO<sub>3</sub> was a stable phase and that the substrate encouraged this phase since other phases would increase strain and cost energy. After this excess reacted with the excess barium, the intensity decreased as expected with increased surface roughness.

Interestingly, during the dwell time for CD (Figure 74 top) the intensity increased in a similar intensity as when the titanium opened during SR. One possible explanation for the larger increase in the CD case is the barium and titanium atoms were deposited in the same layer on the surface, and then rearranged into their respective layers. This rearrangement would restore the same crystal structure and increase the RHEED intensity.

### 5.2.2 Stoichiometry of Barium-Rich Co-Deposited BTO Films

All of the BTO films were barium-rich. The elemental scans included ~1% Sr from the substrate, indicating the stoichiometry of the whole film was being detected. The ratio of the cations (Ti/Ba) was determined using XPS elemental analysis. The barium 3d<sub>5/2</sub> peak revealed two chemical environments (Figure 75) for all films but varied in intensity depending upon growth conditions; the BaO peak at 780.5 eV was higher for codeposition than shuttered

RHEED. However, both growth methods are higher than bulk BTO. Comparing the SR and CD grown BTO films revealed insight into those differences.

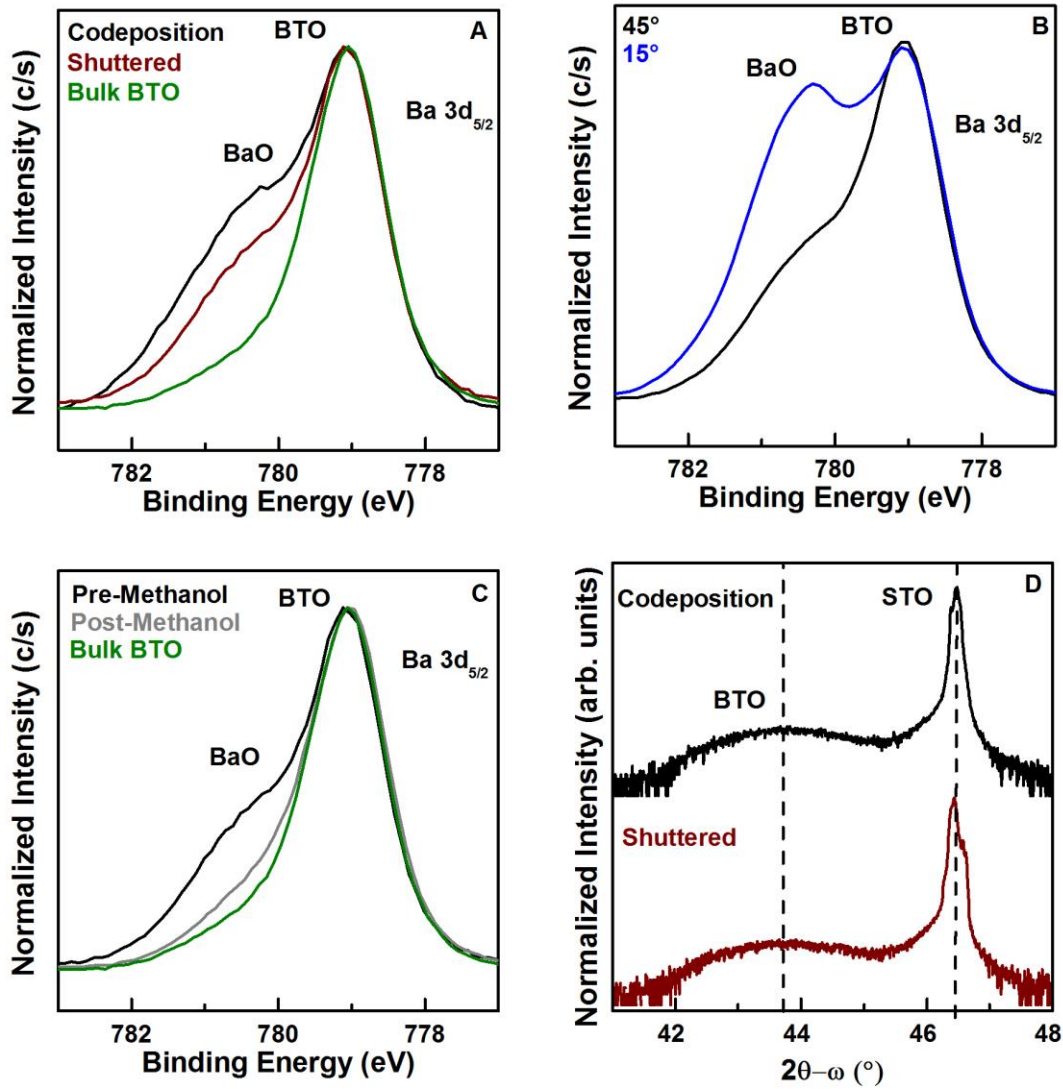


**Figure 75.** (A) Ba 3d<sub>5/2</sub> peak, (B) TOA, (C) cleaning, (D) XRD.

Analyzing the Ba 3d<sub>5/2</sub> peak revealed the differences in cation ratios belonging to the surface barium oxide layer. In both the SR and CD grown BTO films, a primary peak at 779.03 eV was attributed to BTO and a second barium peak at 780.4 eV is known as a surface barium-rich oxide layer with lower electron density than BTO [104] and will be referred to in this dissertation as BaO. The BaO peak was higher in the CD grown film than the SR (Figure 75A).

At 15° take off angle (TOA), the BaO increased, confirming the location being at the surface (Figure 75B). The excess BaO was reduced to nearly the same amount as bulk BTO (Figure 75C) using methanol sonication. The difference in cation ratio of CD to SR resulted in a thicker BaO layer forming on the surface.

Comparing the SR and CD samples with no dwell time revealed near identical lattice parameters but different cation ratios. The SR had a Ti/Ba of 0.81 while the CD was more barium-rich with a Ti/Ba of 0.59. However, both had near identical lattice parameters of 4.12 Å (Figure 75D). SR had a peak position and FWHM of 43.91° and 2.53°, respectively, while the CD had 43.86° and 2.37°.

Following methanol sonication to remove the suspected excess barium oxide at the surface, the stoichiometry changed for SR to 1.12 and for CD to 1.13 (Figure 76). Then, the XRD and XPS agreed that the CD and SR had the same stoichiometry and lattice parameter. Furthermore, the Ti/Ba ratio of both these films matched bulk BTO (dashed line in Figure 76). The change in stoichiometry after methanol sonication confirmed that excess barium during growth accumulated on the surface as BaO. While the out-of-plane lattice parameter of those films were expanded compared to bulk BTO, both CD and SR had the same out-of-plane lattice parameter. The larger than bulk (4.04 Å) *c* parameter was expected due to the 2.2% compressive mismatch between BTO and STO:Nb (0.5 wt%) substrate. Given the change in stoichiometry after methanol cleaning and the identical XRD peak positions for CD and SR samples, the conclusion was that the excess barium accumulated at the surface, and that both SR and CD growth approaches produced stoichiometric BTO.

With this in mind, all barium-rich samples (Figure 76A) were sonicated in methanol to remove excess barium oxide on the surface and found to have Ti/Ba ~ 1.1 (Figure 76B). The stoichiometry self-limited independent of shuttered RHEED, codeposition, dwell time, thickness,

and amount of excess barium provided. All of the 5 nm samples confirmed the excess did not incorporate into the film but rather rose to the surface, since the stoichiometry of the whole film was equal to bulk after methanol cleaning. The co-deposited 5 nm thick samples grown in the barium rich regime proved that stoichiometric barium titanate self-assembled and limited the stoichiometry. It is believed that since the barium atom is large, it could only sit on the A-site. As a result, when excess barium was provided both barium and titanium would sit in their respective sites.

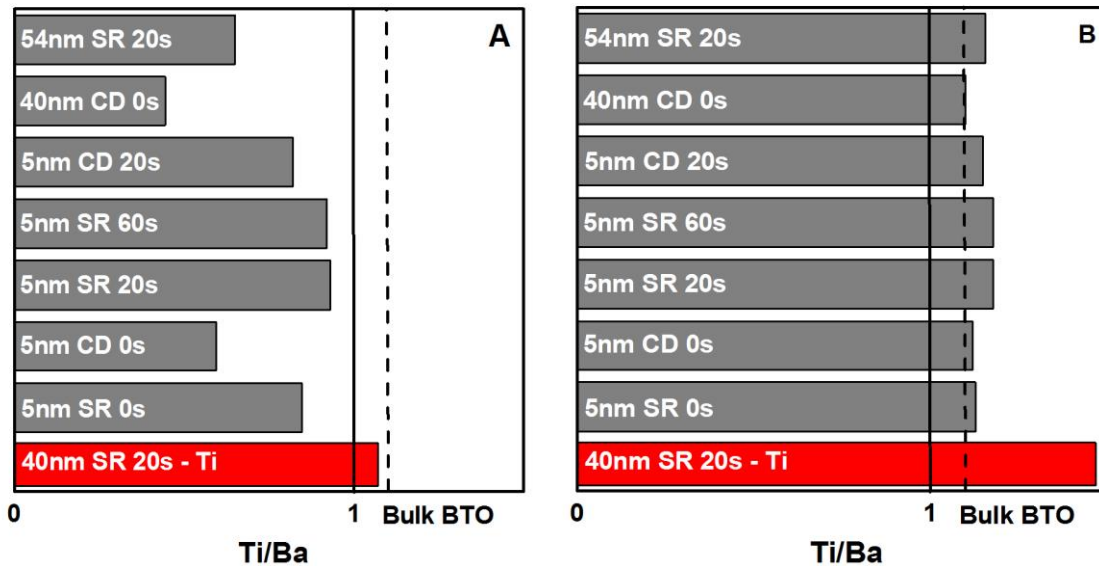


**Figure 76.** Piezoelectric Stoichiometry before (A) and after methanol sonication (B).

On the other hand, the 40 nm barium-poor SR sample had an initial stoichiometry of 1.08 but after methanol sonication, the stoichiometry did not self-limit and was found to have a Ti/Ba of 1.47. As seen in Figure 75A & C, even stoichiometric bulk BTO had a surface BaO layer as reported in literature [146]. Even though there are fewer barium atoms, the surface layer still prefers to form a BaO layer. The XPS from a barium-poor sample showed near identical BaO intensities as compared to bulk BTO. When this BaO layer was reduced, the excess titanium that incorporated into the film during growth was revealed with a greater than bulk BTO Ti/Ba ratio.

Both CD samples had a higher Ti/Ba than the corresponding SR with the same dwell time. For the 0 s samples, CD grown BTO film had a Ti/Ba 0.23 less than the SR grown BTO film. It was also observed that for the 20 s dwell time, the CD had a Ti/Ba of 0.82 compared to the SR with 0.91. The lower Ti/Ba for the CD samples indicated that the surface temperature changes had a significant impact on reducing the excess barium when it had a longer time on the surface. Thicker films grown with CD vs SR revealed this same trend. A 40 nm CD 0 s BTO film showed a Ti/Ba of 0.59 while a 54 nm SR 20 s showed Ti/Ba 0.82. Yet, after methanol sonication those films also showed bulk BTO stoichiometries.

### 5.2.3 Ferroelectric Properties of Self-Assembled BTO films

Although this data supported the conclusion that co-deposition and shuttered RHEED led to growth of similar stoichiometric material, it did not confirm similar ferroelectric properties. As a result, both growth approaches were compared by examining the effect of the two growth modes on their ferroelectric properties. To do this, all films were compared by measuring the piezoelectric coefficient ( $d_{33}$ ) value using piezoforce microscopy (PFM). Both SR and CD films showed the same magnitude of response, or value for  $d_{33}$ , using PFM as long as they had effectively equivalent thicknesses (Figure 77). On the other hand the  $d_{33}$  value was smaller for the thin samples as compared to the thicker samples.

While a larger polarization was expected from the fact that  $\text{BaTiO}_3$  is more strained and elongates the unit cell in the z-direction [80], the substrate had a larger clamping effect for the thinner samples. BTO has +2.2% mismatch with respect to STO:Nb, starts to relax at 2 nm [176], and is fully relaxed at 10 nm thickness. The thicker films took on the bulk BTO lattice constant ( $4.04 \text{ \AA}$ ) and showed a bulk  $d_{33}$  value of  $\sim 12 \text{ pm/V}$  as measured by PFM. At 5 nm thick, the film was partially relaxed with a lattice constant of  $4.12 \text{ \AA}$  with a  $d_{33}$  of  $\sim 10 \text{ pm/V}$ . The

reduction in  $d_{33}$  had to do with a larger clamping effect in the thinner films [80]. Since PFM relies on material expansion to determine the piezoelectric coefficient, the strain from the substrate restricted the material from expanding more to reveal the larger polarization.

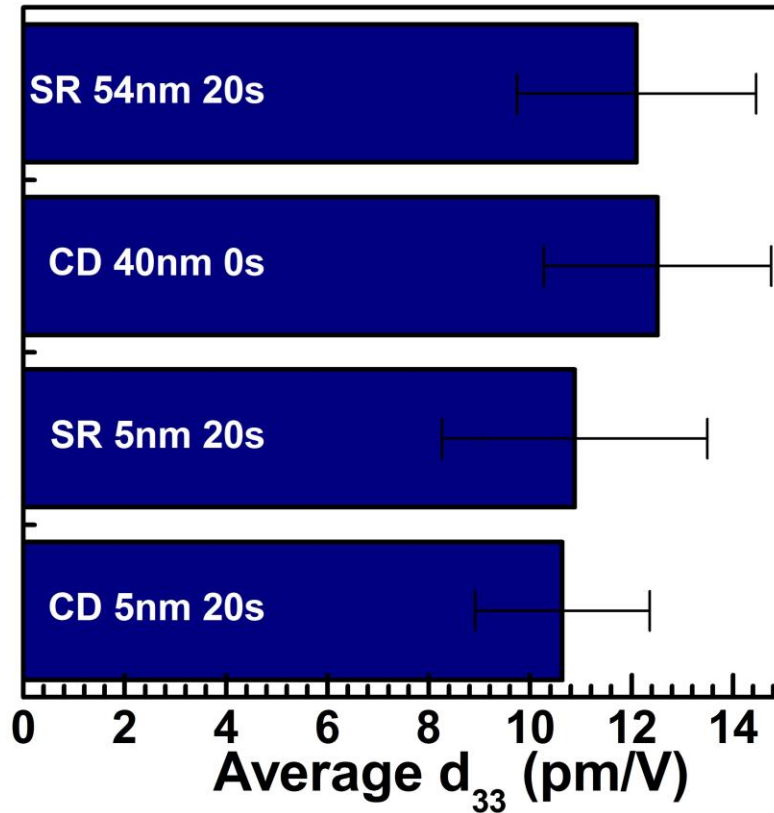


**Figure 77.** Piezoelectric coefficient comparison between growth approaches and thickness.

This research showed that barium titanate thin films self-assemble when grown by co-deposition with excess. The stoichiometry of films grown with excess barium self-limited to the stoichiometry of bulk BTO. ARXPS showed that excess barium oxide accumulated at the surface was removed with methanol. Both XPS and XRD confirmed that the remaining film was stoichiometric BTO. The ferroelectric properties of the self-assembled BTO films was equal to that of the films grown by shuttered RHEED for equal thicknesses.



## Chapter 6: Conclusions & Future Work

The investigation of self-assembled barium titanate thin films has led to many discoveries. This work is the first to report and characterize off-stoichiometric RHEED oscillations for barium titanate. It has been demonstrated for the first time stoichiometric BTO films can be grown from off-stoichiometric growth conditions using codeposition – a simpler, more time efficient method for growing BTO films. This work is the first to report the use of quantitative PFM to compare ferroelectric properties of BTO based on growth approaches. A Riber MBE32 was heavily modified to grow ferroelectric barium titanate. A novel procedure for preserving an atomically flat STO substrate surface and applying a backside Pt coating for more uniform heating was developed for the growth of BTO films.

Some questions remain to verify the impact that excess barium has on material quality, which will be discussed here. While exploring excess barium as a self-limiting growth mechanism, several opportunities arose that were not pursued at the time. Furthermore, developing the procedure for measuring piezoelectric coefficients has led to many questions about better understanding PFM.

### 6.1 Further Evaluation of Self-Assembled Barium Titanate Thin Films

Defects in self-assembled barium titanate thin films have not been fully assessed. Ruddleson-Popper planar faults can form within BTO films. In BTO, full or partial BaO layers could form and would allow for the excess incorporation of barium inside a film. These layers may have the same binding energy as BTO and would not show up in XPS analysis; furthermore, XRD would not reveal them either as they would not have any periodic nature nor have the intensity for single layers to be detected. In order to verify these type of defects, cross-sectional transmission electron microscopy (XTEM) analysis needs to be performed.

Barium titanate is fragile under mechanical stress. XTEM sample preparation puts mechanical stress on BTO while polishing it to less than 10  $\mu\text{m}$ . A new procedure is under development to reliably measure the thickness without applying mechanical stress that is typical through the use of a micrometer. Silicon has been incorporated as an optical indicator that changes to red at less than 10  $\mu\text{m}$  [177]. The polishing procedure has been optimized and testing the ion milling procedure is underway.

The most difficult defects to assess in insulators are point defects. In semiconductors, Hall effect measurements are used to probe point defects by measuring the carrier mobility in a material. In order to understand to what extent the excess barium limits the stoichiometry, thermal conductivity could be measured using time-domain thermoreflectance [92].

## 6.2 Barium Titanate Quantum Dots

Growing and characterizing barium titanate quantum dots was the originally proposed project of this PhD work. BTO dots were not easily formed through SK growth like InAs on GaAs. While some systems that form quantum dots through SK rely on compressive strain (negative mismatch) [178], [179], the only substrate that showed three-dimensional RHEED patterns during growth was MgO (Table 9), which had tensile strain.

**Table 9.** Substrates for BTO dot growth.

Substrate	Lattice Constant ( $\text{\AA}$ )	Mismatch (%)	Dots?
YAlO <sub>3</sub> (001)	3.71	-8.4	No
LaAlO <sub>3</sub>	3.81	-4.7	No
MgO	4.21	+5.2	Yes
LSAT (001)	3.87	-3.1	No
SrLaAlO <sub>4</sub>	3.76	-6.1	No

The interest in growing BTO on MgO is for encouraging inplane polarization. Polarization vortices have been predicted within BTO dots [46], [180] but not observed in free standing BTO dots[181], [182]. The tensile stress encourages inplane polarization that could lead to polarization vortices. Investigating the ferroelectric properties of these dots will be a challenge to use PFM and XTEM since they are neither on a conductive substrate or uniform.

Similar to the spotty patterns observed during BTO growth on MgO (Figure 78A), a spotty pattern was formed during growth with excess barium (Figure 78B) on STO:Nb. Dots were formed (Figure 78C) that showed piezoresponse (Figure 78D), suggesting those dots were BTO. There also seemed to be a reduction in the piezoresponse in the middle of the dot. Further growths and PFM studies on both systems should be investigated.

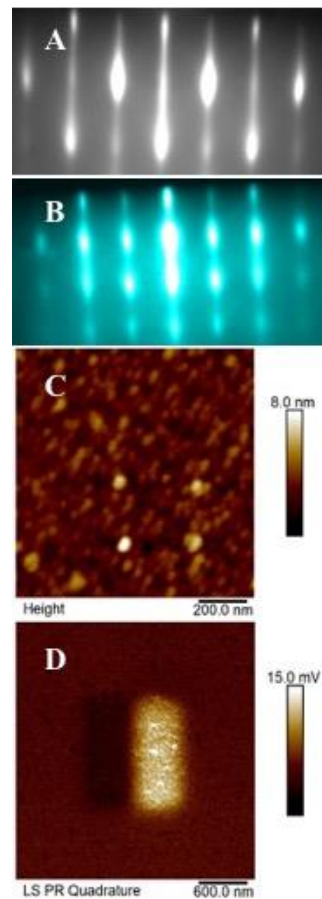


**Figure 78.** Spotty RHEED pattern of BTO grown on MgO (A) and with excess Ba on STO:Nb (B). AFM confirmed dots formed (C) that showed unique piezoresponse on dots (D).

### 6.3 Flexoelectricity and Friction

At the nanoscale, barium titanate becomes easier to bend. Bending creates polarization (Figure 79), a phenomenon called flexoelectricity. When a BTO film is pushed upon with significant force by an AFM probe, the bending becomes strong enough to reverse the polarization.

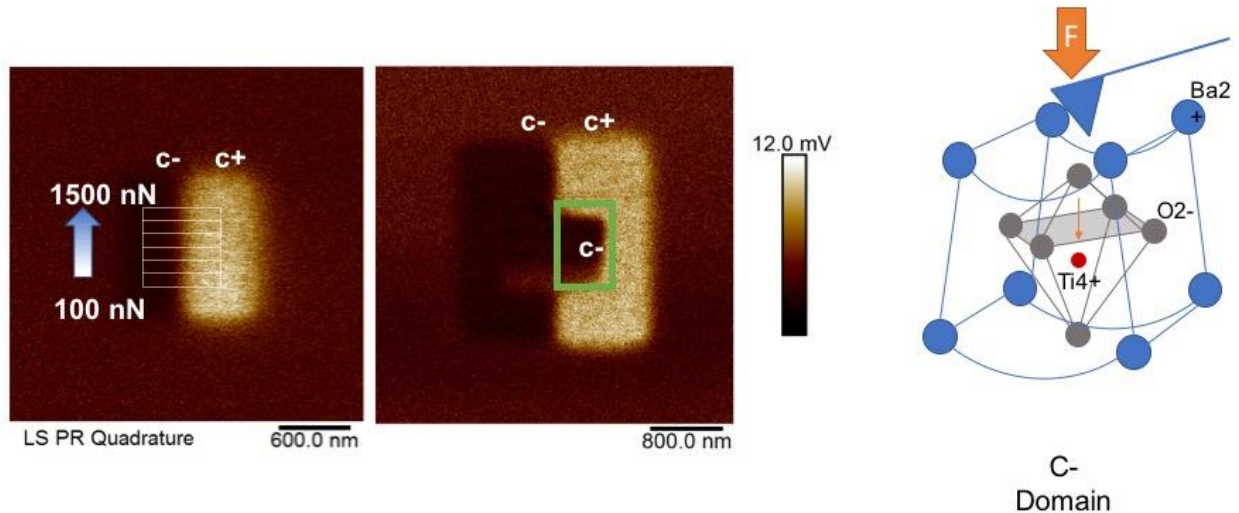


**Figure 79.** Gradient force (left) applied to poled region. Polarization switch due to mechanically bending the film (middle). Graphic showing how bending induces polarization in BTO (right).

For a 5 nm BTO thin film grown on STO:Nb (0.5% wt), a 180° domain was pressed with a force gradient seen in Figure 79. When examining the piezoresponse after bending, the c+ domain had completely reversed to a c- domain at ~900 nN. Mechanically poling also opens the possibility of measuring the piezoelectric response of BTO dots, since a large (>100 V) poling voltage isn't required. For dots, the ability to push from the top and side opens up a new possibility for altering the polarization state within the dot. The ability to induce polarization with bending at the nanoscale opens up a wide variety of applications.

It was also discovered that friction is lower in a c- domain of a 5 nm BTO thin film. Three different regions were poled (Figure 80 right to left): c+ domain electrically poled, c-

domain electrically poled, and c- domain mechanically poled. A lateral force microscopy (LFM) measurement was then performed on this poled region and found that the c- domain mechanically poled had the lowest relative friction. Understanding why the mechanically poled region showed the lowest friction is the next step of research.

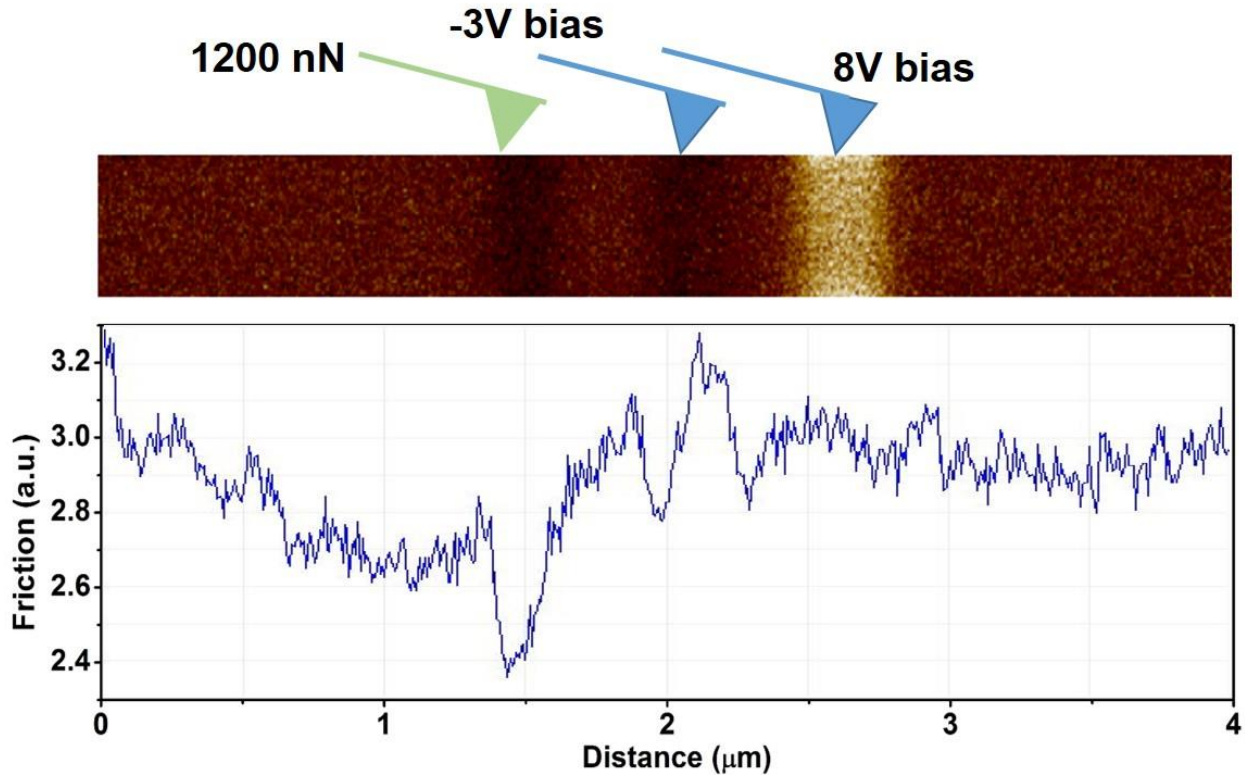


**Figure 80.** Three different regions of BTO were poled both electrically and mechanically (top). The friction plot indicated the mechanically poled region shows lowest friction (bottom).

A potential application for BTO thin films are force activated friction reducing coatings. The coating would only be used when a sufficient force gradient is applied, which would increase its longevity. BTO is also biocompatible, opening up the possibility for reducing friction in medical joints. Understanding polycrystalline BTO coatings on common implant materials needs to be evaluated for real-world situation impact. Wear testing needs to be performed to understand how long the BTO coating would last.

## 6.4 Ferroelectric Properties as a Function of BTO Thickness

Many theoretical and a few experimental studies have investigated the ferroelectric properties with decreasing thickness. There are even fewer experimental studies of a single monolayer of a ferroelectric material. The focus of many of these studies was primarily to determine if out-of-plane polarization existed. A series of BTO films were grown to investigate ferroelectric properties as a function of thickness. The series included thicknesses 54 nm, 40 nm, 20 nm, 12 nm, 5 nm, 1.2 nm and 0.4 nm.

The initial investigation focused on the piezoelectric coefficient as a function of thickness. The piezoelectric coefficient was determined at 40 nm and 5 nm. The 5 nm BTO film had a larger  $d_{33}$  than the 40 nm film. Work is ongoing to investigate if this trend continues at 1.2 nm (3 ML) and 0.4 nm (1 ML). It is theoretically predicted that below a critical thickness, out-of-plane polarization disappears. Preliminary measurements show that both 3 ML and 1 ML of BTO shows piezoresponse and  $180^\circ$  domains. The strain from the substrate enhances the polarization and removes the critical thickness. However, recent PFM measurements on  $\text{MoS}_2$  have shown out-of-plane piezoresponse, which is a material with only in-plane polarization [175]. Understanding the origin of the piezoresponse for 1 and 3 ML is one of the next areas of investigation of this research group.

Beyond the piezoresponse, investigating domain size, poling time, and flexoelectric effect will be investigated as a function of thickness down to one monolayer. Understanding how the size of domains change as function of both poling time and time after poling will yield an understanding of how thickness plays a role in determining the natural domain size. Looking at the force required to mechanically pole as a function of thickness will help optimize BTO coatings for applications in reducing friction. These properties are expected to change at the nanoscale and yield new insight into the behavior of these materials that has not been clarified.

The discovery of a new self-limiting mechanism opens up a way of investigating ferroelectricity more reliably. Removing variation in stoichiometry as a variable will make it easier to understand how the ferroelectric properties change as a function of thickness.

## References

- [1] M. Murakami, Y. Ohishi, N. Hirao, and K. Hirose, "A perovskitic lower mantle inferred from high-pressure, high-temperature sound velocity data," *Nature*, vol. 485, no. 7396, pp. 90–94, May 2012.
- [2] M. A. Peña and J. L. G. Fierro, "Chemical Structures and Performance of Perovskite Oxides," *Chem. Rev.*, vol. 101, no. 7, pp. 1981–2018, Jul. 2001.
- [3] R. Cohen, *Fundamental physics of ferroelectrics 2002 : Washington, DC, 3-6 February 2002*, vol. 626. 2002.
- [4] T. Tybell, C. H. Ahn, and J. M. Triscone, "Ferroelectricity in thin perovskite films," *Appl Phys Lett*, vol. 75, no. 6, pp. 856–858, Aug. 1999.
- [5] J. Scott and C. Paz de Araujo, "Ferroelectric Memories," *Science*, vol. 246, no. 4936, pp. 1400–1405, Dec. 1989.
- [6] J. M. Gregg, "Ferroelectrics at the nanoscale," *Phys Status Solidi A*, vol. 206, no. 4, pp. 577–587, 2009.
- [7] A. J. Bell, "Ferroelectrics: The role of ceramic science and engineering," *J Eur Ceram Soc*, vol. 28, no. 7, pp. 1307–1317, 2008.
- [8] N. Reyren, S. Thiel, A. Caviglia, L. Kourkoutis, G. Hammerl, C. Richter, C. Schneider, T. Kopp, A. Ruetschi, D. Jaccard, M. Gabay, D. Muller, J. Triscone, and J. Mannhart, "Superconducting Interfaces Between Insulating Oxides," *Science*, vol. 317, no. 5842, pp. 1196–1199, Aug. 2007.
- [9] C. Webb, S. L. Weng, J. N. Eckstein, N. Missert, K. Char, D. G. Schlom, E. S. Hellman, M. R. Beasley, A. Kapitulnik, and J. S. Harris Jr, "Growth of high T<sub>c</sub> superconducting thin films using molecular beam epitaxy techniques," *Appl Phys Lett*, vol. 51, no. 15, pp. 1191–1193, Oct. 1987.
- [10] J. Wang, M. Singh, M. Tian, N. Kumar, B. Liu, C. Shi, J. K. Jain, N. Samarth, T. E. Mallouk, and M. H. W. Chan, "Interplay between superconductivity and ferromagnetism in crystalline nanowires," *Nature Physics*, vol. 6, no. 5, pp. 389–394, 2010.
- [11] A. C. Anderson, R. L. Slattery, B. I. Choi, M. I. Filk, and M. I. Cima, "Radiative substrate heating for high-t (c) superconducting thin-film deposition: Film-growth-induced temperature variation.," *J. of Vacuum Science*, vol. 10, pg 3407, 1992.
- [12] J. N. Eckstein, I. Bozovic, K. E. von Dessionneck, D. G. Schlom, J. S. Harris Jr, and S. M. Baumann, "Atomically layered heteroepitaxial growth of single-crystal films of superconducting Bi<sub>2</sub>Sr<sub>2</sub>Ca<sub>2</sub>Cu<sub>3</sub>O<sub>x</sub>," *Appl Phys Lett*, vol. 57, no. 9, pp. 931–933, Aug. 1990.



- [13] D. D. Berkley, B. R. Johnson, N. Anand, K. M. Beauchamp, L. E. Conroy, A. M. Goldman, J. Maps, K. Mauersberger, M. L. Mecartney, J. Morton, M. Tuominen, and Y.-J. Zhang, "In situ formation of superconducting  $\text{YBa}_2\text{Cu}_3\text{O}_{7-x}$  thin films using pure ozone vapor oxidation," *Appl Phys Lett*, vol. 53, no. 20, p. 1973, Sept. 1988.
- [14] L. Maritato, A. Galdi, P. Orgiani, J. W. Harter, J. Schubert, K. M. Shen, and D. G. Schlom, "Layer-by-layer shuttered molecular-beam epitaxial growth of superconducting  $\text{Sr}_{1-x}\text{La}_x\text{CuO}_2$  thin films," *J Appl Phys*, vol. 113, no. 5, p. 053911, 2013.
- [15] D. Kuberkar, D. Rana, C. Thaker, K. Mavani, D. Kundaliya, and S. Malik, "Ferromagnetism and charge ordering in  $(\text{LaR})(0.5)(\text{CaSr})(0.5)\text{MnO}_3$  ( $\text{R} = \text{Nd, Eu, Tb}$ ) compounds," *Journal of Magnetism and Magnetic Materials*, 2004, vol. 272, pp. 1823–1825.
- [16] D. Albrecht, S. Lisenkov, W. Ren, D. Rahmedov, I. A. Kornev, and L. Bellaiche, "Ferromagnetism in multiferroic  $\text{BiFeO}_3$  films: A first-principles-based study," *Physical Review B*, vol. 81, no. 14, p. 140401, 2010.
- [17] Y. Yamada, K. Ueno, T. Fukumura, H. T. Yuan, H. Shimotani, Y. Iwasa, L. Gu, S. Tsukimoto, Y. Ikuhara, and M. Kawasaki, "Electrically Induced Ferromagnetism at Room Temperature in Cobalt-Doped Titanium Dioxide," *Science*, vol. 332, no. 6033, pp. 1065–1067, 2011.
- [18] I. Stolichnov, S. W. E. Riester, H. J. Trodahl, N. Setter, A. W. Rushforth, K. W. Edmonds, R. P. Champion, C. T. Foxon, B. L. Gallagher, and T. Jungwirth, "Non-volatile ferroelectric control of ferromagnetism in  $(\text{Ga, Mn})\text{As}$ ," *Nat Mater*, vol. 7, no. 6, pp. 464–467, 2008.
- [19] S. Qin, D. Liu, Z. Zuo, Y. Sang, and X. Zhang, "UV-irradiation-enhanced ferromagnetism in  $\text{BaTiO}_3$ ," *The Journal of Physical Chemistry Letters*, vol. 1, no. 1, pp. 238–241, 2009.
- [20] T. Shimada, Y. Uratani, and T. Kitamura, "Vacancy-driven ferromagnetism in ferroelectric  $\text{PbTiO}_3$ ," *Appl Phys Lett*, vol. 100, no. 16, p. 162901, Apr. 2012.
- [21] D. Khomskii, "Multiferroics: Different ways to combine magnetism and ferroelectricity," *J Magn Magn Mater*, vol. 306, no. 1, pp. 1–8, 2006.
- [22] S. Kharrazi, D. Kundaliya, S. Gosavi, S. Kulkarni, T. Venkatesan, S. Ogale, J. Urban, S. Park, and S. Cheong, "Multiferroic  $\text{TbMnO}_3$  nanoparticles," *Solid State Communications*, vol. 138, no. 8, pp. 395–398, 2006.
- [23] Y. Tokura, "Multiferroics--toward strong coupling between magnetization and polarization in a solid," *J Magn Magn Mater*, vol. 310, no. 2, pp. 1145–1150, 2007.

- [24] R V K Mangalam, N. Ray, U. V. Waghmare, A. Sundaresan, C N R Rao “Multiferroic properties of nanocrystalline BaTiO<sub>3</sub>,” *Solid State Communications*, vol. 149, no. 1, pp. 1–5, Jan. 2009.
- [25] L. Weston, X. Y. Cui, S. P. Ringer, and C. Stampfl, “Multiferroic crossover in perovskite oxides,” *Physical Review B*, vol. 93, no. 16, p. 165210, Apr. 2016.
- [26] J. Kaur, R. K. Kotnala, and K. C. Verma, “Multiferroic properties of Ba(FexTi1-x)O<sub>3</sub> nanorods,” *Materials Letters*, vol. 65, no. 19, pp. 3160–3163, Oct. 2011.
- [27] S.-W. Cheong and M. Mostovoy, “Multiferroics: a magnetic twist for ferroelectricity,” *Nat Mater*, vol. 6, no. 1, pp. 13–20, 2007.
- [28] M. Bibes and A. Barthelemy, “Multiferroics: Towards a magnetoelectric memory,” *Nat Mater*, vol. 7, no. 6, pp. 425–426, 2008.
- [29] I. A. Kornev, S. Lisenkov, R. Haumont, B. Dkhil, and L. Bellaiche, “Finite-temperature properties of multiferroic BiFeO<sub>3</sub>,” *Phys Rev Lett*, vol. 99, no. 22, pp. –, 2007.
- [30] L. W. Martin, Y. H. Chu, and R. Ramesh, “Advances in the growth and characterization of magnetic, ferroelectric, and multiferroic oxide thin films,” *Mat Sci Eng R*, vol. 68, no. 4, pp. 89–133, 2010.
- [31] E. Fatuzzo and W. Merz, *Ferroelectricity*, vol. 7., pgs 30-33, 1967.
- [32] M. E. Lines and A. M. Glass, *Principles and Applications of Ferroelectrics and Related Materials*. Oxford University Press, pgs 11-23, 1977.
- [33] D. G. Schlom, L.-Q. Chen, X. Pan, A. Schmehl, and M. A. Zurbuchen, “A thin film approach to engineering functionality into oxides,” *J Am Ceram Soc*, vol. 91, no. 8, pp. 2429–2454, 2008.
- [34] M. Henini, *Molecular Beam Epitaxy*. , Elsevier Science, pp. 389-456, 2012.
- [35] A. Bhalla, R. Guo, and R. Roy, “The perovskite structure - a review of its role in ceramic science and technology,” *Mater Res Innov*, vol. 4, no. 1, pp. 3–26, 2000.
- [36] N. A. Pertsev and B. Dkhil, “Strain sensitivity of polarization in perovskite ferroelectrics,” *Appl Phys Lett*, vol. 93, no. 12, p. 122903, Sep. 2008.
- [37] N. A. Benedek, J. M. Rondinelli, H. Djani, P. Ghosez, and P. Lightfoot, “Understanding ferroelectricity in layered perovskites: new ideas and insights from theory and experiments,” *Dalton Trans.*, vol. 44, no. 23, pp. 10543–10558, Jun. 2015.
- [38] M. J. Polking, “Deciphering the physics and chemistry of perovskites with transmission electron microscopy,” *Nanoscale*, vol. 8, no. 12, pp. 6237–6248, Mar.

2016.

- [39] A. M. Glazer, "The classification of tilted octahedra in perovskites," *Acta Crystallogr B Struct Crystallogr Cryst Chem*, vol. 28, no. 11, pp. 3384–3392, Nov. 1972.
- [40] I. B. Bersuker, "On the origin of ferroelectricity in perovskite-type crystals," *Physics Letters*, vol. 20, no. 6, pp. 589–590, Apr. 1966.
- [41] R. Cohen, "Origin of ferroelectricity in perovskite oxides," *Nature*, vol. 358, no. 6382, pp. 136–138, 1992.
- [42] G. H. Jonker and J. H. van Santen, "Properties of Barium Titanate in Connection with Its Crystal Structure.," *Science*, vol. 109, no. 2843, pp. 632–635, Jun. 1949.
- [43] W. F. Forrester and R. M. Hinde, "Crystal Structure of Barium Titanate," *Nature*, vol. 156, no. 3954, pp. 177–177, 1945.
- [44] H. Lu, C. W. Bark, D. Esque de los Ojos, J. Alcala, C. B. Eom, G. Catalan, and A. Gruverman, "Mechanical Writing of Ferroelectric Polarization," *Science*, vol. 336, no. 6077, pp. 59–61, Apr. 2012.
- [45] H. Fu and L. Bellaiche, "Ferroelectricity in barium titanate quantum dots and wires," *Phys Rev Lett*, vol. 91, no. 25, pp. 257601–257601, 2003.
- [46] I. Naumov, L. Bellaiche, and H. Fu, "Unusual phase transitions in ferroelectric nanodisks and nanorods," *Nature*, vol. 432, no. 7018, pp. 737–740, 2004.
- [47] J. Young, P. Lalkiya, and J. M. Rondinelli, "Design of noncentrosymmetric perovskites from centric and acentric basic building units," *J. Mater. Chem. C*, vol. 4, no. 18, pp. 4016–4027, May 2016.
- [48] K. Rabe, M. Dawber, C. Lichtensteiger, C. Ahn, and J. Triscone, "Modern Physics of Ferroelectrics: Essential Background," *Topics in applied physics*, vol. 105, p. 1, 2007.
- [49] Y. Tsur, T. D. Dunbar, and C. A. Randall, "Crystal and Defect Chemistry of Rare Earth Cations in BaTiO<sub>3</sub>," *Journal of Electroceramics*, vol. 7, no. 1, pp. 25–34, 2001.
- [50] G. Catalan and J. F. Scott, "Physics and Applications of Bismuth Ferrite," *Adv. Mater.*, vol. 21, no. 24, pp. 2463–2485, Jun. 2009.
- [51] N. A. Spaldin, "A beginner's guide to the modern theory of polarization," *Journal of Solid State Chemistry*, vol. 195, pp. 2–10, Nov. 2012.
- [52] D. Khomskii, "Classifying multiferroics: Mechanisms and effects," *Physics*, vol. 2, p. 20, 2009.
- [53] Y. Iwazaki, T. Suzuki, S. Sekiguchi, and M. Fujimoto, "Thermal Stability of Artificial

- SrTiO<sub>3</sub>/SrO Superlattice Epitaxially Grown on SrTiO<sub>3</sub> Single Crystal,” *Jpn J Appl Phys*, vol. 39, no. 4, pp. L303–L305, Apr. 2000.
- [54] G. King and P. M. Woodward, “Cation ordering in perovskites,” *J. Mater. Chem.*, vol. 20, no. 28, pp. 5785–5796, Jul. 2010.
- [55] O. Y. Gorbenko, S. V. Samoilenkov, I. E. Graboy, and A. R. Kaul, “Epitaxial Stabilization of Oxides in Thin Films,” *Chemistry of Materials*, vol. 14, no. 10, pp. 4026–4043, Oct. 2002.
- [56] M. T. Buscaglia, M. Sennour, V. Buscaglia, C. Bottino, V. Kalyani, and P. Nanni, “Formation of Bi<sub>4</sub>Ti<sub>3</sub>O<sub>12</sub> One-Dimensional Structures by Solid-State Reactive Diffusion. From Core-Shell Templates to Nanorods and Nanotubes,” *Cryst Growth Des*, vol. 11, no. 4, pp. 1394–1401, 2011.
- [57] S. Stemmer, T. Höche, R. Keding, C. Rüssel, R. Schneider, N. D. Browning, S. K. Streiffer, and H. J. Kleebe, “Oxidation states of titanium in bulk barium titanates and in (100) fiber-textured (Ba<sub>x</sub>Sr<sub>1-x</sub>)Ti<sub>1+y</sub>O<sub>3+z</sub> thin films,” *Appl Phys Lett*, vol. 79, no. 19, pp. 3149–3151, Nov. 2001.
- [58] J. A. Enterkin, A. K. Subramanian, B. C. Russell, M. R. Castell, K. R. Poeppelmeier, and L. D. Marks, “A homologous series of structures on the surface of SrTiO<sub>3</sub>(110),” *Nat Mater*, Feb. 2010.
- [59] S. Lee, A. R. Damodaran, P. Gorai, N. Oh, J. A. Moyer, J. H. Kwon, N. Ferdous, A. Shah, Z. Chen, E. Breckenfeld, R. V. K. Mangalam, P. V. Braun, P. Schiffer, M. Shim, J. M. Zuo, E. Ertekin, and L. W. Martin, “A Novel, Layered Phase in Ti-Rich SrTiO<sub>3</sub> Epitaxial Thin Films,” *Adv. Mater.*, vol. 27, no. 5, pp. 861–868, Feb. 2015.
- [60] S. Stemmer, S. K. Streiffer, N. D. Browning, and A. I. Kingon, “Accommodation of nonstoichiometry in (100) fiber-textured (Ba<sub>[sub x]</sub>Sr<sub>[sub 1-x]</sub>)Ti<sub>[sub 1+y]</sub>O<sub>[sub 3+z]</sub> thin films grown by chemical vapor deposition,” *Appl Phys Lett*, vol. 74, no. 17, p. 2432, 1999.
- [61] J. Rumble, Ed., *CRC Handbook of Chemistry and Physics, 98th Edition*. CRC Press, pp 234-254, 2017.
- [62] Y. Li, R. Yu, H. Zhou, Z. Cheng, and X. Wang, “Direct Observation of Thickness Dependence of Ferroelectricity in Freestanding BaTiO<sub>3</sub> Thin Film,” *Journal of the American Ceramic Society*, 98, 2710-2712, 2015.
- [63] Y. Li, R. Yu, T. Shi, Z. Liao, D. Song, H. Zhou, Z. Cheng, and J. Zhu, “Atomic structure and polarity compensation of BaTiO<sub>3</sub> (1 1 1) surface,” *Journal of Physics: Condensed Matter*, vol. 27, no. 9, p. 095901, Mar. 2015.
- [64] J. F. Scott, “Device Physics of Ferroelectric Memories,” *Ferroelectrics*, vol. 183, pp. 51–63, 1996.

- [65] J. Scott, “Applications of Modern Ferroelectrics,” *Science*, vol. 315, no. 5814, pp. 954–959, Feb. 2007.
- [66] J. F. Scott, “A review of ferroelectric switching,” *Ferroelectrics*, vol. 503, no. 1, pp. 117–132, 2016.
- [67] M. Dawber, K. Rabe, and J. Scott, “Physics of thin-film ferroelectric oxides,” *Reviews of Modern Physics*, vol. 77, no. 4, p. 1083, 2005.
- [68] A. Pramanick, A. D. Prewitt, J. S. Forrester, and J. L. Jones, “Domains, Domain Walls and Defects in Perovskite Ferroelectric Oxides: A Review of Present Understanding and Recent Contributions,” *Crit Rev Solid State*, vol. 37, no. 4, pp. 243–275, Dec. 2012.
- [69] C. T. Nelson, P. Gao, J. R. Jokisaari, C. Heikes, C. Adamo, A. Melville, S.-H. Baek, C. M. Folkman, B. Winchester, Y. Gu, Y. Liu, K. Zhang, E. Wang, J. Li, L.-Q. Chen, C.-B. Eom, D. G. Schlom, and X. Pan, “Domain Dynamics During Ferroelectric Switching,” *Science*, vol. 334, no. 6058, pp. 968–971, 2011.
- [70] S. V. Kalinin, B. J. Rodriguez, A. Y. Borisevich, A. P. Baddorf, N. Balke, H. J. Chang, L.-Q. Chen, S. Choudhury, S. Jesse, P. Maksymovych, M. P. Nikiforov, and S. J. Pennycook, “Defect-Mediated Polarization Switching in Ferroelectrics and Related Materials: From Mesoscopic Mechanisms to Atomistic Control,” *Adv. Mater.*, vol. 22, no. 3, pp. 314–322, Jan. 2010.
- [71] S. Lee, C. A. Randall, and Z. K. Liu, “Modified Phase Diagram for the Barium Oxide–Titanium Dioxide System for the Ferroelectric Barium Titanate,” *Journal of the American Ceramic Society*, vol. 90, no. 8, pp. 2589–2594, Aug. 2007.
- [72] S. Lee and C. A. Randall, “A modified Vegard’s law for multisite occupancy of Ca in BaTiO<sub>3</sub>–CaTiO<sub>3</sub> solid solutions,” *Appl Phys Lett*, vol. 92, no. 11, p. 111904, Mar. 2008.
- [73] J. Hwang, T. Kolodiazny, J. Yang, and M. Couillard, “Doping and temperature-dependent optical properties of oxygen-reduced BaTiO<sub>3</sub>– $\delta$ ,” *Phys. Rev. B*, vol. 82, no. 21, p. 214109, Dec. 2010.
- [74] S. Lee, S. Moon, M. Kwak, H. Ryu, Y. Kim, and K. Kang, “High dielectric tunability of (Ba, Sr)TiO<sub>3</sub> thin films and their coplanar waveguide phase shifter applications,” *Jpn J Appl Phys I*, vol. 43, no. 9, pp. 6750–6754, 2004.
- [75] S. Landau, P. Weiss, N. Junghans, B. Kolbesen, D. Adderton, P. De Wolf, G. Schindler, W. Hartner, F. Hintermaier, C. Dehm, and C. Mazure, “Characterization of high-k dielectric/ferroelectric materials: capabilities of scanning probe microscopy (SPM),” vol. 3895, pp. 188–195, 1999.

- [76] D. A. Tenne, A. Bruchhausen, N. D. Lanzillotti-Kimura, A. Fainstein, R. S. Katiyar, A. Cantarero, A. Soukiassian, V. Vaithyanathan, J. H. Haeni, W. Tian, D. G. Schlom, K. J. Choi, D. M. Kim, C. B. Eom, H. P. Sun, X. Q. Pan, Y. L. Li, L. Q. Chen, Q. X. Jia, S. M. Nakhmanson, K. M. Rabe, and X. X. Xi, "Probing nanoscale ferroelectricity by ultraviolet Raman spectroscopy," *Science*, vol. 313, no. 5793, pp. 1614–1616, 2006.
- [77] W. Chang, S. Kirchoefer, J. Bellotti, and J. Pond, "(Ba,Sr)TiO<sub>3</sub> ferroelectric thin films for tunable microwave applications," *Rev Mex Fis*, vol. 50, no. 5, pp. 501–505, 2004.
- [78] R. C. Haislmaier, R. Engel-Herbert, and V. Gopalan, "Stoichiometry as key to ferroelectricity in compressively strained SrTiO<sub>3</sub> films," *Appl Phys Lett*, vol. 109, no. 3, p. 032901, Jul. 2016.
- [79] Y. S. Kim, D. J. Kim, T. H. Kim, T. W. Noh, J. S. Choi, B. H. Park, and J. G. Yoon, "Observation of room-temperature ferroelectricity in tetragonal strontium titanate thin films on SrTiO<sub>3</sub> (001) substrates," *Appl Phys Lett*, vol. 91, no. 4, p. 042908, Jul. 2007.
- [80] K. J. Choi, M. Biegalski, Y. L. Li, A. Sharan, J. Schubert, R. Uecker, P. Reiche, Y. B. Chen, X. Q. Pan, V. Gopalan, L. Q. Chen, D. G. Schlom, and C. B. Eom, "Enhancement of Ferroelectricity in Strained BaTiO<sub>3</sub> Thin Films," *Science*, vol. 306, no. 5698, pp. 1005–1009, Nov. 2004.
- [81] K.-I. Mimura and K. Kato, "Enhanced dielectric properties of BaTiO<sub>3</sub> nanocube assembled film in metal–insulator–metal capacitor structure," *Appl. Phys. Express*, vol. 7, no. 6, p. 061501, Jun. 2014.
- [82] J. B. Neaton and K. M. Rabe, "Theory of polarization enhancement in epitaxial BaTiO<sub>3</sub>/SrTiO<sub>3</sub> superlattices," *Appl Phys Lett*, vol. 82, no. 10, pp. 1586–1588, Mar. 2003.
- [83] W. Tian, J. C. Jiang, X. Q. Pan, J. H. Haeni, Y. L. Li, L. Q. Chen, D. G. Schlom, J. B. Neaton, K. M. Rabe, and Q. X. Jia, "Structural evidence for enhanced polarization in a commensurate short-period BaTiO<sub>3</sub>/SrTiO<sub>3</sub> superlattice," *Appl Phys Lett*, vol. 89, no. 9, p. 092905, 2006.
- [84] A. Ya'akovovich, S. Baltianski, and Y. Tsur, "I–V relations and enhanced mobility of metal vacancies in acceptor doped polycrystalline BaTiO<sub>3</sub> under oxygen activity gradient," *Materials Science Technology*, vol. 25, no. 11, pp. 1329–1333, Nov. 2009.
- [85] F. Yang, K. J. Jin, H. B. Lu, M. He, C. WANG, and J. Wen, "Oxygen vacancy induced magnetism in BaTiO<sub>3</sub>– $\delta$  and Nb: BaTiO<sub>3</sub>– $\delta$  thin films," *Science China Physics*, vol. 53, Issue 5, 2010.
- [86] C. H. Park and D. J. Chadi, "Microscopic study of oxygen-vacancy defects in ferroelectric perovskites," *Physical Review B*, vol. 57, no. 22, pp. R13961–R13964, Jun. 1998.

- [87] D. M. Duffy, J. P. Hoare, and P. W. Tasker, "Vacancy formation energies near the surface of an ionic crystal," *Journal of Physics C*, vol. 17, no. 7, 1984.
- [88] K. Shimoyama, K. Kubo, M. Lida, K. Yamabe, and T. Maeda, "Changes in surface states during epitaxial growth of BaTiO<sub>3</sub> on SrTiO<sub>3</sub> substrate in connection with composition deviation," *J Vac Sci Technol A*, vol. 19, no. 5, pp. 2083–2088, 2001.
- [89] T. Suzuki, Y. Nishi, and M. Fujimoto, "Effect of Nonstoichiometry on Microstructure of Epitaxially Grown BaTiO<sub>3</sub> Thin Films," *Jpn J Appl Phys*, vol. 39, no. 10, pp. 5970–5976, Oct. 2000.
- [90] D. Damjanovic, "Ferroelectric, dielectric and piezoelectric properties of ferroelectric thin films and ceramics," *Rep Prog Phys*, vol. 61, no. 9, pp. 1267–1324, Sep. 1998.
- [91] L. Bellaiche, A. Garcia, and D. Vanderbilt, "Finite-temperature properties of PZT alloys from first principles," *Physical Review Letters*, no. 84, pp. 5427–5430, 21-Apr-2000.
- [92] D.-W. Oh, J. Ravichandran, C.-W. Liang, W. Siemons, B. Jalan, C. M. Brooks, M. Huijben, D. G. Schlom, S. Stemmer, L. W. Martin, A. Majumdar, R. Ramesh, and D. G. Cahill, "Thermal conductivity as a metric for the crystalline quality of SrTiO<sub>3</sub> epitaxial layers," *Appl Phys Lett*, vol. 98, no. 22, p. 221904, 2011.
- [93] D. E. Rase and R. Roy, "Phase Equilibria in the System BaO-TiO<sub>2</sub>," *Journal of the American Ceramic Society*, vol. 38, no. 3, pp. 102–113, Jun. 2006.
- [94] H. M. O'Bryan and J. Thomson, "Phase Equilibria in the TiO<sub>2</sub>-Rich Region of the System BaO-TiO<sub>2</sub>," *Journal of the American Ceramic Society*, vol. 57, no. 12, pp. 522–526, Dec. 1974.
- [95] T. Maekawa, Y. Sugiki, S. Matsumoto, S. Adachi, S. Yoda, and K. Kinoshita, "Numerical analysis of crystal growth of an InAs–GaAs binary semiconductor by the Travelling Liquidus-Zone method under microgravity conditions," *International Journal of Heat and Mass Transfer*, vol. 47, no. 21, pp. 4535–4546, Oct. 2004.
- [96] Y. Tokuda, S. Kobayashi, T. Ohnishi, T. Mizoguchi, N. Shibata, Y. Ikuhara, and T. Yamamoto, "Growth of Ruddlesden-Popper type faults in Sr-excess SrTiO<sub>3</sub> homoepitaxial thin films by pulsed laser deposition," *Appl Phys Lett*, vol. 99, no. 17, p. 173109, Oct. 2011.
- [97] T. Suzuki, Y. Nishi, M. Fujimoto, "Defect structure in homoepitaxial non-stoichiometric strontium titanate thin films," *Philosophical Magazine A*, vol. 80, no. 3, pp. 621–637, Aug. 2009.
- [98] A. P. Kajdos and S. Stemmer, "Hybrid molecular beam epitaxy for the growth of complex oxide materials," in *Epitaxial Growth of Complex Metal Oxides*, Elsevier, 2015, pp. 47–68.

- [99] J. K. Lee, K. S. Hong, and J. W. Jang, "Roles of Ba/Ti Ratios in the Dielectric Properties of BaTiO<sub>3</sub> Ceramics," *Journal of the American Ceramic Society*, vol. 84, no. 9, pp. 2001–2006, Sep. 2001.
- [100] A. Beauger, J. C. Mutin, and J. C. Niepce, "Role and behaviour of orthotitanate Ba<sub>2</sub>TiO<sub>4</sub> during the processing of BaTiO<sub>3</sub> based ferroelectric ceramics," *J Mater Sci*, vol. 19, no. 1, pp. 195–201, Jan. 1984.
- [101] S. Lee, Z. K. Liu, M.-H. Kim, and C. A. Randall, "Influence of nonstoichiometry on ferroelectric phase transition in BaTiO<sub>3</sub>," *J Appl Phys*, vol. 101, no. 5, p. 054119, Mar. 2007.
- [102] Y. Zhou, C.-S. Park, C.-H. Wu, D. Maurya, M. Murayama, A. Kumar, R. S. Katiyar, and S. Priya, "Microstructure and surface morphology evolution of pulsed laser deposited piezoelectric BaTiO<sub>3</sub> films," *J. Mater. Chem. C*, vol. 1, no. 39, pp. 6308–6315, 2013.
- [103] P. Krishnan and P. R. Munroe, "Influence of fabrication conditions on the ferroelectric polarization of barium titanate thin films," *Journal of Asian Ceramic Societies*, Vol 1, Issue 2, pp. 149-154, June 2013.
- [104] A. Barbier, C. Mocuta, D. Stanescu, P. Jegou, N. Jedrecy, and H. Magnan, "Surface composition of BaTiO<sub>3</sub>/SrTiO<sub>3</sub> (001) films grown by atomic oxygen plasma assisted molecular beam epitaxy," *J Appl Phys*, vol. 112, no. 11, p. 114116, 2012.
- [105] M.-H. M. Hsu, C. Merckling, S. El Kazzi, M. Pantouvaki, O. Richard, H. Bender, J. Meersschaut, J. Van Campenhout, P. Absil, and D. Van Thourhout, "Diffraction studies for stoichiometry effects in BaTiO<sub>3</sub> grown by molecular beam epitaxy on Ge(001)," *J Appl Phys*, vol. 120, no. 22, p. 225114, Dec. 2016.
- [106] D. G. Schlom, "Perspective: Oxide molecular-beam epitaxy rocks!," *APL Materials*, vol. 3, no. 6, p. 062403, Jun. 2015.
- [107] D. G. Schlom and L. N. Pfeiffer, "Oxide electronics: Upward mobility rocks!," *Nature Materials*, vol. 9, no. 11, pp. 881–883, Nov. 2010.
- [108] D. G. Schlom, "Oxide Molecular-Beam Epitaxy: An Introduction with Examples," <https://www.slideshare.net/nirupam12/d-schlom-oxide-molecularbeam-epitaxy>, 10-Aug-2012.
- [109] J. F. Ihlefeld, A. Kumar, V. Gopalan, D. G. Schlom, Y. B. Chen, X. Q. Pan, T. Heeg, J. Schubert, X. Ke, P. Schiffer, J. Orenstein, L. W. Martin, Y. H. Chu, and R. Ramesh, "Adsorption-controlled molecular-beam epitaxial growth of BiFeO<sub>3</sub>," *Appl Phys Lett*, vol. 91, no. 7, pp. 071922–071922–3, 2007.
- [110] C. D. Theis, J. Yeh, M. E. Hawley, G. W. Brown, and D. G. Schlom, "Adsorption-



Controlled Growth of Ferroelectric  $\text{PbTiO}_3$  and  $\text{Bi}_4\text{Ti}_3\text{O}_{12}$  Films for Nonvolatile Memory Applications by MBE,” *Materials Research Society Symposium Proceedings*, vol. 474, pp. 297–302, Mar. 1997.

- [111] B. Jalan, R. Engel-Herbert, N. J. Wright, and S. Stemmer, “Growth of high-quality  $\text{SrTiO}_3$  films using a hybrid molecular beam epitaxy approach,” *J Vac Sci Technol A*, vol. 27, no. 3, pp. 461–464, 2009.
- [112] S. Stemmer, “Stoichiometry optimization of homoepitaxial oxide thin films using x-ray diffraction,” *Applied Physics Letters*, 95, 142905, 2009.
- [113] A. P. Kajdos and S. Stemmer, “Surface reconstructions in molecular beam epitaxy of  $\text{SrTiO}_3$ ,” *Appl Phys Lett*, vol. 105, no. 19, p. 191901, Nov. 2014.
- [114] R. F.C. Farrow, “Molecular Beam Epitaxy,” Noyes Publications, pgs 178-213, 1995.
- [115] H. Shigetani, K. Kobayashi, M. Fujimoto, W. Sugimura, Y. Matsui, and J. Tanaka, “Studies of Interface and Surface Structures of  $\text{BaTiO}_3$  Thin Films Grown on  $\text{SrTiO}_3$  (001) Substrates by Mbe,” *MRS Proceedings*, vol. 440, no. 1, 1996.
- [116] K. Shimoyama, M. Kiyohara, K. Kubo, A. Uedono, and K. Yamabe, “Epitaxial growth of  $\text{BaTiO}_3/\text{SrTiO}_3$  structures on  $\text{SrTiO}_3$  substrate with automatic feeding of oxygen from the substrate,” *J Appl Phys*, vol. 92, no. 8, pp. 4625–4630, 2002.
- [117] D. G. Schlom, C. D. Theis, and M. Hawley, “The Controlled Growth of Perovskite Thin Films: Opportunities, Challenges and Synthesis,” *Integrated Thin Films and Applications*, Jan. 1997.
- [118] C. M. Brooks, L. F. Kourkoutis, T. Heeg, J. Schubert, D. A. Muller, and D. G. Schlom, “Growth of homoepitaxial  $\text{SrTiO}_3$  thin films by molecular-beam epitaxy,” *Appl Phys Lett*, vol. 94, no. 16, pp. 162905–162905, 2009.
- [119] E. N. Kaufmann, “Reflection High-Energy Electron Diffraction,” in *Characterization of Materials*, John Wiley & Sons Incorporated, 2012, p. 831.
- [120] A. Ichimiya and P. I. Cohen, *Reflection High-Energy Electron Diffraction*. Cambridge University Press, pgs 67-94, 2004.
- [121] T. W. Zhang, Z. W. Mao, Z. B. Gu, Y. F. Nie, and X. Q. Pan, “An efficient and reliable growth method for epitaxial complex oxide films by molecular beam epitaxy,” *Appl Phys Lett*, vol. 111, no. 1, p. 011601, Jul. 2017.
- [122] D. G. Schlom, L.-Q. Chen, C. J. Fennie, V. Gopalan, D. A. Muller, X. Pan, R. Ramesh, and R. Uecker, “Elastic strain engineering of ferroic oxides,” *MRS Bulletin*, vol. 39, no. 2, pp. 118–130, 2014.
- [123] Y. Matsubara, K. S. Takahashi, Y. Tokura, and M. Kawasaki, “Single-crystalline

- BaTiO<sub>3</sub> films grown by gas-source molecular beam epitaxy,” *Appl. Phys. Express*, vol. 7, no. 12, p. 125502, Dec. 2014.
- [124] E. Mikheev, A. P. Kajdos, A. J. Hauser, and S. Stemmer, “Electric field-tunable Ba<sub>x</sub>Sr<sub>1-x</sub>TiO<sub>3</sub> films with high figures of merit grown by molecular beam epitaxy,” *Appl Phys Lett*, vol. 101, no. 25, p. 252906, 2012.
- [125] M. M. Rutkowski, K. McNicholas, Z. Q. Zeng, F. Tuomisto, and L. J. Brillson, “Optical identification of oxygen vacancy formation at SrTiO<sub>3</sub>–(Ba,Sr)TiO<sub>3</sub> heterostructures,” *Journal of Physics D: Applied Physics*, vol. 47, no. 25, p. 255303, Jun. 2014.
- [126] D. Cao, M. Q. Cai, W. Hu, P. Yu, H. T. Huang. "Vacancy-induced magnetism in BaTiO<sub>3</sub>(001) thin films based on density functional theory," *Physical chemistry chemical physics : Physical Chemistry Chemical Physics*. 13. 4738-45.. (2011)
- [127] A. Raeliarijaona and H. Fu, “Mode sequence, frequency change of nonsoft phonons, and LO-TO splitting in strained tetragonal BaTiO<sub>3</sub>,” *Phys. Rev. B*, vol. 92, no. 9, p. 094303, Sep. 2015.
- [128] C. D. Theis and D. G. Schlom, “The Reactivity of Ozone Incident onto the Surface of Perovskite Thin Films Grown by MBE,” *Proceedings of the Ninth International Conference on High Temperature Materials Chemistry*, vol. 97, no. 39, pp. 610–616, Jan. 1997.
- [129] E. S. Hellman and E. H. Hartford, “Effects of oxygen on the sublimation of alkaline earths from effusion cells,” *Journal of Vacuum Science & Technology B: Microelectronics and Nanometer Structures*, vol. 12, no. 2, pp. 1178–1180, 1994.
- [130] O. Tuftte and P. Chapman, “Electron Mobility in Semiconducting Strontium Titanate,” *Phys Rev*, vol. 155, no. 3, pp. 796–802, 1967.
- [131] T. Zhao, F. Chen, H. Lu, G. Yang, and Z. Chen, “Thickness and oxygen pressure dependent structural characteristics of BaTiO<sub>3</sub> thin films grown by laser molecular beam epitaxy,” *J Appl Phys*, vol. 87, no. 10, pp. 7442–7447, May 2000.
- [132] J. Haeni, C. Theis, and D. Schlom, “RHEED intensity oscillations for the stoichiometric growth of SrTiO<sub>3</sub> thin films by reactive molecular beam epitaxy,” *Journal of Electroceramics*, vol. 4, no. 2, pp. 385–391, 2000.
- [133] B. Bolger and P. K. Larsen, “Video system for quantitative measurements of RHEED patterns,” *Rev Sci Instrum*, vol. 57, no. 7, pp. 1363–1367, 1986.
- [134] W. Braun, *Applied RHEED*. Berlin: Springer-Verlag, pgs 2-29, 1999.
- [135] M. Brahlek, L. Zhang, H.-T. Zhang, J. Lapano, L. R. Dedon, L. W. Martin, and R. Engel-Herbert, “Mapping growth windows in quaternary perovskite oxide systems by

- hybrid molecular beam epitaxy,” *Appl Phys Lett*, vol. 109, no. 10, p. 101903, Sep. 2016.
- [136] M. Kawasaki, K. Takahashi, T. Maeda, and R. Tsuchiya, “Atomic control of the SrTiO<sub>3</sub> crystal surface,” *Science*, pp.1540-1542 , Jan. 1994.
- [137] J. Zhang, D. Dou, T. Merz, J. Chakhalian, M. Kareev, J. Liu, and L. Brillson, “Depth-resolved subsurface defects in chemically etched SrTiO<sub>3</sub>,” *Appl Phys Lett*, vol. 94, no. 9, pp. 092904–092903, 2009.
- [138] M. Kareev, S. Prosandeev, J. Liu, C. Gan, J. Freeland, M. Xiao, and J. Chakhalian, “Atomic control and characterization of surface defect states of TiO<sub>2</sub> terminated SrTiO<sub>3</sub> single crystals,” *Appl Phys Lett*, vol. 93, p. 061909, 2008.
- [139] M. Kawasaki, K. Takahashi, T. Maeda, and R. Tsuchiya, “Atomic control of the SrTiO<sub>3</sub> crystal surface,” *Science*, vol. 266, no. 5190, pp. 1540–1542, 1994.
- [140] R. E. Hummel and K. H. Guenther, *Handbook of Optical Properties*. CRC Press, pgs 298-302, 1995.
- [141] I. Bozovic and J. N. Eckstein, “Analysis of Growing Films of Complex Oxides by RHEED,” *MRS Bulletin*, vol. 20, no. 5, pp. 32–38, May 1995.
- [142] A. V. Naumkin, A. Kraut-Vass, C. J. Powell, and S. W. Gaarenstroom, *NIST X-ray Photoelectron Spectroscopy Database*. NIST Standard Reference Database Number 20, National Institute of Standards and Technology, Gaithersburg MD, 20899 (2000).
- [143] G. C. Smith, “Evaluation of a simple correction for the hydrocarbon contamination layer in quantitative surface analysis by XPS,” *Journal of Electron Spectroscopy*, pp. 21–28, Dec. 2005.
- [144] X. L. Li, H. B. Lu, M. Li, Z. Mai, H. Kim, and Q. J. Jia, “Characteristics of the low electron density surface layer on BaTiO<sub>3</sub> thin films,” *Appl Phys Lett*, vol. 92, no. 1, p. 012902, Jan. 2008.
- [145] S. M. Mukhopadhyay and T. C. S. Chen, “Surface chemical states of barium titanate: Influence of sample processing,” *J Mater Res*, vol. 10, no. 6, pp. 1502–1507, 1995.
- [146] L. T. Hudson, R. L. Kurtz, S. W. Robey, and D. Temple, “Surface core-level shifts of barium observed in photoemission of vacuum-fractured BaTiO<sub>3</sub> (100),” *Physical Review B*, vol. 47, no. 16, pp. 10832–10838, 1993.
- [147] A. L. Kholkin, N. A. Pertsev, and A. V. Goltsev, “Piezoelectricity and Crystal Symmetry,” in *Piezoelectric and Acoustic Materials for Transducer Applications*, no. 2, Boston, MA: Springer, Boston, MA, 2008, pp. 17–38.
- [148] P. Dineva, D. Gross, R. Müller, and T. Rangelov, “Piezoelectric Materials,” in

- Dynamic Fracture of Piezoelectric Materials*, vol. 212, no. 2, Cham: Springer International Publishing, 2014, pp. 7–32.
- [149] R. Wishengrad and V. Kelley, “Dimension V Instruction Manual,” Bruker, Mar. 2011.
- [150] F. Peter, *Piezoresponse force microscopy and surface effects of perovskite ferroelectric nanostructures*. Information Technology, Vol 11, Die Deutsche Bibliothek. 2006.
- [151] D. A. Bonnell, S. V. Kalinin, A. L. Kholkin, and A. Gruverman, “Piezoresponse Force Microscopy: A Window into Electromechanical Behavior at the Nanoscale,” *MRS Bulletin*, vol. 34, no. 9, pp. 648–657, Sep. 2009.
- [152] R. Proksch and S. Kalinin, *Piezoresponse force microscopy with asylum research AFMs*. PFM App Note, 2008.
- [153] R. K. Vasudevan, N. Balke, P. Maksymovych, S. Jesse, and S. V. Kalinin, “Ferroelectric or non-ferroelectric: Why so many materials exhibit ferroelectricity? on the nanoscale,” *Applied Physics Reviews*, vol. 4, no. 2, p. 021302, Jun. 2017.
- [154] D. A. L. Kholkin, D. S. V. Kalinin, D. A. Roelofs, and A. Gruverman, “Review of Ferroelectric Domain Imaging by Piezoresponse Force Microscopy,” in *Scanning Probe Microscopy*, no. 7, New York, NY: Springer New York, 2007, pp. 173–214.
- [155] A. Gruverman, O. Auciello, and H. Tokumoto, “Scanning force microscopy for the study of domain structure in ferroelectric thin films,” *Journal of Vacuum Science & Technology B (Microelectronics and Nanometer Structures)*, vol. 14, no. 2, pp. 602–605, 1996.
- [156] T. Jungk, A. Hoffmann, and E. Soergel, “Quantitative analysis of ferroelectric domain imaging with piezoresponse force microscopy,” *Appl Phys Lett*, vol. 89, no. 16, p. 163507, Oct. 2006.
- [157] E. Soergel, “Piezoresponse force microscopy (PFM),” *Journal of Physics D: Applied Physics*, vol. 44, no. 46, p. 464003, Nov. 2011.
- [158] T. Jungk, Á. Hoffmann, and E. Soergel, “Consequences of the background in piezoresponse force microscopy on the imaging of ferroelectric domain structures,” *Journal of Microscopy*, vol. 227, no. 1, pp. 72–78, Jul. 2007.
- [159] T. Jungk, A. Hoffmann, and E. Soergel, “Challenges for the determination of piezoelectric constants with piezoresponse force microscopy,” *Appl Phys Lett*, vol. 91, no. 25, p. 253511, 2007.
- [160] T. Jungk, A. Hoffmann, and E. Soergel, “Contrast mechanisms for the detection of ferroelectric domains with scanning force microscopy,” *New J. Phys.*, vol. 11, no. 3, p. 033029, Mar. 2009.

- [161] W. Wang, Y. Geng, and W. Wu, "Background-free piezoresponse force microscopy for quantitative measurements," *Appl Phys Lett*, vol. 104, no. 7, p. 072905, Feb. 2014.
- [162] D. Denning and J. Guyonnet, "Applications of piezoresponse force microscopy in materials research: from inorganic ferroelectrics to biopiezoelectrics and beyond," *International Materials Review*, Vol 61, pgs 46-70, 2015.
- [163] M. Alexe and A. Gruverman, *Nanoscale Characterisation of Ferroelectric Materials*. Berlin, Heidelberg: Springer Science & Business Media, pgs 4-18, 2013.
- [164] J. L. Wang, F. Gaillard, A. Pancotti, B. Gautier, G. Niu, B. Vilquin, V. Pillard, G. L. M. P. Rodrigues, and N. Barrett, "Chemistry and Atomic Distortion at the Surface of an Epitaxial BaTiO<sub>3</sub> Thin Film after Dissociative Adsorption of Water," *The Journal of Physical Chemistry C*, vol. 116, no. 41, pp. 21802–21809, Oct. 2012.
- [165] M. Maglione, G. Philippot, D. Levasseur, S. Payan, C. Aymonier, and C. Elissalde, "Defect chemistry in ferroelectric perovskites: long standing issues and recent advances," *Dalton Trans.*, vol. 44, no. 30, pp. 13411–13418, Jul. 2015.
- [166] J. Baniecki, M. Ishii, K. Kurihara, K. Yamanaka, T. Yano, K. Shinozaki, T. Imada, K. Nozaki, and N. Kin, "Photoemission and quantum chemical study of SrTiO<sub>3</sub> (001) surfaces and their interaction with CO<sub>2</sub>," *Physical Review B*, vol. 78, no. 19, Nov. 2008.
- [167] F. Peter, K. Szot, R. Waser, B. Reichenberg, S. Tiedke, and J. Szade, "Piezoresponse in the light of surface adsorbates: Relevance of defined surface conditions for perovskite materials," *Appl Phys Lett*, vol. 85, no. 14, p. 2896, 2004.
- [168] V. E. Henrich, G. Dresselhaus, and H. J. Zeiger, "Surface defects and the electronic structure of SrTiO<sub>3</sub> surfaces," *Physical Review B*, vol. 17, no. 12, pp. 4908–4921, 1978.
- [169] A. E. Becerra-Toledo, J. A. Enterkin, D. M. Kienzle, and L. D. Marks, "Water adsorption on SrTiO<sub>3</sub>(001): II. Water, water, everywhere," *Surface Science*, vol. 606, no. 9, pp. 791–802, May 2012.
- [170] S. Nasser, "X-ray photoelectron spectroscopy study on the composition and structure of BaTiO<sub>3</sub> thin films deposited on silicon," *Appl Surf Sci*, vol. 157, no. 1, pp. 14–22, 2000.
- [171] F. Johann and E. Soergel, "Quantitative measurement of the surface charge density," *Appl Phys Lett*, vol. 95, no. 23, p. 232906, Dec. 2009.
- [172] S. V. Kalinin and D. A. Bonnell, "Imaging mechanism of piezoresponse force microscopy of ferroelectric surfaces," *Physical Review B*, vol. 65, no. 12, p. 125408, Mar. 2002.

- [173] P. Fisher, H. Du, M. Skowronski, P. A. Salvador, O. Maksimov, and X. Weng, “Stoichiometric, nonstoichiometric, and locally nonstoichiometric SrTiO<sub>3</sub> films grown by molecular beam epitaxy,” *J Appl Phys*, vol. 103, no. 1, p. 013519, 2008.
- [174] K. Virwani and V. Kelley, “Piezoresponse Atomic Force Microscopy Using a NanoScope V Controller,” Bruker, Jun. 2008.
- [175] C. J. Brennan, R. Ghosh, K. Koul, S. K. Banerjee, N. Lu, and E. T. Yu, “Out-of-Plane Electromechanical Response of Monolayer Molybdenum Disulfide Measured by Piezoresponse Force Microscopy,” *Nano Lett*, vol. 17, no. 9, pp. 5464–5471, Aug. 2017.
- [176] H. P. Sun, X. Q. Pan, J. H. Haeni, and D. G. Schlom, “Structural evolution of dislocation half-loops in epitaxial BaTiO<sub>3</sub> thin films during high-temperature annealing,” *Appl Phys Lett*, vol. 85, no. 11, pp. 1967–1969, Sep. 2004.
- [177] J. P. McCaffrey and J. Hulse, “Transmitted color and interference fringes for TEM sample preparation of silicon,” *Micron*, vol. 29, no. 2, pp. 139–144, 1998.
- [178] A. Bosacchi, P. Frigeri, S. Franchi, P. Allegri, and V. Avanzini, “InAs/GaAs self-assembled quantum dots grown by ALMBE and MBE,” *Journal of Crystal Growth*, 1997, vol. 175, pp. 771–776.
- [179] R. Tromp, F. Ross, and M. Reuter, “Instability-driven SiGe island growth,” *Phys Rev Lett*, vol. 84, no. 20, pp. 4641–4644, 2000.
- [180] F. Huaxiang and L. Bellaiche, “Off-center atomic displacements in BaTiO<sub>3</sub> quantum dots,” *AIP Conference Proceedings*, vol. 677, no. 1, p. 139, 2003.
- [181] M. J. Polking, M.-G. Han, A. Yourdkhani, V. Petkov, C. F. Kisielowski, V. V. Volkov, Y. Zhu, G. Caruntu, A. P. Alivisatos, and R. Ramesh, “Ferroelectric order in individual nanometre-scale crystals,” *Nature Materials*, vol. 11, no. 8, pp. 700–709, Aug. 2012.
- [182] D. Karpov, Z. Liu, T. dos Santos Rolo, R. Harder, P. V. Balachandran, D. Xue, T. Lookman, and E. Fohtung, “Three-dimensional imaging of vortex structure in a ferroelectric nanoparticle driven by an electric field,” *Nat Comms*, vol. 8, no. 1, p. 280, Aug. 2017.

## Appendix A: Description of Research for Popular Publication

Self-Assembled Barium Titanate

A Simpler Way to Make a Ferroelectric

By Timothy A Morgan

Recipes that are simpler to follow typically are more popular among home bakers. When you get a delicious cake with half the time and less complicated steps, most cooks consider it a plus. However, simpler recipes typically sacrifice some flavor. But, what if you could have both? Simpler with the same flavor.

The new growth approach proposed by University of Arkansas researchers have developed a simpler way to grow barium titanate without sacrificing any of its properties. The key ingredient is to use excess barium during growth. Typically, when baking a cake, measuring the exact amount of ingredients is essential to obtaining the desired flavor. However, when growing with excess barium, the material takes what barium it needs and passes the rest to the top, where it is simply wiped off.

What baker wouldn't love removing the simplicity of measuring? Instead of leveling off a measuring cup or pulling out a scale to get down to the 0.1 oz of flour, just dump in some extra flour. When the cake comes out of the oven, the excess will be on top and it can just be wiped off.

Beyond simplicity, excess barium opens up co-deposition as a way to grow barium titanate. Historically,  $\text{BaTiO}_3$  has been grown as a super lattice of  $\text{BaO}$  and  $\text{TiO}_2$  layers like a layered cake. This approach was a carryover from the days of oxide MBE being used to grow superconductors such as  $\text{Tl}_2\text{Ba}_2\text{Ca}_{n-1}\text{Cu}_n\text{O}_{2n+4}$ , where there were many components and the

structure was much more complex which demanded sequential layering of components. When ferroelectrics were grown using oxide MBE, they simply continued using the same methods. However, when BaO and TiO<sub>2</sub> are on a surface with sufficient temperature, the preferred compound is BaTiO<sub>3</sub>. In co-deposition, we put barium and titanium on the same plane. They metals oxidize and form BaTiO<sub>3</sub>.

What's amazing is that they rearrange. It's like putting strawberry and lemon cake ingredients into a batter and baking it. When the cake is cut you see a layered cake with alternating layers of strawberry and lemon instead of a uniformly mixed lemonberry cake.

The self-assembly of barium titanate opens up an easier way to control stoichiometry. In industry, reducing how precise the deposition of barium is makes fabrication of BTO capacitors much easier for corporations to make profits.



## **Appendix B: Executive Summary of Newly Created Intellectual Property**

The following list of new intellectual property items were created in the course of this research project and should be considered from both a patent and commercialization perspective.

1. A method for creating stoichiometric barium titanate in half the time of conventional growth methods. Barium titanate is typically grown by a cycle of BaO-TiO<sub>2</sub> layers that require a long calibration time. The new method allows for co-deposition of Ba, Ti, and O, reducing the growth time in half. This also eliminates the need for long calibration time.

## **Appendix C: Potential Patent and Commercialization Aspects of listed Intellectual Property Items**

### **C.1 Patentability of Intellectual Property (Could Each Item be Patented)**

The one item listed was considered first from the perspective of whether or not the item could be patented.

1. The growth approach could be patented because of its novel approach to producing stoichiometric barium titanate using molecular beam epitaxy. Reducing the growth time in half would be of benefit to industrial production of BTO by MBE.

### **C.2 Commercialization Prospects (Should Each Item Be Patented)**

The one item listed was then considered from the perspective of whether or not the item should be patented.

1. The growth approach should be patented since the market for oxide MBE growth in industry is still early in its development. Primarily powders are produced at this time for capacitors.

### C.3 Possible Prior Disclosure of IP

The following items were discussed in a public forum or have published information that could impact the patentability of the listed IP.

1. T. Al. Morgan, M. Zamani-Alavijeh, S. Erickson, G. Story, A. Schroeder, A. V. Kuchuk, M. Benamara, G. J. Salamo, “Self-Assembled Barium Titanate Thin Films by Molecular Beam Epitaxy”, Accepted for publication in Journal of Crystal Growth, April 2018
2. T. Al. Morgan, M. Zamani-Alavijeh, G. Story, A. Schroeder, A. V. Kuchuk, M. Benamara, G. J. Salamo, “Self-limiting Growth of Barium Titanate via Molecular Beam Epitaxy”, Oral Presentation at the IEEE ISAF-IWATMD-PFM Conference, Atlanta, GA May 7-11, 2017.
3. T. Al. Morgan, M. Zamani-Alavijeh, G. Story, A. Schroeder, A. V. Kuchuk, M. Benamara, G. J. Salamo, Poster presentation “Off-stoichiometric growth of barium titanate”, Fundamental Physics of Ferroelectrics, Williamsburg, VA 2017

## Appendix D: Broader Impact of Research

### D.1 Applicability of Research Methods to Other Problems

The discovery of excess barium being a self-limiting mechanism for controlling stoichiometry came while investigating ferroelectricity as a function of Ti/Ba change. While plotting the  $d_{33}$  vs Ti/Ba, there were no films with Ti/Ba less than 1. Further testing led to the discovery that co-deposition under excess barium allows for barium titanate to self-assemble.

One of the principles of the self-limiting mechanism is based on stable perovskite structure. A stable perovskite structure has a tolerance factor between 0.75 and 1. If barium were to sit in the B-site, the tolerance factor would be outside this range for tolerance factors. For example, strontium can sit in the B-site and fall within a stable range. One other possible titanate,  $\text{CaTiO}_3$ , might be a candidate for this technique. The other consideration is how easy it would be to remove the excess that comes to the top.

### D.2 Impact of Research Results on U.S. and Global Society

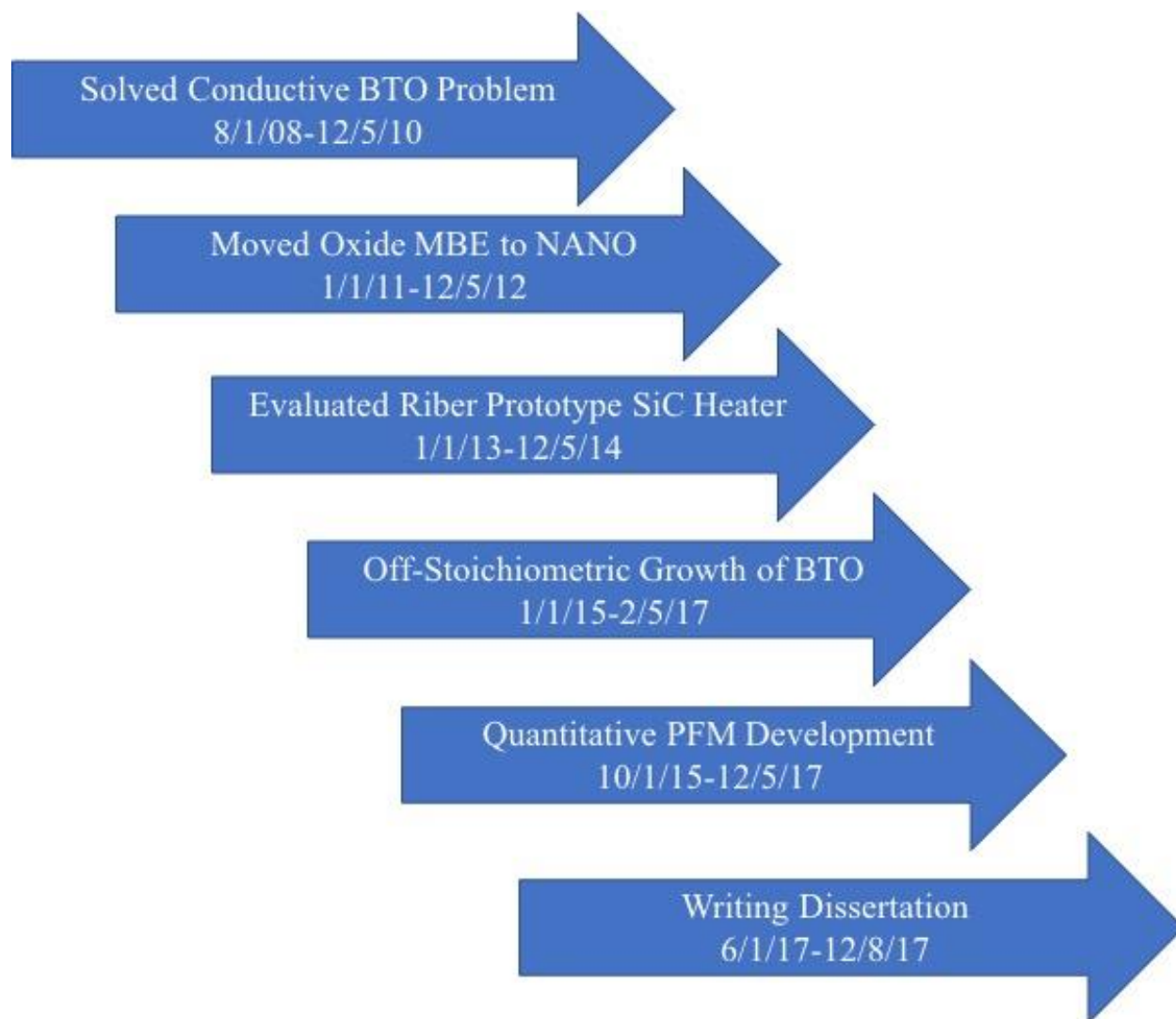
The largest impact of this research would be manufacturing. Reducing the growth time of MBE grown barium titanate could lead to producing barium titanate more consistently. The downside would be using extra barium and an extra step. The cost-effectiveness of this solution would have to be evaluated. If the yield increased, the excess barium and processing step may be worth it.

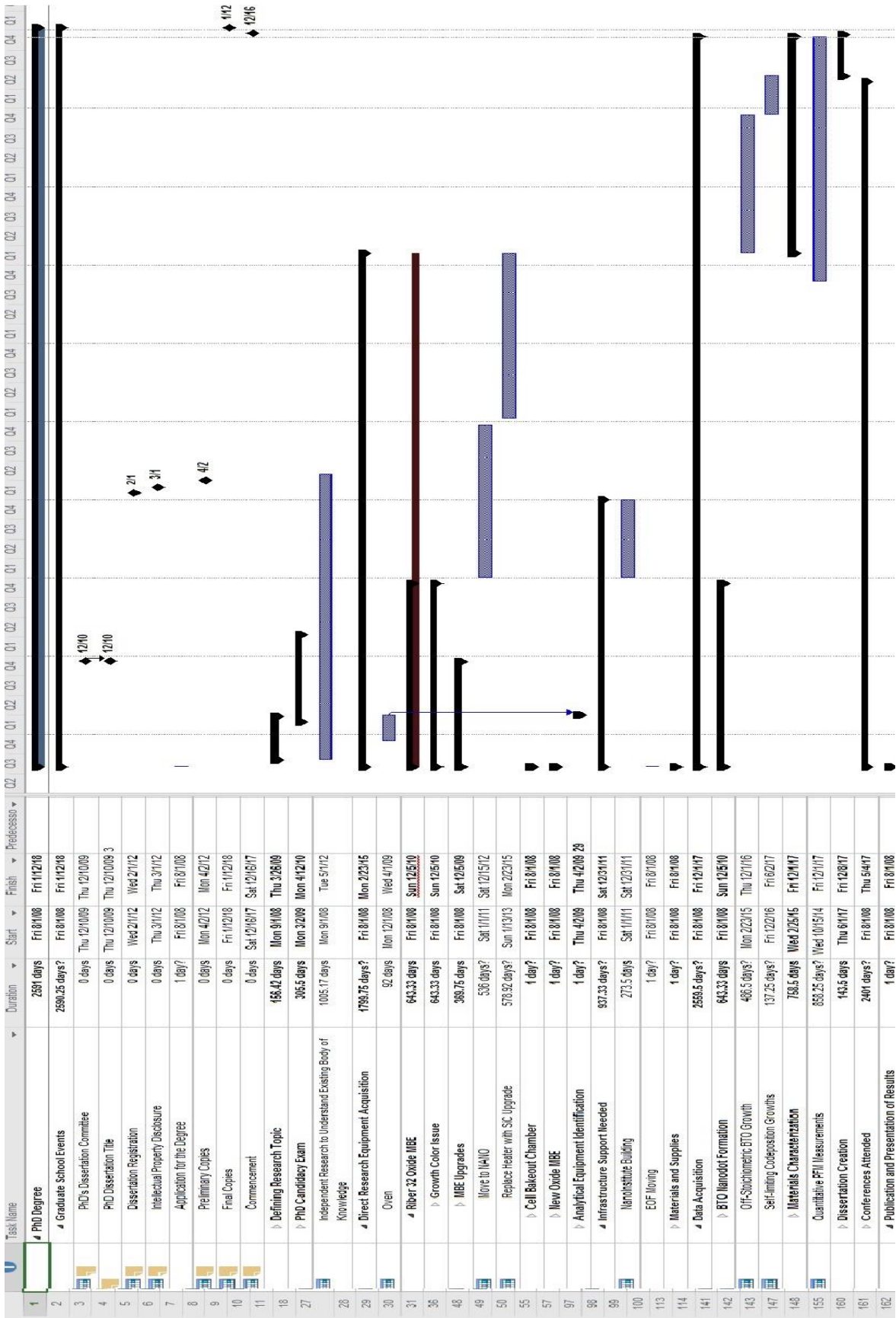
The use of BTO as a motion activated friction reducing coating could provide immense value. BTO is also biocompatible, making these coatings a possibility inside knee joint replacements.

### D.3 Impact of Research Results on the Environment

The increase of barium oxide waste would not be a concern since it is not toxic to the environment. Furthermore, BTO can be used to generate energy through its piezoelectric properties. In addition to reducing friction, which will extend the life of a product, BTO can generate electricity when pushed upon; interesting applications include tennis shoes and soccer balls, where they are constantly being pushed and could generate power in everyday life.

## Appendix E: Microsoft Project for PhD MicroEP Degree Plan





## **Appendix F: Identification of All Software Used in Research and Dissertation Generation**

### Computer #1:

Model Number: Apple iMac 27”

Serial Number:

Location: NANO 111

Owner: Dr. Greg Salamo

### Software #1:

Name: Microsoft Office 2016

Purchased by: University of Arkansas Site License

### Computer #2:

Model Number: Custom PC

Serial Number:

Location: NANO 111

Owner: Dr. Greg Salamo

### Software #1:

Name: Microsoft Office 2016

Purchased by: University of Arkansas Site License

### Software #2:

Name: OriginPro 8

Purchased by: Dr. Greg Salamo

### Software #3:

Name: Nanoscope Analysis



Purchased by: Freeware by Bruker

Software #4:

Name: MultiPak

Purchased by: Arkansas Bio-Nano Material Characterization Facility

Software #5:

Name: VESTA

Purchased by: Freeware by JP Minerals

## Appendix G: All Publications Published, Submitted and Planned

- M. Zamani-Alavijeh, **T. Al. Morgan**, A. V. Kuchuk, M. Benamara, G. J. Salamo, “Ferroelectric properties dependence on barium titanate thickness”, in preparation, 2018
- **T. Al. Morgan**, M. Zamani-Alavijeh, S. Erickson, G. Story, A. Schroeder, A. V. Kuchuk, M. Benamara, G. J. Salamo, “Self-Assembled Barium Titanate Thin Films by Molecular Beam Epitaxy”, Accepted for publication in Journal of Crystal Growth, April 2018
- Li C, **Morgan T. Al.**, Kuchuk A. V., Benamara M., Maidaniuk Y, Shetty S, Mazur Y, Ware M E & Salamo G J, Kinetically controlled indium surface coverage effects on PAMBE-growth of InN/GaN(0001) quantum well structures, Accepted for publication in Journal of Applied Physics, April 2018
- Abolhassani, M., Griggs, C. S., Gurtowski, L. A., Mattei-Sosa, J. A., Nevins, M., Medina, V. F., **Morgan, T. Al.**, Greenlee, L. F., “Scalable Chitosan-Graphene Oxide Membranes: The Effect of GO Size on Properties and Cross-Flow Filtration Performance”, ACS Omega, Accepted November 22, 2017
- **T. Al. Morgan**, M. Zamani-Alavijeh, G. Story, A. Schroeder, A. V. Kuchuk, M. Benamara, G. J. Salamo, “Self-limiting Growth of Barium Titanate via Molecular Beam Epitaxy”, IEEE Proceedings of the 2017 International Symposium on the Applications of Ferroelectrics, 2017
- Zeng Z, **Morgan T Al**, Fan D, Li C, Hirono Y, Hu X, Zhao Y, Lee J S, Wang J, Wang Z M, Yu S, Hawkrigde M E, Benamara M and Salamo G J (2013) Molecular beam epitaxial growth of Bi<sub>2</sub>Te<sub>3</sub> and Sb<sub>2</sub>Te<sub>3</sub> topological insulators on GaAs (111) substrates: a potential route to fabricate topological insulator p-n junction AIP Advances **3** 072112–072112–8
- V. P. Kunets, C. S. Furrow, **T. Al. Morgan**, Y. Hirono, M. E. Ware, V. G. Dorogan, Y. I. Mazur, V. P. Kunets, and G. J. Salamo, “InGaAs quantum wire intermediate band solar cell,” Appl Phys Lett, vol. 101, no. 4, p. 041106, 2012.
- Li, C., Zeng, Z. Q., Fan, D. S., Hirono, Y., Wu, J, **T. Al. Morgan** et. al.. (2011). Bismuth nano-droplets for group-V based molecular-beam droplet epitaxy. Applied Physics.
- J Dobbert, Vas. P Kunets, **T. Al Morgan**, D Guzun, Yu. I Mazur, W. T Masselink, and G. J Salamo, J Mater Sci-Mater El 19 (8-9), 797 (2008).
- Vas. P Kunets, **T. Al Morgan**, Yu. I Mazur, V. G Dorogan, P. M Lytvyn, M. E Ware, D Guzun, J. L Shultz, and G. J Salamo, J Appl Phys 104 (10), 103709 (2008).
- Julia Dobbert, Vasyl P Kunets, **T. Al. Morgan**, Dorel Guzun, Yuriy I Mazur, William Ted Masselink, and Gregory J Salamo, Ieee T Electron Dev 55 (2), 695 (2008).

## Conference Presentations

- **T. Al. Morgan**, M. Zamani-Alavijeh, G. Story, A. Schroeder, A. V. Kuchuk, M. Benamara, G. J. Salamo, “Self-limiting Growth of Barium Titanate via Molecular Beam Epitaxy”, Oral Presentation at the IEEE ISAF-IWATMD-PFM Conference, Atlanta, GA May 7-11, 2017.
- **T. Al. Morgan**, M. Zamani-Alavijeh, G. Story, A. Schroeder, A. V. Kuchuk, M. Benamara, G. J. Salamo, Poster presentation “Off-stoichiometric growth of barium titanate”, Fundamental Physics of Ferroelectrics, Williamsburg, VA 2017
- **T. Al. Morgan**, M. Zamani-Alavijeh, G. Story, W. Schroeder, A. V. Kuchuk, M. Benamara, AND G. J. Salamo, “Growth of Different Structural Phases of Barium Titanate,” Poster presentation at Arkansas NSF EPSCoR Annual Conference Little Rock, AR May 24-25, 2016.
- **T. Al. Morgan**, M. Zamani-Alavijeh, M. Benamara, M. Mortazavi and G. J. Salamo, “Ferroelectric Properties of Barium Titanate Thin Films for Data Storage Devices,” presented at the Arkansas Space Grant Consortium Annual Meeting, Hot Springs, Ar, April 15-16, 2016.
- **T. Al. Morgan**, V. Kunets, M. E. Ware, X. Hu, Y. Hirono, C. S. Furrow, V. G. Dorogan, M. Benamara, Y. I. Mazur, G. J. Salamo, N. Alnami, and M. Mortazavi, “Green Energy Generation and Storage: Integration of Quantum Dot Solar Cells and Ferroelectric Capacitors,” presented at the Arkansas Space Grant Consortium Annual Meeting, Hot Springs, Ar, April 9-10, 2015.
- **T. Al. Morgan**, Z.Q. Zeng, R.J. Sleezer, and G.J. Salamo, Growth of Self-Assembled BaTiO<sub>3</sub> Nanodots using Tensile Strain, MRS Poster Session 1 (2011)
- **T. Al. Morgan**, Z. Zeng, G. J. Salamo, “Investigation of Ferroelectric Nanodots for Memory Applications”, MRS U. of Arkansas Poster Session (2009)